RECLAMATION

Managing Water in the West

Technical Memorandum TM-85-833000-2014-42

Evidence for Far-field Reservoir Pressurization, Paradox Valley, Colorado

Colorado Basin Salinity Control Project,
Paradox Valley Unit, Colorado
Upper Colorado Region

U.S. Department of the Interior
Bureau of Reclamation

April 2016

Mission Statements

The mission of the Department of the Interior is to protect and provide access to our Nation's natural and cultural heritage and honor our trust responsibilities to Indian Tribes and our commitments to island communities.

The mission of the Bureau of Reclamation is to manage, develop, and protect water and related resources in an environmentally and economically sound manner in the interest of the American public.

BUREAU OF RECLAMATION
Technical Service Center, Denver, Colorado
Seismology, Geomorphology, and Geophysics Group, 85-833000

Technical Memorandum TM-85-833000-2014-42

Evidence for Far-field Reservoir Pressurization, Paradox Valley, Colorado

Colorado Basin Salinity Control Project,
Paradox Valley Unit, Colorado
Upper Colorado Region

Prepared by:

Vanessa King, Geophysicist — 4/7/16 Date

Lisa Block, Geophysicist — 4/10/2016 Date

Peer Review Certification
This report has been reviewed and is believed to be in accordance with the service agreement and standards of the profession.

Peer reviewed by:

Christopher Wood, Geophysicist — 4/11/2016 Date

Executive Summary

The Bureau of Reclamation operates a deep injection well near Paradox Valley, Colorado, which injects salt brine as part of the Colorado River Basin Salinity Control Program. In recent years, the pressure required to inject the brine has been increasing and, prior to a decrease in the injection flow rate in mid-2013, was approaching the maximum allowable surface injection pressure as permitted by the U.S. Environmental Protection Agency (EPA).

Various solutions for reducing the surface pressure without further reductions in the volume of brine being disposed of each year are currently under consideration, including drilling a second injection well. A December 2012 Consultant Review Board (CRB) recommended that the pressure-flow data recorded at the wellhead be investigated to determine whether the pressure increase is caused by far-field reservoir pressurization or near-well flow impairment. This is an important issue in evaluating solutions for reducing the pressures, because if the pressure were caused by near-well flow impairment, it might be possible to rectify the issue with a workover of the existing well. Cleaning and reworking the existing wellbore would likely be a more economical way to reduce pressures than drilling a second injection well. This report summarizes the work that has been performed in response to this CRB recommendation.

Available evidence suggests that far-field pressurization is the dominant factor contributing to the increasing wellhead pressures, and therefore a workover at the existing wellbore is not likely to significantly reduce pressures. Two sources of evidence were investigated: pressure-flow modeling, and spatiotemporal patterns of induced seismicity.

The pressure-flow data can be reasonably well fit using a simple radial flow model and just three free parameters: permeability, skin due to damage, and a wellbore storage constant. Near-wellbore flow impairment should be evident as a change in one or more of these modeled reservoir parameters over time. There are no strong effects in the pressure-flow modeling results for the last several years that indicate near-wellbore changes, and thus the observed pressure increase at the wellhead appears to be related to far-field reservoir pressurization. The radius of investigation of the pressure-flow modeling of individual injection cycles is estimated to be 1 to 2 km. Therefore, these results suggest pore pressure increase in the target injection formations to a distance of at least 1-2 km from the well. The actual extent of elevated pore pressures, however, could be well beyond the radius of investigation.

The spatiotemporal occurrence of induced seismicity indicates that there is substantial vertical and lateral hydraulic connectivity in the near-well region that does not appear to have degraded over time as brine injection has continued. These observations suggest that the increasing depth of fill in the injection well and any potential precipitation and clogging of fractures within ~2-3 km of the well are not noticeably interfering with fluid flow and pore pressure propagation. In addition, changes observed since 2009 in the patterns of induced seismicity occurring ≥6 km from the well suggest that reservoir pressures may be increasing at distances up to ~18 km from the injection well. However, because of the low, fracture-dominated permeability of the

Leadville formation, elevated pore pressures may be propagated over large distances through a limited network of fractures, potentially leading to a strongly heterogeneous pore pressure field. Seismicity patterns also are not symmetric around the wellbore. Seismicity in the areas southwest, south, and southeast of the well has been characterized by relatively low rates and small magnitudes at radial distances greater than about 2.5 km, and no seismicity has occurred in these directions at distances > 7 km, suggesting that geologic factors may be limiting pore pressure increase in these areas. In summary, the induced seismicity patterns are consistent with reservoir pressurization around the well to a distance of 2-2.5 km and suggest pressurization to much larger distances (up to ~ 18 km) in some azimuthal directions.

Contents

Tables

Figures

Page

1 Introduction

The Bureau of Reclamation operates a deep injection well near Paradox Valley, in western Colorado (Figure 1-1), which is referred to in this report as PVU Injection Well #1. This well has been in near-continuous operation since 1996, as part of the Paradox Valley Unit (PVU), a component of the Colorado River Basin Salinity Control Program. Injection at PVU diverts salt brine that would otherwise flow into the Dolores River, a tributary of the Colorado River. The diverted brine is injected into a 4.8-km-deep well for long-term disposal.

In recent years, the pressure required to inject the brine has been increasing and, prior to a decrease in the injection flow rate in mid-2013, was approaching the maximum allowable surface injection pressure (MASIP), as permitted by the U.S. Environmental Protection Agency (EPA).

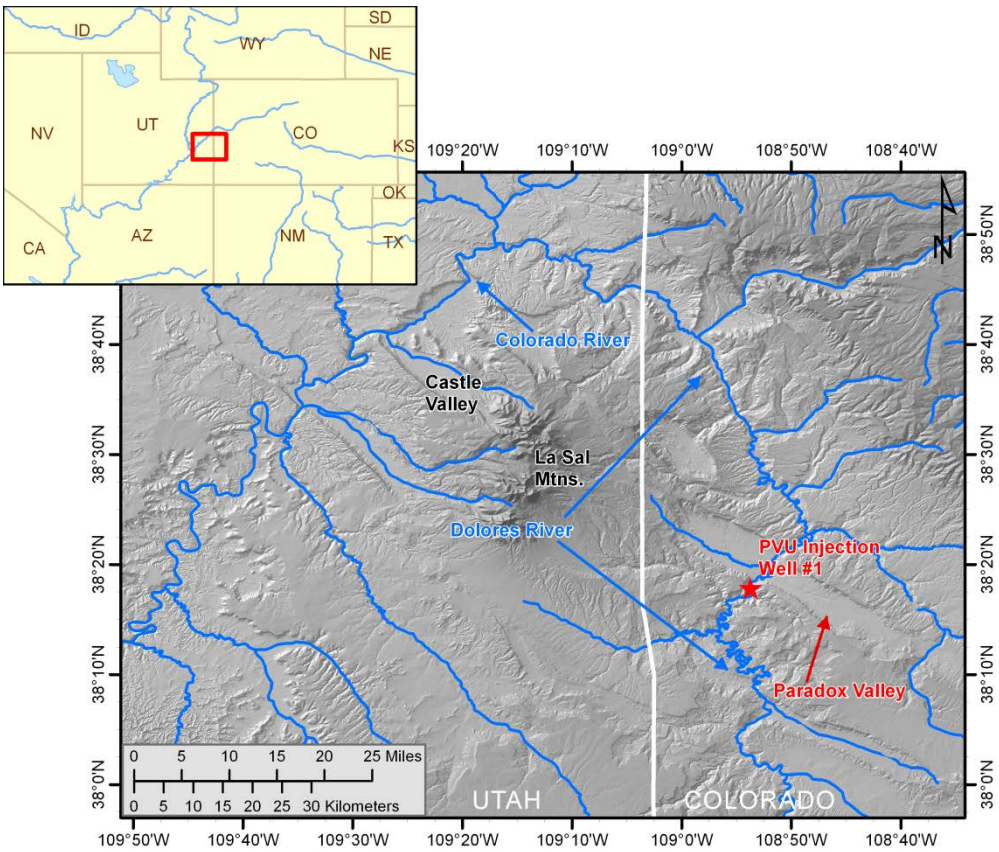

Figure 1-1. Location of the deep injection well at Reclamation's Paradox Valley Unit in western Colorado.

A second injection well is under consideration as a potential means to control the surface injection pressure without additional reductions in the volume of brine disposed of each year. A Consultant Review Board (CRB) was held in December 2012 to review the information that is currently available for selecting the location of a potential second injection well, and to make recommendations for additional data that could be acquired or analyses that could be performed to aid in the site selection process. One recommendation made by the CRB was to analyze the

pressure-flow data in order to examine the temporal evolution of reservoir parameters and "evaluate whether the gradual pressure build-up is indeed a far-field pressurization process, or is more related to near-field flow impairment processes that might be rectified more economically" (Dusseault et al., 2013). This analysis was identified as a priority in an Accountability Report prepared in response to the CRB recommendations (Block, 2014). This report summarizes much of the work that has been performed in response to this CRB recommendation. Some of this work is also discussed in another Technical Memorandum (Wood et al., 2016).

While PVU lacks any observation wells that would help directly measure the degree of far-field subsurface pressurization, available evidence suggests that far-field pressurization is the dominant factor contributing to the increasing wellhead pressures. Here two sources of evidence are considered: results of pressure-flow modeling, and the spatiotemporal occurrence of induced seismicity.

2 Local Geology

A summary of the local geology in the vicinity of Paradox Valley is provided in this section; see King et al. (2014) and Block et al. (2012) for further information regarding both the local and regional geology.

Paradox Valley and the surrounding mesas contain rocks spanning Precambrian to mid-Cretaceous time. The Precambrian basement rock consists of granite, schist, gneiss, and pegmatite. Overlying the Precambrian rock is a series of sedimentary units including sandstones, siltstones, shales, conglomerates, limestones, dolomites, and evaporites.

A stratigraphic column of the Paradox Valley area is presented in Table 2-1. PVU Injection Well #1 is sited on the Triassic-age Chinle Formation. The stratigraphy of the underlying formations shown in Table 2-1 is taken from the geologic well log for this borehole (Harr, 1988), which extends into the Precambrian basement rock. Depths of geologic units encountered in this well are included in the table and are relative to the local ground surface elevation of 4996 ft (1523 m). The overlying stratigraphy, including the Triassic-age Wingate sandstone to the Cretaceous-age Mancos shale, is taken from a geologic map of the Moab Quadrangle produced by the United States Geological Survey (Williams, 1964). Descriptions of the rock units are taken from several sources (see Footnote 2 in Table 2-1).

The Mississippian Leadville formation is the primary target reservoir for PVU brine injection, due to its sedimentary and structural characteristics. The Leadville formation consists of limestone and dolomite layers that are fractured, faulted, and contain karst features. The lower Leadville formation (Kinderhookian-age) consists of stromatolitic dolomite, lime mudstones, and pelletal lime mudstone deposited in intertidal to subtidal environments. The upper Leadville formation (Osagean-age) is separated by an unconformity and contains fossiliferous pelletal and oolitic limestone, and lime and dolomitic mudstone (Campbell, 1981). The upper Leadville underwent uplift and erosion after deposition, resulting in karst-type weathering and the formation of a terra rosa type regolith on the surface. Hence, not only was the thickness of the Leadville decreased along the structural highs, but the porosity was also reduced when solution cavities that formed during uplift were later filled with shales and clays. Areas of dolomitization directly below these weathered sections generally have the best reservoir characteristics. Effective porosity improves with the degree of dolomitization (Bremkamp and Harr, 1988).

Table 2-1. Paradox Valley stratigraphy

Stratigraphic Unit	Depth[1]	Description[2]
CRETACEOUS[3] (145-65 Ma)		
Mancos Shale	Above elevation of wellhead	Dark gray to black, soft, fissile marine shale with thin sandstone beds at various horizons.
Dakota Sandstone		Friable to quartzitic fluvial sandstone and conglomeratic sandstone with interbedded carbonaceous nonmarine shale.
Burro Canyon Fm.		Fluvial sandstone and conglomerate interbedded with lacustrine siltstone, shale, and mudstone, and thin beds of impure limestone.
JURASSIC (205-145 Ma)		
Morrison Fm.	Above elevation of wellhead	Fluvial and lacustrine shale, mudstone, and sandstone; local thin limestone beds.
Summerville Fm.		Sandy shale and mudstone of terrestrial origin.
Entrada Sandstone		Fine- to medium-grained, massive, and cross-bedded eolian sandstone; basal few feet may consist of red siltstone and fine-grained sandstone and is sometimes referred to as the Carmel Formation.
Navajo Sandstone		Fine-grained, cross-bedded eolian sandstone.
TRIASSIC (255-205 Ma)		
Kayenta Fm.	Above elevation of wellhead	Irregularly interbedded fluvial shale, siltstone, and fine to coarse-grained sandstone.
Wingate Sandstone		Fine-grained, massive, thick-bedded and prominently cross-bedded eolian sandstone.
Chinle Fm.	0 (at surface)	Siltstone interbedded with lenses of sandstone and shale, limestone-pebble and shale-pellet conglomerate, with lenses of grit and quartz-pebble conglomerate near base. Terrestrial depositional environment.
Moenkopi Fm.	390	Sandy shale/silty sandstone with some conglomerate present. Marine and terrestrial depositional environment.
PERMIAN (298-255 Ma)		
Cutler Fm.	1,140	Fluvial arkose and arkosic conglomerate, with some sandy shales; deposited in alluvial fans.
PENNSYLVANIAN (322-298 Ma)		
Hermosa Group – Honaker Trail Fm.:		
Upper Honaker Trail	8,313	Limestone/sandstone/siltstone; deposited in marine conditions.
La Sal	12,006	Limestone/dolomite; some silty limestone, oolitic limestone, and algal limestone present.
Lower Honaker Trail	12,082	Limestone/sandstone/siltstone; deposited in marine conditions.
Hermosa Group – Paradox Fm.:	12,350	Resulted from intermittently closed marine environment.
Ismay	12,839	Limestone, stacked algal carbonate mounds and other shallow-water carbonates and dolomites.
1st Main Salt	13,104	Dolomite/salt; intermittently closed marine environment.
2nd Main Salt	13,497	Salt/anhydrite/shale; intermittently closed marine environment.
Base Salt – Lower Paradox	13,566	Shale/anhydrite/(minor) limestone; intermittently closed marine depositional environment.
Hermosa Group – Pinkerton Trail Fm.	13,693	Shales/anhydrites/siltstone/(minor) limestones; dark colored shales, limestone formed by marine invasion.

Molas Fm.	13,944	Shale/siltstone/claystone; regolith/soil (*terra rosa*) de-veloped on the karst surface of the Leadville formation after a period of extensive weathering and erosion.
MISSISSIPPIAN (355-322 Ma)		
Leadville Fm.	13,984	Limestone/dolomite. Lower unit (Kinderhookian-age) stromatolitic dolomite, lime mudstones, pelletal lime mudstones; deposited in intertidal to subtidal environments. Upper unit (Osagean-age) fossiliferous pelletal and oolitic limestone, and lime and dolomitic mudstone.
DEVONIAN (416-355 Ma)		
Ouray Fm.	14,400	Limestone—lime mudstone, pelletal lime mudstone and skeletal limestone that is locally dolomitized; formed in quiet-water marine environment.
Elbert Fm.	14,440	Sandstone/shales/shaly dolomites.
McCracken Fm.	14,607	Sandstone with occasional interbeds of sandy dolomite; transgressive depositional environment.
Aneth Fm.	14,681	Dolomite/shale; dense, argillaceous sequence.
CAMBRIAN (540-488 Ma)		
Lynch Fm.: Upper Lynch Shale Lynch Limestone Lower Lynch Shale	 14,763 14,835 14,928	 Sandstone/interbedded shale, dolomite, limestone. Limestone. Shale.
Muav Fm.	14,988	Limestone.
Bright Angel Fm.	15,103	Shale.
Ignacio Fm.	15,246	Sandstone, sometimes referred to as quartzite; transgressive depositional environment.
PRECAMBRIAN (>540 Ma)		
Precambrian	15,446	Described regionally as granitic rock with well-developed northwest and northeast orthogonal fracture systems; identified in PVU Injection Well #1 as moderately metamorphosed diorite-gabbro schist.

[1]Depths are taken from the geologic drill log of PVU Injection Well #1 by Harr (1988). Depths are relative to the ground surface elevation (4996 ft) and have been corrected for borehole deviation.
[2]Descriptions are taken from: Bremkamp and Harr (1988), Campbell (1981), Doelling (1988), Williams (1964), and Nuccio and Condon (1996).
[3]Ages from Walker and Geissman (2009).

Porosities derived from analysis of the sonic log acquired for PVU Injection Well #1 indicate 86 ft of 5% or greater porosity (Bremkamp and Harr, 1988). This is similar to the porosity found in the Conoco Scorup Somerville Wilcox #1 well, located 4.6 km north-northeast of PVU Injection Well #1, but significantly higher than the values in any other wells in the region. In addition, the hydrologic permeability within the Leadville formation at PVU Injection Well #1 is greatly increased by the presence of an extensive fracture field related to the Wray Mesa fault system (Bremkamp and Harr, 1988). The Leadville formation shows very little fracturing in the nearby Union Otho Ayers #1-0-30 Well (Bremkamp and Harr, 1988), consistent with the lower porosity measured in that well. Core data from other nearby wells are not available, but given the low primary porosity of the Leadville, the degree of fracturing is likely to be strongly correlated with the porosities derived from logging.

Other formations that were considered viable injection zones in PVU Injection Well #1 include the Precambrian schist, the Devonian Ouray, Elbert, and McCracken formations, and the Cambrian Ignacio formation. The upper 191 feet (58 m) of Precambrian schist encountered in

PVU Injection Well #1 was estimated to contain 30 ft (9 m) of 5% or greater porosity. The Devonian and Cambrian formations showed some favorable porosity and fracture characteristics, but were considered to have low storage volume potential.

PVU Injection Well #1 contains perforations over a 286-foot (87-meter) interval in the Leadville formation. Two 30-foot (9-meter) intervals without perforations were left to assist in future treatment of the injection interval if necessary (Subsurface Technology, 2001). Additional perforated intervals were created in the underlying formations and Precambrian basement, extending more than 1400 feet (427 meters) below the bottom of the Leadville (Subsurface Technology, 2001). Early flow profiles indicated that the Leadville formation accepts the majority of fluid (Envirocorp Services and Technology Inc., 1995).

Additional logging of PVU Injection Well #1 was performed in 2001, including a mechanical casing caliper survey and a differential temperature survey (Subsurface Technology, 2001). The caliper survey indicated that the top-of fill depth was 14,172 feet (4320 meters), at the base of the upper Leadville perforations, indicating that the perforations in the lower Leadville and underlying formations were not accepting significant amounts of fluid. In contrast, a previous survey in 1994 indicated that the top of fill was at 14,604 feet (4451 meters), near the base of the underlying Elbert Formation (Subsurface Technology, 2001).

3 Injection History

Between 1991 and 1995, a series of 7 injection tests were conducted at PVU, in addition to an acid stimulation test and a reservoir integrity test (Envirocorp Services and Technology Inc., 1995). The purpose of these tests was to qualify for a permit for long-term injection from the Environmental Protection Agency (EPA). Continuous injection of brine began in July 1996, after EPA granted the permit. Since the start of continuous injection, four major changes in injection operations have been instituted and maintained at PVU. Each change was made to mitigate the potential for unacceptable seismicity or to improve injection economics. These injection phases are described below. Plots of the daily average injection flow rate, surface injection pressure, and downhole pressure at a depth of 14,100 ft (4.3 km) throughout the history of PVU injection operations are shown in Figure 3-1.

3.1 Phase I (July 22, 1996 – July 25, 1999)

During this initial phase of continuous injection, injection occurred at a nominal flow rate of 345 gpm (1306 l/min), at about 4,950 psi (34.1 MPa) average surface pressure. This corresponds to approximately 11,800 psi (81.4 MPa) downhole pressure at 14,100 ft (4.3 km) depth. To maintain this flow rate, three constant-rate pumps were used concurrently, with each operating at a flow rate of 115 gpm. The surface pressure increased in response to this flow, and regularly approached the wellhead pressure safety limit of 5,000 psi. At these times one or two injection pumps would be shut down, reducing the injection rate and allowing the pressure to drop a few hundred psi, before returning to three-pump injection. These shutdowns occurred frequently and lasted for minutes, hours, or a few days. Maintenance shutdowns lasted for one to two weeks and, in mid-1997, a 71-day shutdown was needed when replacing the operations contractor. The shutdowns resulted in an overall average injection rate for phase I of ~300 gpm (1100 l/min). The injectate during Phase I consisted of 70% Paradox Valley Brine (PVB) and 30% fresh water.

Due to concerns about corrosion, the decision was made in 1997 to switch from using an O_2 scavenger to a rust inhibitor, as the O_2 scavenger was found to be insufficient as a corrosion inhibitor. While the rust inhibitor was substantially more effective at inhibiting corrosion, it also increased the risk of precipitation of elemental sulfur (A. Nicholas, personal communication, 2013).

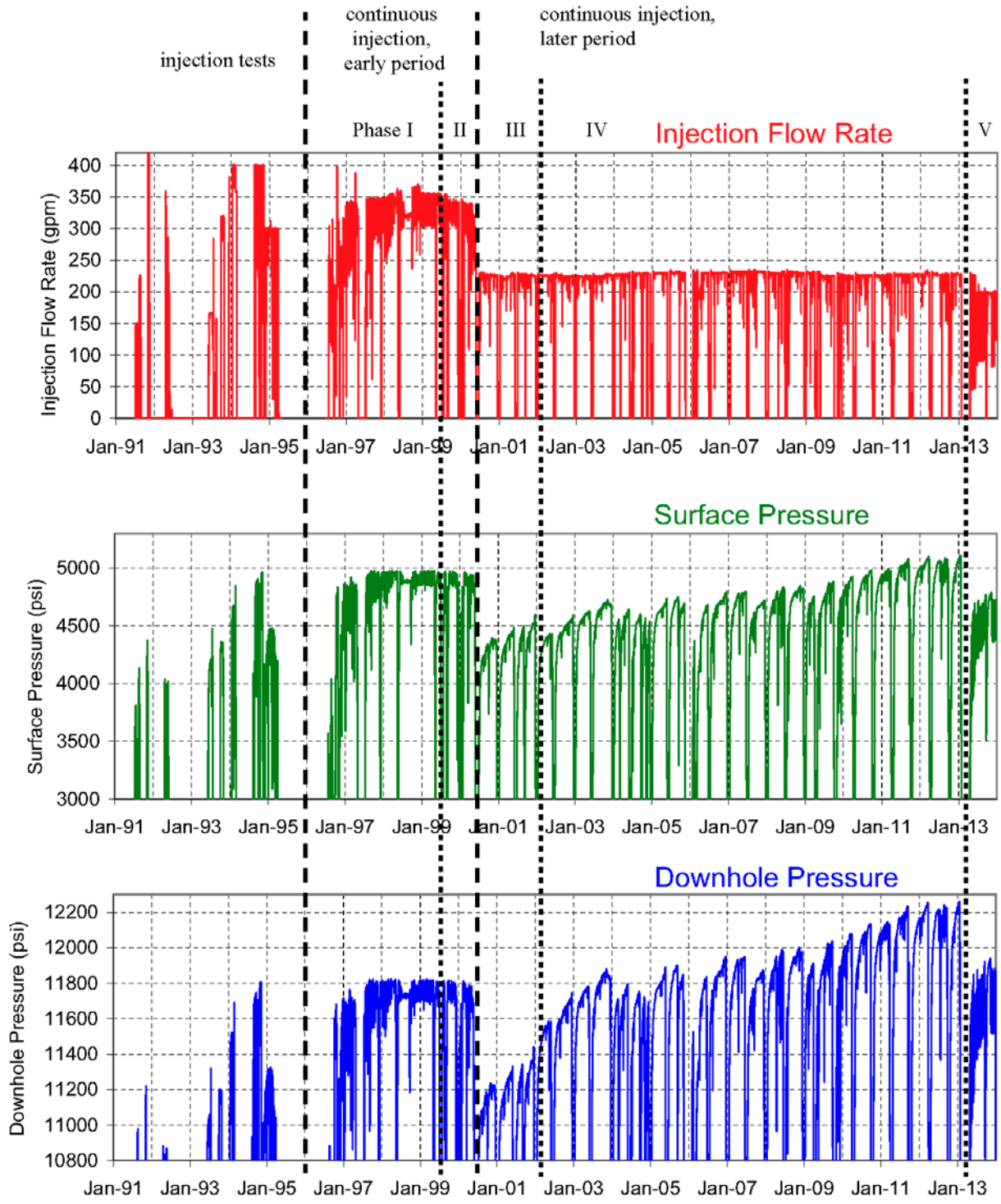

Figure 3-1. Daily average injection flow rate (top), daily average surface injection pressure (middle), and daily average downhole pressure at 14,100 feet (4.3 km) depth (bottom) during PVU injection operations.

3.2 Phase II (July 26, 1999 – June 22, 2000)

Following two local magnitude (M_L) 3.5 induced earthquakes in June and July, 1999, injection operations were changed to include a 20-day shutdown (i.e., a "shut-in") every six months (Mahrer et al., 2002). Prior to these events, it was noted that the rate of seismicity in the near-wellbore region (i.e. within about a 2-km radius from the wellbore) decreased during and following unscheduled maintenance shutdowns, and during the shutdowns following the injection tests of 1991 through 1995 (Mahrer et al., 2001). It was thought that the biannual shutdowns might reduce the potential for inducing felt seismicity by allowing extra time for the injectate to diffuse from the pressurized fractures and faults into the rock matrix. When injecting during this phase, the injection pressure and flow rate were the same as during Phase I.

3.3 Phase III (June 23, 2000 – January 6, 2002)

Immediately following an M_L 4.3 earthquake on May 27, 2000, PVU was shut down for 28 days. During this shutdown period, the existing injection strategy for PVU and its relationship to induced seismicity were evaluated. It was decided to reduce the injection flow rate in order to reduce the potential for inducing felt seismicity (Mahrer et al., 2001). On June 23, 2000, PVU injection operations resumed using a maximum of two pumps, rather than alternating between two and three pumps. The biannual 20-day shutdowns were maintained. The nominal flow rate during Phase III, while injecting using two pumps, was 230 gpm (871 l/min). Accounting for the two 20-day shut-ins per year, the average injection flow rate was approximately 205 gpm (776 l/min), a decrease of about 32% compared to Phase I. The 70:30 ratio of brine to fresh water was maintained.

3.4 Phase IV (January 7, 2002 – April 16, 2013)

Beginning with continuous injection operations in 1996, the injectate had been diluted to 70% PVB and 30% Dolores River fresh water. A geochemical study had predicted that if 100% PVB were injected, it would interact with connate fluids and the dolomitized Leadville limestone at downhole (initial) temperatures and pressures, and that PVB would then precipitate calcium sulfate, which in turn would lead to restricted permeability (Kharaka et al., 1997). During October 2001, with the decreased injection volume discussed above, the injectate concentration concerns were reconsidered (Mahrer et al., 2002). Temperature logging in the injection interval documented substantial near-wellbore cooling, indicating that a significant displacement of connate brine away from the wellbore had occurred by this time, reducing the potential for 100% PVB and connate brine to mix, and therefore that if precipitation occurred, it would not be near the wellbore perforations where clogging would be a concern (Subsurface Technology, 2001). Further discussions indicated that, if precipitation occurred, its maximum expected rate would be ~8 tons of calcium sulfate per day (Mahrer et al., 2002). To put this amount into perspective, injecting at ~230 gpm, assuming a density of 9.86 lbs/gal (17% more dense than fresh water), results in a daily injection of ~1630 tons. The maximum expected precipitate is ~0.5% of the daily injection mass.

After considering this new information, Reclamation decided to begin injecting 100% PVB, in order to increase the amount of salt disposed following the reduced injection rate initialized in Phase III. Injection of 100% PVB began on January 7, 2002, following the December-January 20-day shutdown, and has been maintained since. The same reduced injection rate as in Phase III (230 gpm) and biannual 20-day shutdowns have been maintained. The only noticeable effect of the change to 100% PVB injectate has been increasing bottom hole pressure because of the increased density of 100% PVB (by about 5%) over the 70% PVB to 30% fresh water mix (Ake et al., 2005).

3.5 Phase V (April 17, 2013 – present)

An M_L 4.4 induced earthquake occurred in the northern Paradox Valley area on January 24, 2013 (Block et al., 2014b). In response to this earthquake, injection was halted while a reassessment of the seismic hazard associated with PVU injection was performed. Analyses of the seismic and injection data indicated that the potential for inducing large felt events could be reduced by decreasing the long-term average injection pressures (Block and Wood, 2009; Wood et al., 2016). Pressure-flow modeling indicated that reducing the flow rate would reduce wellhead pressures, and forward modeling was used to determine an appropriate flow rate (Wood et al., 2016). In addition, the pressure-flow modeling indicated that changing the injection well shut-in schedule to have shorter, more frequent shut-ins would result in a lower average wellhead pressure, compared to the biannual 20-day shut-ins previously used.

As a result of these analyses, the decision was made in April 2013 to reduce the injection flow rate, and to increase the frequency of injection well shut-ins while reducing their duration (Block et al., 2014a). Due to a delay in obtaining plungers that would allow injection at a lower flow rate, injection was initially resumed on April 17, 2013, maintaining the flow rate at 230 gpm and implementing a 36-hour shut-in every week. On June 6, 2013, following the acquisition and installation of the new plungers, the flow rate was reduced to 200 gpm and the shut-in duration was reduced to 18 hours. The frequency of one shut-in per week was maintained. A shut-in duration of 18 hours was chosen so that the total annual shut-in time would be approximately equivalent to that scheduled previously with the biannual 20-day shut-ins. Hence, the nominal flow rate during Phase V (200 gpm) was decreased by 13% from that during Phase IV (230 gpm), and the total duration of planned shut-ins remained the same.

Because of the frequency of the new shut-in schedule, the durations of any unplanned shut-ins (such as those periodically required for equipment maintenance) are tracked, and those hours are subtracted from the duration of the weekly scheduled 18-hour shut-in. The durations of unplanned shut-ins had not been tracked and subtracted from the biannual 20-day shut-ins during earlier injection phases, and hence the total shut-in time during previous years had sometimes increased substantially, depending on the number and duration of unplanned shut-ins required. Hence, while the nominal flow rate during Phase V was decreased by 13% from that during Phase IV, the effective decrease in flow rate has been less than this value due to the difference in total shut-in time. The average flow rate during Phase V (from April 17, 2013 to December 31, 2013) has been 180 gpm, which is ~8% less than the average flow rate of 196 gpm during the previous three years (2010-2012).

Pressure-flow modeling of Phases I-IV only is included in this analysis; pressure-flow modeling of Phase V is still in the beginning stages.

4 Pressure-Flow Modeling

Pressure-flow modeling can help with understanding the reservoir behavior by focusing on a few basic parameters such as permeability and skin effect, and analyzing their evolution over time. Such modeling can be used to determine whether recorded changes in wellhead pressures are more likely the result of changes in the near-wellbore properties, or whether a fixed set of reservoir parameters are adequate to fit the recorded pressures over long time periods.

4.1 Previous Work

One of the key parameters that defines reservoir behavior is the effective permeability. Previous estimates of permeability have varied. Drill stem tests using a variable flow rate gave an original permeability of 7.97 mD (Harr, 1989). However, Horner analysis performed at the same time indicated a permeability between 1.3 and 1.5 mD (Harr, 1989). Additionally, analysis of core samples from the Conoco-Scorup well located approximately 4.6 km to the northeast yielded permeabilities ranging from 0.03 to 1.3 mD (Harr, 1989), which could suggest significant regional variations in permeability.

A series of seven injection tests were performed between 1991 and 1995. Permeabilities were only calculated for the first three tests, which took place between July 11, 1991 and June 18, 1992, primarily due to equipment failures in later tests. The permeabilities for the first injection and falloff periods were calculated as 4-5 mD and 2 mD, respectively. The second injection and falloff periods yielded 7.8 mD and 2.2 mD, respectively. The third falloff period yielded a permeability of 1.6 mD, while the third injection period was determined to be unanalyzable due to numerous flow rate changes caused by equipment failure. The lower permeabilities calculated during falloff periods, as compared with injection periods, were assumed to indicate fracture closure (Envirocorp Services and Technology Inc., 1995).

An early model of the injection test data attempted to fit the data from the seventh and final injection test, which took place from August 14, 1994 to April 3, 1995, using a fracture network model with 5% porosity and a permeability of 3 mD (Envirocorp Services and Technology Inc., 1995). While they obtained reasonable fits to the data from this injection test, their model predicted future pressures that were significantly lower than recorded pressures. While the modeled injection scenarios differ from the actual injection scenarios, preventing a direct comparison, their model predicted that surface pressure would not exceed 4500 psi after ten years of continuous injection at a flow rate of 300 gpm. In contrast, the recorded pressures exceeded 4500 psi after less than four months of injection at an average flow rate of 163 gpm. This suggests that the effective permeability-thickness and/or porosity-thickness were overestimated in this early modeling.

In 2001, Reclamation funded USGS to perform fluid-flow modeling of the 1996-2000 pressure and flow data using a poroelastic model, and a draft report was received in 2009 (Roeloffs and Denlinger, 2009). The USGS model consisted of a radially-symmetric finite element grid with

twenty layers based on stratigraphy, each characterized by four parameters (shear modulus, Poisson ratio, Skempton's coefficient, and hydraulic diffusivity). The model was calibrated by trial-and-error matching of the predicted flows and pressures with those measured at the wellhead. For the layer representing the Leadville formation, a porosity of 10% and a permeability of 28 mD were assumed for a thickness of 146 meters (479 feet), with significantly lower values for other layers. In contrast, Bremkamp and Harr (1988) determined a porosity in the Leadville of ≥10% for only 2 feet of its 416-foot thickness, using sonic logging, or 18 feet, using visual binocular examination of recovered core. Hydraulic diffusivity (calculated from permeability, formation thicknesses, porosity, and shear modulus), was found to be the parameter most strongly effecting pressure distribution in the model. The USGS model did not incorporate skin factor or wellbore storage parameters.

The USGS model provides a reasonably good fit to the flow rate data for approximately the first 500 days, but then the modeled flow rates begin to decrease, while the measured flow rates remain approximately constant. Roeloffs and Denlinger (2009) suggest that formation permeability may have increased, or that the flow may have reached a zone of higher permeability away from the well.

The permeability of intact limestone and dolomite generally varies from 0.01 to 0.1 mD (Bear, 1972). The permeability value for intact rock is known as primary, or matrix, permeability, and is generally only applicable to laboratory samples, as rocks over larger scales will contain at least some degree of fracturing. Limestones may also have increased permeability due to vugular porosity. The permeability due to fracturing and secondary porosity is known as secondary permeability and can vary by several orders of magnitude, even exceeding 10^5 mD in some highly fractured locations (Cox and others, 2000). Thus, the estimated permeabilities of a few mD, while higher than would be expected to be measured under laboratory conditions, are reasonable for a moderately fractured reservoir.

4.2 Fitting of Pressure-Flow Data to Idealized Models

It was unclear initially whether complicated numerical models were required to fit the pressure-flow data at the wellhead, or instead if simple idealized models would suffice. In the absence of monitoring wells or other independent means of verifying predicted pressures within the injection reservoir at distances away from the wellbore, the use of excessively complex models may result in overfitting of the wellhead data, and a correspondingly poor predictive capability of the models for future data. We therefore tried fitting the data for individual injection and shut-in cycles using several simple, idealized models commonly employed in the well-testing and reservoir-modeling industry. F.A.S.T. WellTest software v.7.6.0, described in Fekete (2012), was used for this analysis.

Biot (1941) developed a model of a fluid-filled porous material based on a conceptual model of a coherent solid skeleton and freely moving pore fluid (Detournay and Cheng, 1993). Under this model, for the case of an isotropic applied stress tensor σ, the constitutive equations are,

$$\begin{aligned} \varepsilon &= a_{11}\sigma + a_{12}p \\ \varsigma &= a_{21}\sigma + a_{22}p \end{aligned} \tag{4.1}$$

where ς is the increment of fluid content, p is the fluid pressure, and ε is the volumetric strain (Wang, 2000). This model includes full coupling between the solid and fluid components. Substituting physically meaningful constants, the most general form of the linear constitutive equations for isotropic material response is:

$$\begin{aligned} \varepsilon_{ij} &= \frac{\sigma_{ij}}{2G} - \left(\frac{1}{6G} - \frac{1}{9K}\right)\delta_{ij}\sigma_{kk} + \frac{1}{3H}\delta_{ij}p \\ \varsigma &= \frac{\sigma_{kk}}{3H} + \frac{p}{R} \end{aligned} \tag{4.2}$$

where K and G are the bulk modulus and shear modulus of the drained elastic solid, and H, and R are constitutive constants characterizing the coupling between the solid fluid stress and strain (Detournay and Cheng, 1993).

At reservoir depths, the rock compressibility is generally small, and thus a simplifying assumption may be made in order to uncouple the solid and fluid components. This is a common simplification in reservoir modeling applications, and is used in our analysis.

For the uncoupled, incompressible rock assumption, the governing equation for radial flow in cylindrical coordinates is:

$$\frac{\partial^2 p}{\partial r^2} + \frac{1}{r}\frac{\partial p}{\partial r} = \frac{\phi c_t \mu}{k}\frac{\partial p}{\partial t} \tag{4.3}$$

where r is the radial distance from the well in centimeters, t is time in seconds, p is the reservoir pressure in atmospheres at distance r and time t, ϕ is the formation porosity as a fraction of bulk volume, k is the formation permeability in Darcies, μ is the fluid viscosity in centipoises, and c_t is the total compressibility in volumes per volume per atmosphere (Horner, 1951).

For a point source, the change in pressure resulting from an applied flow is:

$$p - p_0 = \frac{q\mu}{4\pi kh}\mathrm{Ei}\left(\frac{r^2\phi\mu c_t}{4kt}\right) \tag{4.4}$$

where p_0 is the initial reservoir pressure in atmospheres at $t = 0$, q is a constant rate of production of the well (starting at $t = 0$) in cubic centimeters of subsurface volume per second, h is the layer thickness in centimeters, $\mathrm{Ei}(x); x > 0$ is the exponential integral (Abramowitz

and Stegun, 1964), and other variables are the same as in Equation (4.3). This solution assumes an infinite reservoir and an infinitely small wellbore radius (Horner, 1951).

For sufficiently small $x > 0$, $\mathrm{Ei}(x)$ may be accurately approximated by $\mathrm{Ei}(x) \approx \gamma + \log(x)$, where γ is Euler's constant (Abramowitz and Stegun, 1964). Thus if the parameters of the model are homogeneous and constant over time, then Equation (4.4) may be approximated as:

$$p - p_0 = -\frac{q\mu}{4\pi kh}\log\left(\frac{4kt}{r^2\phi\mu c_t}\right) + const. \tag{4.5}$$

which shows that for continuous injection $q < 0$, the pressure change at the wellbore radius r_w is asymptotic to $\log(t)$, and with a slope inversely proportional to the permeability-thickness product kh.

Typical well-testing procedures consider a period of constant production starting at time $t = 0$, followed by a shut-in period starting at time $t_0 > 0$, then the well pressure during the shut-in period at time $t_0 + \tau$, can be obtained by superimposing two equations of the form of Equation 4.4. Using the wellbore radius r_w for *r*, this leads to the equation:

$$p_w - p_0 = \frac{q\mu}{4\pi kh}\left[\mathrm{Ei}\left(\frac{r_w{}^2\phi\mu c_t}{4k(t_0+\tau)}\right) - \mathrm{Ei}\left(\frac{r_w{}^2\phi\mu c_t}{4k\tau}\right)\right] \tag{4.6}$$

where p_w is the pressure at the wellbore in atmospheres and r_w is in centimeters. Using the previous approximation for $\mathrm{Ei}(x)$ at small $x > 0$, the pressure change during the shut-in period described by Equation (4.6) may be approximated as:

$$p_w - p_0 = -\frac{q\mu}{4\pi kh}\log\left(\frac{t_0+\tau}{\tau}\right) \tag{4.7}$$

For continuous injection $q < 0$, Equation (4.7) shows that the pressure fall-off at the wellbore radius following shut-in is asymptotic to $\log\left(\frac{t_0+\tau}{\tau}\right)$, where t_0 is the injection duration, τ is the time since shut-in, and where the slope is inversely proportional to the permeability-thickness product kh. Horner (1951) demonstrates that the error introduced by this approximation typically drops to 0.25% within seconds of closing the well.

In dimensionless variables, the governing equation equivalent to Equation (4.3) is:

$$\frac{\partial^2 p_D}{\partial r_D{}^2} + \frac{1}{r_D}\frac{\partial p_D}{\partial r_D} = \frac{\partial p_D}{\partial t_D} \tag{4.8}$$

where, in arbitrary units, $r_D = r/r_w$ is the dimensionless radial distance from the well, $t_D = \frac{kt}{r_w^2 \phi \mu c_t}$ is dimensionless time, and $p_D = \frac{kh}{q\mu}(p - p_0)$ is the dimensionless pressure change on the formation side at distance r_D and time t_D (Agarwal et al., 1970). Using the previously defined units, the equations for r_D and t_D are unchanged, while the equation for p_D becomes $p_D = 0.0689\frac{kh}{q\mu}(p - p_0)$. All model properties are assumed to remain constant with time, and pressure is calculated based on the recorded injection rate, which varies over time.

In solving Equation (4.8) for a finite wellbore, two additional variables, the wellbore storage constant and skin factor, are introduced in the inner boundary conditions, in order to ensure continuity across the wellbore boundary. In dimensionless variables, the boundary conditions are:

$$C_D \frac{dp_{wD}}{dt_D} - \left(\frac{\partial p_D}{\partial r_D} \right)_{r_D=1} = 1 \qquad (4.9)$$

and

$$p_{wD} = \left[p_D - s\left(\frac{\partial p_D}{\partial r_D} \right) \right]_{r_D=1} \qquad (4.10)$$

where p_{wD} is the dimensionless pressure drop within the wellbore, C_D is the dimensionless wellbore storage constant, s is the dimensionless skin factor, and other parameters are the same as in Equation (4.8) (Agarwal et al., 1970). All fluid and rock properties are assumed to remain constant.

Our analysis uses the recorded injection flow rates and surface pressures recorded at the PVU wellhead since continuous injection began in 1996. The sample rate of that data is non-uniform over time. Injection data prior to 2003 were recorded on an older supervisory control and data acquisition (SCADA) system in a format that is currently inaccessible. For this period, only daily average pressures and flow rates are available. Starting in 2003, data are available at much higher sample rates (up to 1 sample every 2 seconds) due to the installation of a newer SCADA system. Mixing data at the two sample rates was found to create artificial trends in the data. For example, a large apparent decrease in the wellbore storage constant occurred when mixing the daily-average with the high-frequency data. While misfits were lower using data with the higher sample rate, and the absolute values obtained for parameters were likely more accurate, the trends in the parameters over time are more significant to this analysis than their particular values. It was therefore decided to use the daily average data over the entire well operating history for this analysis.

Reservoir temperature is a significant factor affecting the modeling, primarily because of its effect on the fluid viscosity, as the temperature of the injectate is generally assumed to be equal to the undisturbed reservoir temperature. While this assumption is probably adequate for short-term injection testing, the volume of fluid that has been injected into PVU Injection Well #1 has likely led to cooling of the reservoir at a significant distance from the well, and thus the reservoir temperature varies in both time and space. However, as the model cannot account for temperature variations, and as there are no data to constrain temperatures away from the well, a single temperature was used for the modeling. A temperature of 37.8˚C was used, corresponding to the temperature measured near the base of the Leadville formation three days into a shut-in that occurred in March 1994 (Subsurface Technology, 2001).

Other input parameters include a reservoir thickness of 100 feet (30.5 meters), porosity of 3%, and salinity of 2.60 kg/L after January 8, 2002, when injection of 100% brine began, and 1.82 kg/L prior to this date, when the injectate was a mixture of 70% brine and 30% fresh water. The salinity of the fresh water was assumed to be negligible relative to the brine, and therefore a salinity of 70% of that for the brine was used for the mixture. The assumed thickness of 100 feet is approximately equal to the thickness of the perforated interval of the upper Leadville, as logging has indicated that the middle and lower Leadville perforations are covered with fill (Subsurface Technology, 2001) and thus accept a significantly lower amount of flow. It is unknown to what extent fluid is able to migrate vertically outside of the perforated interval in the vicinity of the wellbore.

Viscosity and fluid compressibility are calculated using the temperature and salinity, but variation of these parameters over time is not included in this analysis. The calculated viscosity is 1.030 cP during the injection of 70% brine and 1.348 cP during the injection of 100% brine. The calculated fluid compressibility is 1.933×10^{-6} psi^{-1} during the injection of 70% brine and 1.731×10^{-6} psi^{-1} during the injection of 100% brine.

While the assumed model parameters have a significant effect on the absolute values of the calculated permeability, the effect on the relative permeability values between cycles is minimal, and thus we do not expect our interpretations to be significantly affected by the choice of model parameters. For example, if a value of 479 feet had been used for the layer thickness, roughly equal to the thickness of the entire Leadville formation, the calculated permeabilities would be reduced by a factor of 4.79, but the ratios of permeabilities between cycles would not be affected. Variations in model parameters in space or time, such as a change in thickness of the Leadville away from the well or reservoir cooling over time, could potentially have more significant effects, but the model cannot account for changes in these parameters, and there are only limited data to constrain such changes.

Downhole pressures were calculated by adding a constant value to the surface pressures, accounting for the weight of the brine and the frictional effect due to flow, assuming new tubing conditions with no scale buildup inside the tubing (Mahrer et al., 2004). The friction term is negligible for the injection rates and tubing size used at PVU. It is possible that the friction term becomes more significant over time due to scale build-up, but as well logging has not been performed at PVU since 2001 (due to the substantial cost and risk to the wellbore that would be

involved in such logging), the current conditions are unknown and therefore the potential changes in friction have not been incorporated into the analysis. A constant pressure difference between the wellhead and downhole pressure of 6822 psi was used for continuous injection Phases I-III, and 7133 psi for injection Phase IV, when injectate density increased as a result of the switch to 100% brine.

After comparisons of several different models supported by the Fekete software, a radially symmetric model was selected. This model has no-flow boundaries in the vertical direction and infinite-acting boundaries in the horizontal directions. Models with no-flow or constant pressure boundaries in the x- and/or y-directions were also considered, as well as radial composite models and models incorporating fractures and anisotropic permeability. However, these models provided either a worse fit or an insignificant improvement in the fit to the data, so the simplest model that adequately fit the data was selected.

There is some evidence that a radial composite model with a decreased permeability in the near-well area may provide an improved fit over a radial flow model, particularly from the two long (68-day and 83-day) falloff periods that occurred in 2005-2006 and 2013, respectively. However, for buildup cycles, as well as for falloff periods of standard duration (~20 days), the improvement in fit is insufficient to justify adding additional free parameters. Additionally, the decrease in permeability in the near-well area is relatively minor and does not appear to change significantly with time, supporting the validity of a radial flow model to adequately fit the pressure-flow data.

While the radially symmetric model does not incorporate individual fractures, the estimated downhole pressures are frequently above the fracture propagation pressures (Envirocorp Services and Technology Inc., 1995), and thus the near-wellbore region is expected to be so extensively fractured as to be adequately represented as a porous medium, particularly in recent years.

There are three free parameters in the selected model: the effective permeability, k, skin due to damage in the near-wellbore region, s_d, and dimensionless wellbore storage constant, C_D. The entire flow rate history is incorporated into the calculation of modeled pressures. First, the parameters are fit individually for each buildup period. This approach is used to assess whether these parameters have changed over time, and because there was no clear reason for assuming that a single set of parameters would be adequate to fit all the data. Second, a single set of parameters is used to fit multiple buildup periods. This approach is used to assess whether a single set of parameters adequately fits multiple injection periods.

For Phases II-IV, when two twenty-day shut-ins were scheduled every year, a cycle is defined to be the build-up period between two scheduled shut-ins. Unscheduled 11-day and 17-day shut-ins occurred in the cycles beginning July 26, 1999 and January 21, 2006, respectively, so these flow periods were each split into two cycles for this analysis. All cycles contain unscheduled shut-ins, primarily due to equipment issues, which range in duration from a few hours to ten days. In order to analyze the six-month cycles as a single flow period despite the short shut-ins, it is necessary to input a small but non-zero flow rate for the short shut-in periods.

For Phase I, cycles are defined as the flow periods between two unscheduled multi-day shut-ins, which range in duration from four to seventy days. Cycles range from 47 to 345 flow days in duration; build-up periods of only a few days are excluded from analysis.

Defining cycles in this matter leads to a total of 38 cycles: 7 in Phase I, 3 in Phase II, 4 in Phase III, and 24 in Phase IV.

4.3 Results of Pressure-Flow Model Fitting

Using the first approach described previously, the model parameters for each injection cycle were fit simultaneously, using a Simplex automatic parameter estimation procedure to find a local minimum in the misfit between the data and the model. All parameters for each injection cycle were fit independently from the other injection cycles. Section 4.3.1 describes how the computed model parameters have evolved over the various phases of injection. Section 4.3.2 describes the quality of the model fits to the pressure-flow data. Section 4.3.3 provides further discussion of possible changes in permeability at significant distances from the injection well. Following the second approach described previously, section 4.3.4 shows the results of fitting multiple cycles simultaneously.

4.3.1 Changes in Model Parameters over Time

In Phase I, modeled values for k range from 9.06 to 10,200 mD, and values for s_d range from -5.82 to 2000, with a strong positive correlation between these two parameters. Values for C_D range from 6.27×10^5 to 1.46×10^6. The magnitude of variations in k and s_d is believed to be an artifact of attempts by the modeling algorithm to fit data that include factors that the model cannot account for. In particular, the model seems to be unable to fit periods of frequent flow rate changes. Figure 4-1 demonstrates this for an example Phase I cycle, beginning May 30, 1998. Figure 4-1a shows the best fit parameters. Note that the model is not able to capture the shape of the pressure curve especially well at any point during the cycle. Figure 4-1b shows the model with manually determined parameters that are believed to be more physically realistic. These parameters fit the data well during the beginning part of the curve, when the flow rate is nearly constant at 345 gpm. However, once the pressures begin approaching 5000 psi and the flow rate was frequently changed between 115, 230, and 345 gpm (as discussed in Section 3.1), the modeled pressures begin to deviate significantly from the measured pressures. This may be due to a variety of factors, including using a sample rate with a lower frequency than the flow rate changes.

In Phase II, the variation in model parameters is much smaller than found in Phase I, with k ranging from 13.6 to 21.9 mD, s_d ranging from -6.05 to -3.99, and C_D ranging from 8.80×10^5 to 1.37×10^6.

In Phases III and IV, for twenty-seven of the twenty-eight cycles in these phases, effective permeabilities range from 10.4 to 29.2 mD, with a mean of 18.0 mD and median of 16.7 mD, and skin values range from -5.98 to -1.98, with a mean of -4.35 and median of -4.62. The permeability and skin both appear to increase somewhat during Phase III, while in Phase IV neither of these parameters shows any clear trends with time, as shown in Figure 4-2.

The remaining cycle initially appeared to be a significant outlier, with a modeled permeability of 140 mD and skin value of 26.3. This cycle, which began March 4, 2006, contained a period of about a month near the beginning of the cycle where the flow rate fluctuated frequently between 115 gpm and 230 gpm. As in Phase I, these rapid flow rate changes appear to cause instability in the modeling algorithm. For this reason, the permeability and wellbore storage constants were re-fit after fixing the value of s_d at the mean of the preceding and following cycles. This led to a permeability of 20.7, with a minimal increase in the misfit.

Modeled dimensionless wellbore storage constants for Phases III-IV vary from 9.01×10^5 to 1.74×10^6, which correspond to dimensional wellbore storage constants of 4.17 to 8.03 ft^3/psi. These values are significantly larger than the value expected from considering only the actual wellbore volume, which is on the order of 1 ft^3/psi, suggesting that the fractured area around the well may essentially be acting as an enlarged wellbore or an extension of the wellbore (Fekete, 2012). The wellbore storage constants are somewhat higher prior to mid-2002, with a decrease of about 21% between the mean values from September 1999 to January 2002 (the beginning of Phase IV, when the change from injection of 70% brine to injection of 100% brine occurred) and the mean values beginning with June 2002 (Figure 4-2b). The magnitude of the decrease between the mean of the cycles in these two time periods is approximately 2.94×10^5, which is 2.6 times the standard deviation of the wellbore storage constants beginning in June 2002, indicating that the decrease is statistically significant. It is possible that the decrease in the modeled wellbore storage constant indicates a decrease in the perforated interval of the wellbore due to narrowing of the wellbore and/or precipitation of elemental sulfur, both of which have been observed in past wireline logs (Subsurface Technology, 2001). There may also be precipitation of anhydrite in the fractures surrounding the wellbore, which was predicted by Kharaka et al. (1997) as a result of geochemical analyses. However, it is not clear why precipitation would cause a sudden decrease in the wellbore storage constant followed by a long period of relatively stable values, rather than a gradual decrease.

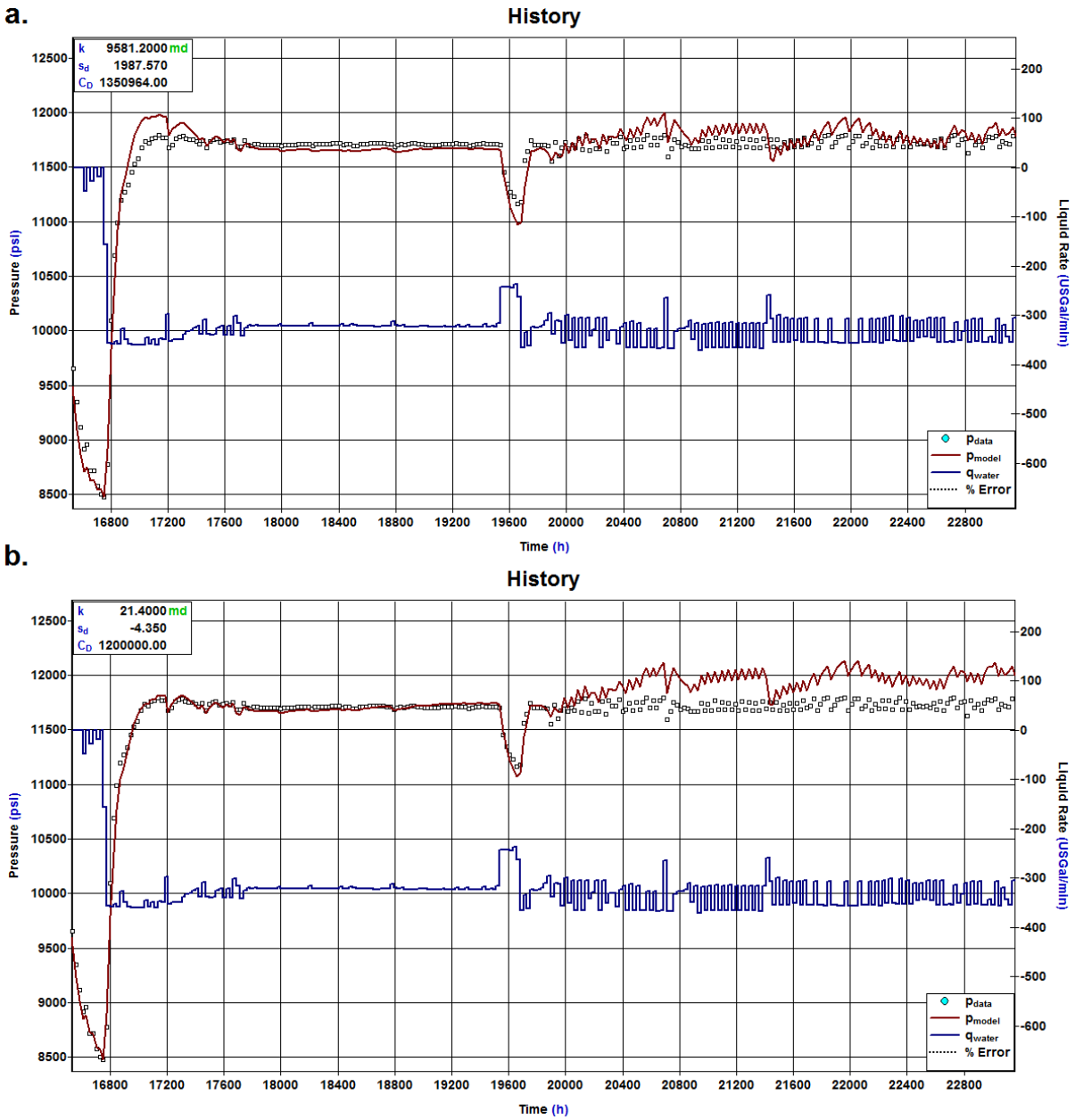

Figure 4-1. Recorded (blue dots) and modeled (red line) downhole pressures, fit using (a) best-fit parameters and (b) manually determined parameters for an example Phase I cycle, beginning May 30, 1998. Blue lines indicate recorded flow rate. Recorded downhole pressures are calculated by adding a constant value of 6822 psi to measured surface pressures. The model has difficulty fitting the data during periods of frequent flow rate changes, such as occurred after hour 19,600.

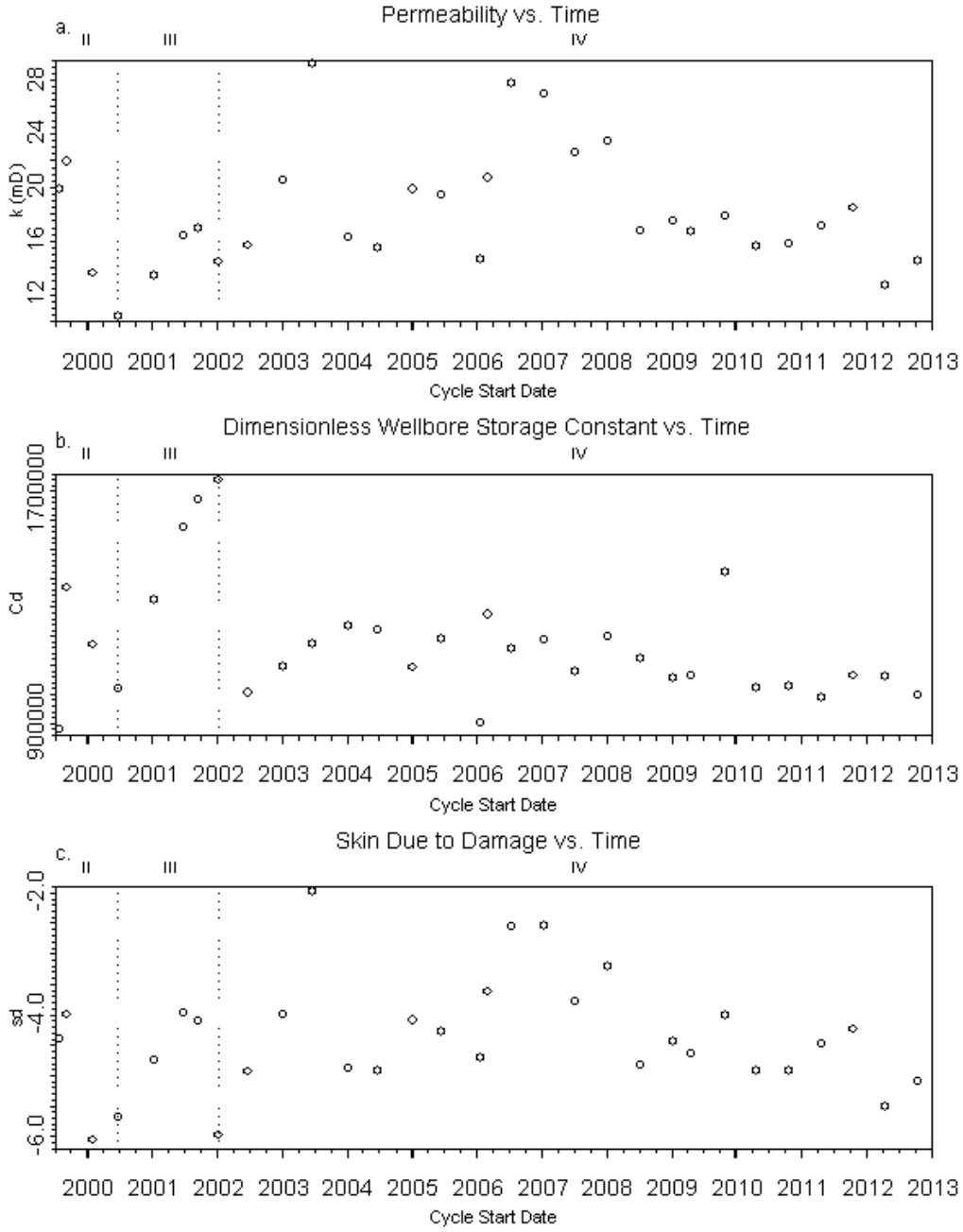

Figure 4-2. Effective permeability (a), dimensionless wellbore storage constant (b), and skin due to damage (c) versus time for pressure build-up cycles in Phases II-IV. Dashed lines indicate boundaries of the injection phases.

There is significant tradeoff between the model parameters, as indicated by the strong positive correlation between the values of k and s_d shown in Figure 4-3, leading to concern that the resulting parameters may not be robust. In order to minimize the tradeoff, the values for k and C_D are refit after fixing s_d at a value of -4.35. This value for s_d corresponds to the mean of the calculated values for the cycles in Phases III and IV.

Fixing s_d leads to much less variation in the values obtained for k, particularly those in Phase I and Phase II (Table 4-1). The values for all cycles vary from 14.02 to 27.12, with a mean of 18.76 and median of 18.36. With the exception of an outlying cycle in 2002, the values are highest during Phases I and II, when the injection rate was higher, then lowest during Phase III, and have remained relatively constant since Phase IV began in 2002 (Figure 4-4). The outlying cycle coincides with the switch from 70% brine to 100% brine and is likely an artifact of that change, as the changes in fluid viscosity and density do not happen instantaneously as modeled.

Modeling of the injection tests performed from 1991-1995, which varied from 0% to 70% brine, indicate a positive correlation between salinity and permeability, suggesting that the increase in permeability between Phase III and Phase IV may be due to the switch to 100% brine, which increases the fluid density and downhole pressure and may assist in keeping fractures open. A comparison between the parameters with s_d allowed to vary or fixed is shown in Table 4-1.

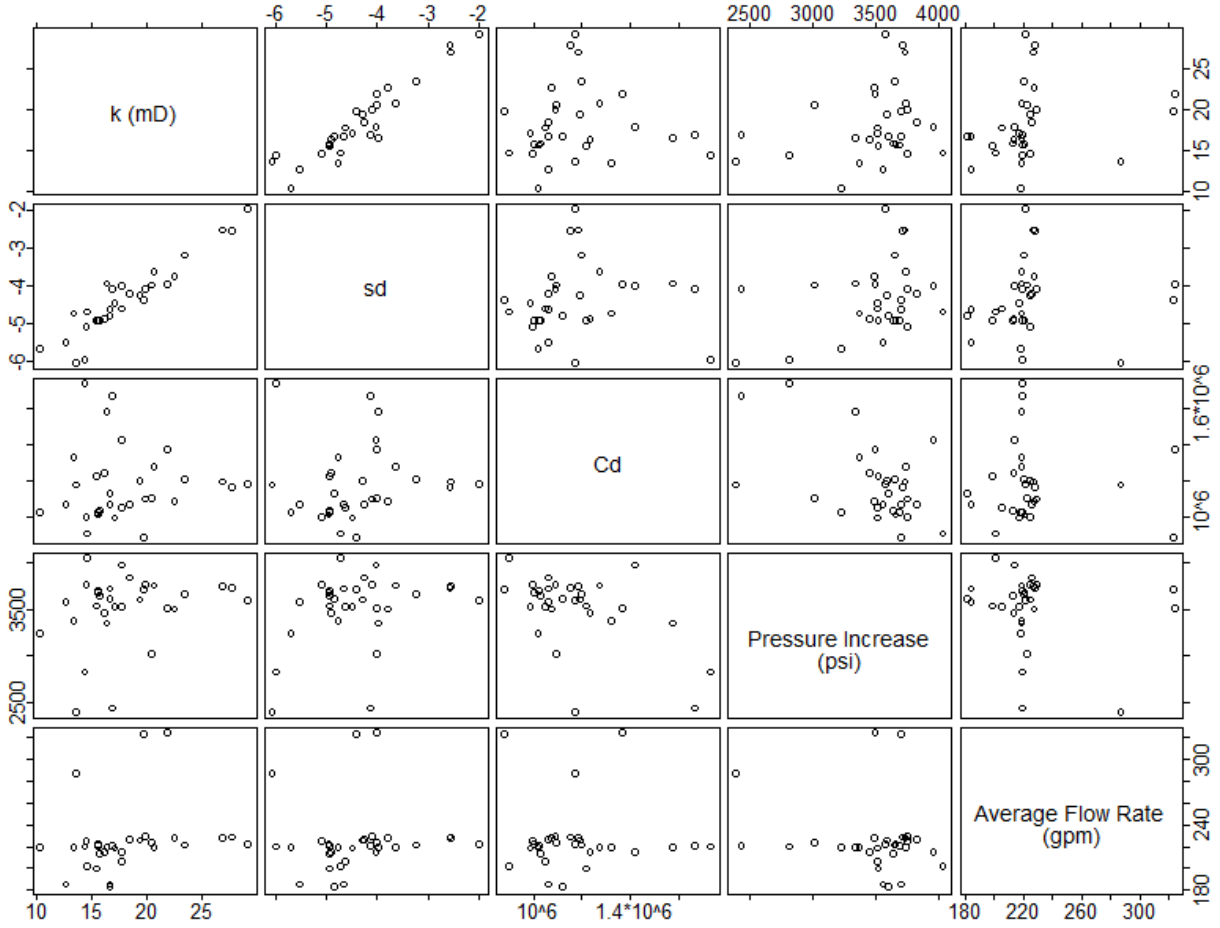

Figure 4-3. Scatter-plot matrix showing pairwise correlations between modeled permeability (k), skin due to damage (s_d), dimensionless wellbore storage constant (C_D), recorded pressure increase, and average recorded flow rate for all pressure build-up cycles in Phases II-IV. Note the strong correlation between modeled permeability and skin.

Table 4-1. Permeability (k), skin due to damage (s_d), and dimensionless wellbores storage constant (C_D) fit with three free parameters, and k and C_D fit with s_d fixed at -4.35 for all cycles.

		s_d allowed to vary			s_d fixed at -4.35	
Phase	**Start Date**	k	s_d	C_D (x10^5)	k	C_D (x10^5)
Phase I	07/22/1996	9.06	-5.82	6.27	14.0	7.99
	09/14/1996	88.3	12.9	9.45	17.7	6.69
	11/09/1996	7120	2000	6.29	16.3	4.71
	07/10/1997	7620	1920	13.3	20.2	8.11
	12/10/1997	10200	1910	13.5	25.1	8.72
	05/30/1998	9580	1990	14.6	22.9	9.19
	05/16/1999	26.1	-4.47	11.4	27.1	11.1
	Phase I mean	*4960*	*1120*	*10.6*	*20.5*	*8.08*
Phase II	07/26/1999	19.8	-4.40	8.80	20.1	8.58
	09/07/1999	21.9	-3.99	13.7	20.2	13.0
	01/08/2000	13.6	-6.05	11.7	23.4	14.1
	Phase II mean	*18.5*	*-4.81*	*11.4*	*21.3*	*11.9*
Phase III	06/23/2000	10.4	-5.68	10.2	15.7	12.2
	01/08/2001	13.4	-4.75	13.2	14.9	13.4
	06/25/2001	16.4	-3.96	15.8	15.0	14.9
	09/13/2001	17.0	-4.11	16.7	16.0	16.5
	Phase III mean	*14.3*	*-4.63*	*14.0*	*15.4*	*14.3*
Phase IV	01/08/2002	14.4	-5.98	17.4	24.2	18.9
	06/24/2002	15.7	-4.94	10.1	18.2	10.3
	01/08/2003	20.5	-4.00	11.0	18.9	10.0
	06/19/2003	29.2	-1.98	11.7	18.6	10.0
	01/08/2004	16.3	-4.89	12.4	18.9	12.8
	06/21/2004	15.5	-4.92	12.2	18.2	12.9
	01/06/2005	19.9	-4.09	10.9	18.8	10.1
	06/16/2005	19.4	-4.28	11.9	18.8	11.7
	01/21/2006	14.7	-4.71	9.02	16.2	9.16
	03/04/2006	20.7	-3.63	12.7	17.9	8.81
	07/12/2006	27.8	-2.55	11.6	18.7	10.1
	01/14/2007	27.0	-2.54	11.9	18.8	10.0
	07/10/2007	22.6	-3.78	10.8	19.8	10.8
	01/10/2008	23.5	-3.21	12.0	18.3	11.6
	07/08/2008	16.7	-4.82	11.2	19.1	10.4
	01/07/2009	17.8	-4.62	10.5	18.9	10.8
	04/23/2009	16.7	-4.64	10.6	17.6	13.5
	10/29/2009	17.8	-4.01	14.2	16.6	10.5
	04/21/2010	15.6	-4.92	10.2	18.2	10.9
	10/21/2010	15.8	-4.92	10.3	18.4	11.9
	04/22/2011	17.1	-4.47	9.9	17.4	12.7
	10/19/2011	18.5	-4.23	10.6	18.0	10.3
	04/16/2012	12.7	-5.51	10.6	18.0	12.1
	10/18/2012	14.6	-5.09	10.0	17.8	10.9
	Phase IV mean	*18.8*	*-4.28*	*11.4*	*18.5*	*11.3*

The decrease in *k* between Phase II and Phase III may be an effect of fracture closure due to the decrease in flow rate and resultant decrease in reservoir pressure. During Phases III-IV, the pressures have gradually increased to the high values seen in Phase II, even surpassing these pressures in recent years. One would expect that the increase in pressure past the Phase II pressures would cause fractures to re-open and permeabilities to return to the values seen in Phase II. However, the permeabilities have remained lower than they were in Phase II, which suggests that the permeability is more sensitive to flow rate than pressure, but the reason for this is unclear. Alternatively, it is possible that the average pore pressures within the radius of investigation of the pressure-flow modeling have remained lower since 2000 than before, if spatial pore pressure gradients have changed sufficiently (see section 4.2.3 for a discussion of the radius of investigation). A substantial change in spatial pore pressure gradients over time to a radial distance of at least 1.1 km is inferred from observed patterns of near-well induced seismicity (see section 5.3.2).

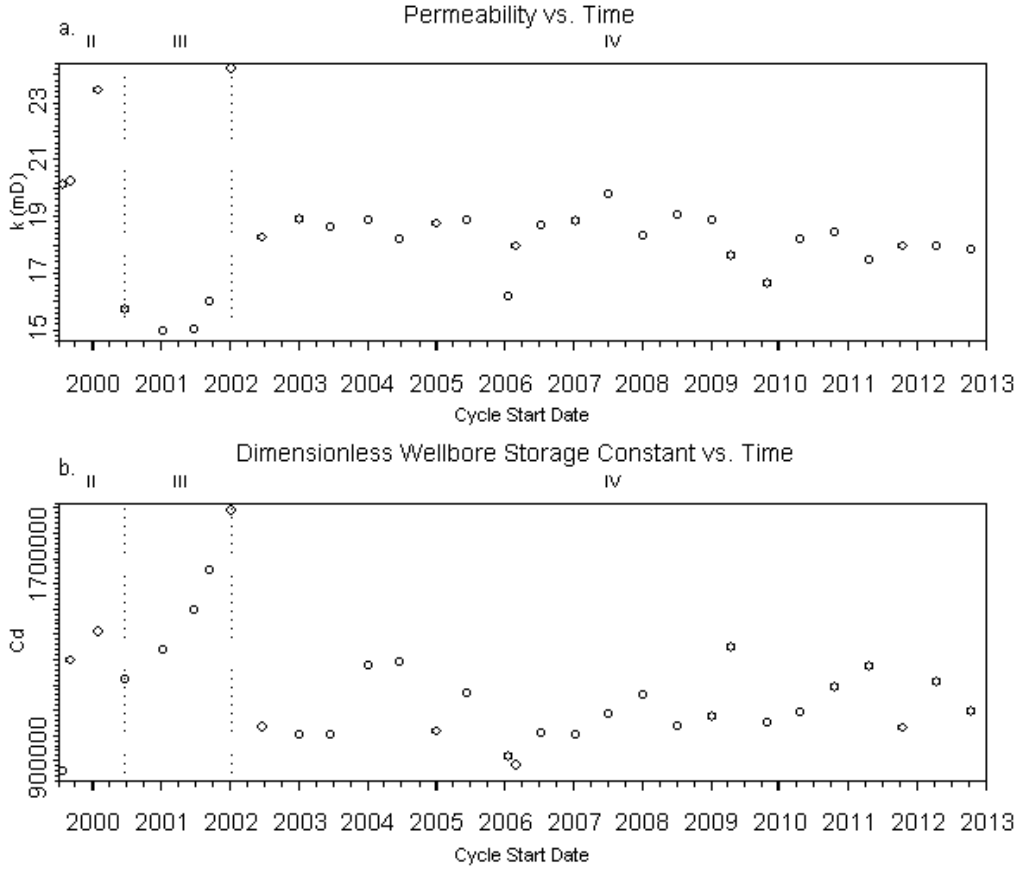

Figure 4-4. Effective permeability (a) and dimensionless wellbore storage constant (b) versus time for all pressure build-up cycles during Phases II-IV, fixing the value of s_d to -4.35. Dashed lines indicate boundaries of the injection phases.

All of the calculated permeability values are higher than those calculated from the early injection tests (Envirocorp Services and Technology Inc., 1995), as discussed in section 4.1. However, a layer thickness of 280 feet was used in these calculations. The values of the product of *kh* that we calculated for the first few injection cycles are consistent with the values calculated for the

injection tests, suggesting that there was not a significant increase in permeability during the injection tests.

The dimensionless wellbore storage constant varies from 4.70×10^5 to 1.89×10^6, corresponding to a dimensional wellbore storage constant varying from 2.18 to 8.73 ft^3/psi. For Phases II- IV, the wellbore storage constant shows a similar trend to the values fit without fixing s_d, with the highest values occurring prior to 2002, a 25% decrease from the mean values prior to June 2002 and the mean values beginning in June 2002, and relatively constant values since 2003. The decrease in the mean wellbore storage constant between January 2002 and June 2002 is 3.1 times the standard deviation of the data beginning in June 2002, again indicating that the decrease appears to be statistically significant.

With the skin value fixed, there do not appear to be significant pairwise correlations between the modeled values of permeability, wellbore storage constant, pressure increase during the cycle, and average flow rate (Figure 4-5).

The degree of tradeoff between the permeability and skin value demonstrates that the values for both parameters cannot be uniquely resolved with the current dataset.

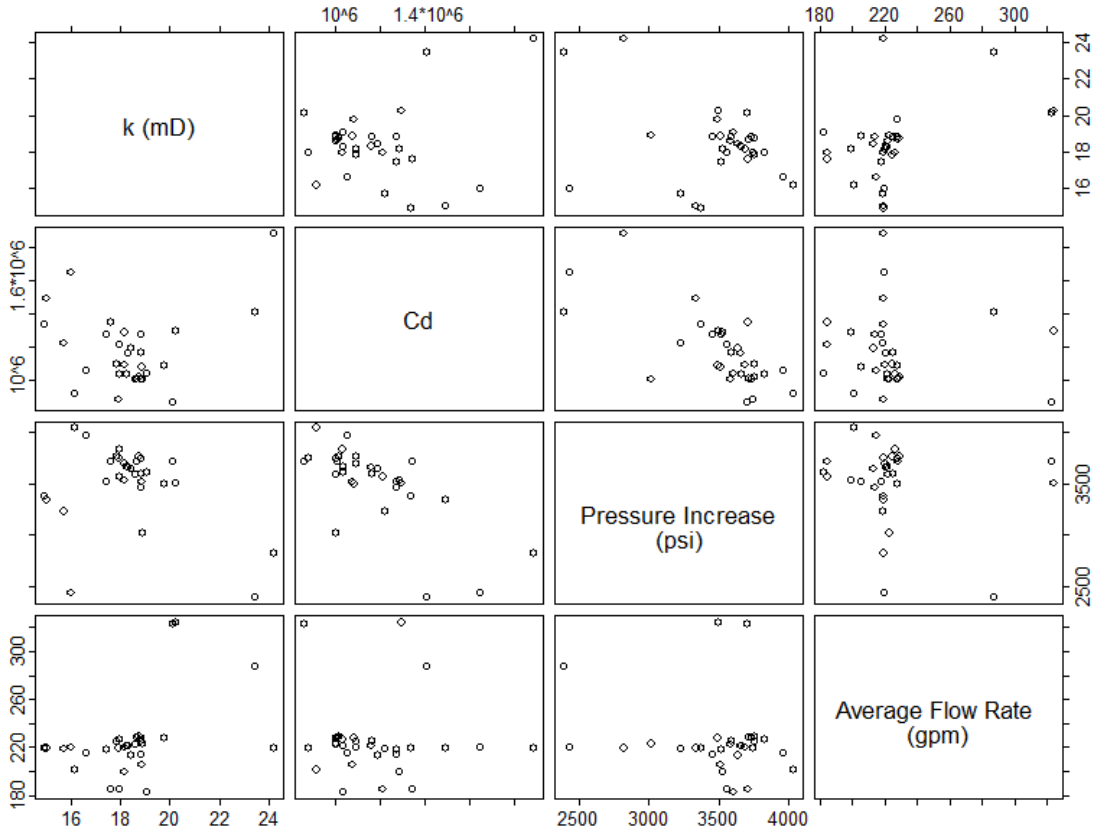

Figure 4-5. Scatter-plot matrix showing pairwise correlations between permeability (*k*), dimensionless wellbore storage constant (C_D), pressure increase, and average flow rate for all pressure build-up cycles in Phases II-IV, holding s_d fixed at -4.35.

4.3.2 Model Pressure-History Plots and Type Curves

For each injection cycle, the free parameters of the model were fit simultaneously, using automatic parameter estimation to find a local minimum in the misfit between the recorded and modeled pressure at the bottom of the well. Downhole recorded pressurs were calculated from the measured surface pressures by accounting for the weight of the brine in the wellbore, and for frictional effects of the flow (Mahrer et al., 2004). Changes in flow rate during an injection cycle, including short shut-ins, were handled using superposition to account for the variable injection rate history. The results of this modeling are a series of pressure-history plots and type curves, one for each injection cycle, which illustrate the modeled flow regime and how well it fits the data. The type curves show the change in pressure divided by flow rate ($\Delta p/q$) and the time derivative of $\Delta p/q$ versus time on a log-log plot.

Pressure-history modeling results from a typical Phase I injection cycle are shown in Figure 4-6. This figure includes results for the case when all three model parameters are allowed to vary (upper plot), and for the case when s_d is held fixed (lower plot).

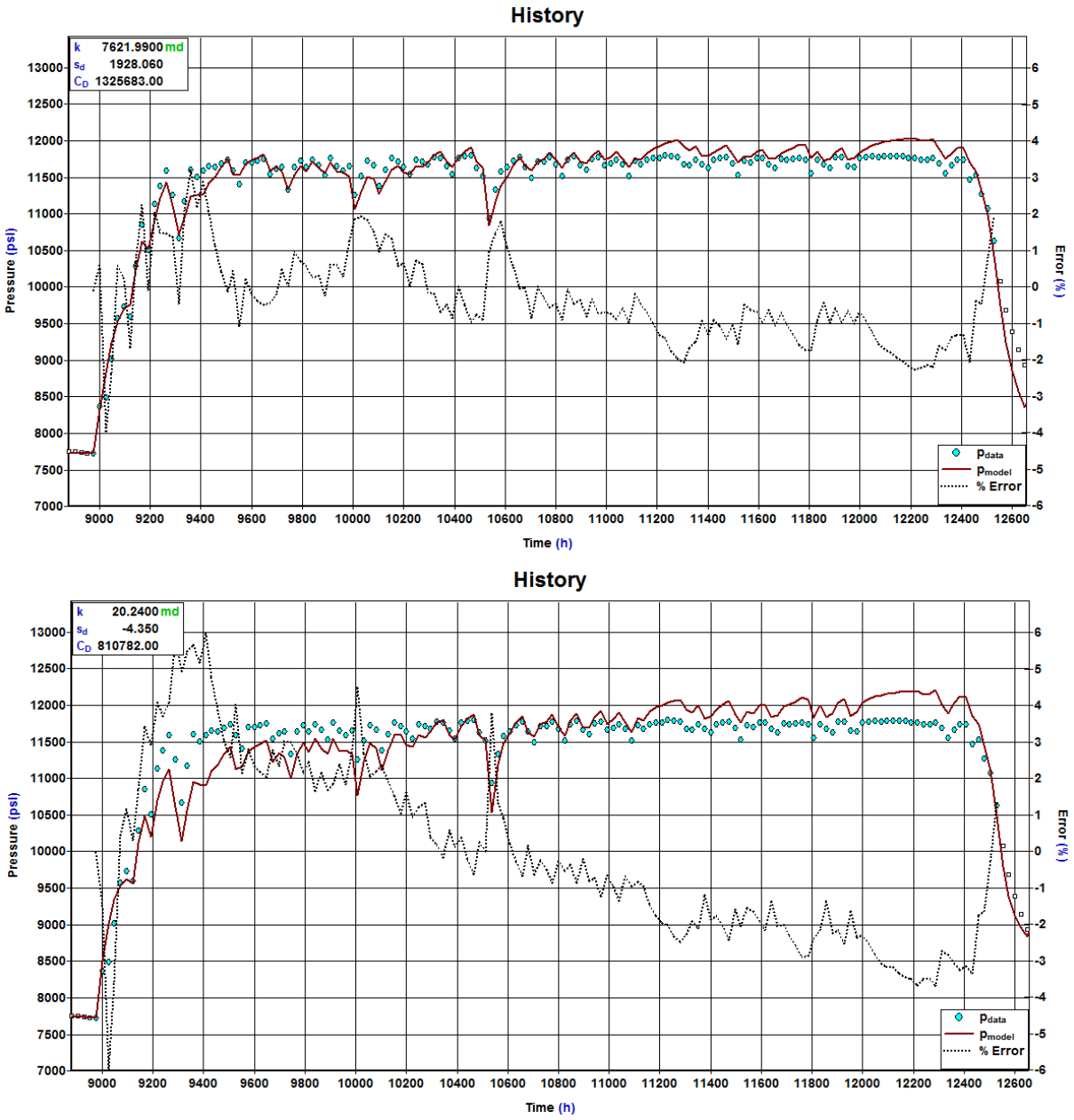

Figure 4-6. Recorded (blue dots) and modeled (red line) downhole pressures and percent error (dashed line) for an example Phase I cycle, beginning July 10, 1997, allowing all three parameters to vary (top) and fixing s_d at -4.35 (bottom). Recorded downhole pressures are calculated by adding a constant value of 6822 psi to measured surface pressures.

The model using three free parameters fits the data significantly better than the model using two free parameters; however, the parameters are not independent, nor are they physically reasonable, as discussed in Section 4.3.1. Regardless, these plots suggest that an idealized radial-flow model can provide a reasonable fit to this data, with errors of less than about 5 percent. The corresponding type curves (pressure change and derivative) are shown in Figure 4-7 and also suggest that a radial-flow model fits the Phase I data reasonably well.

.

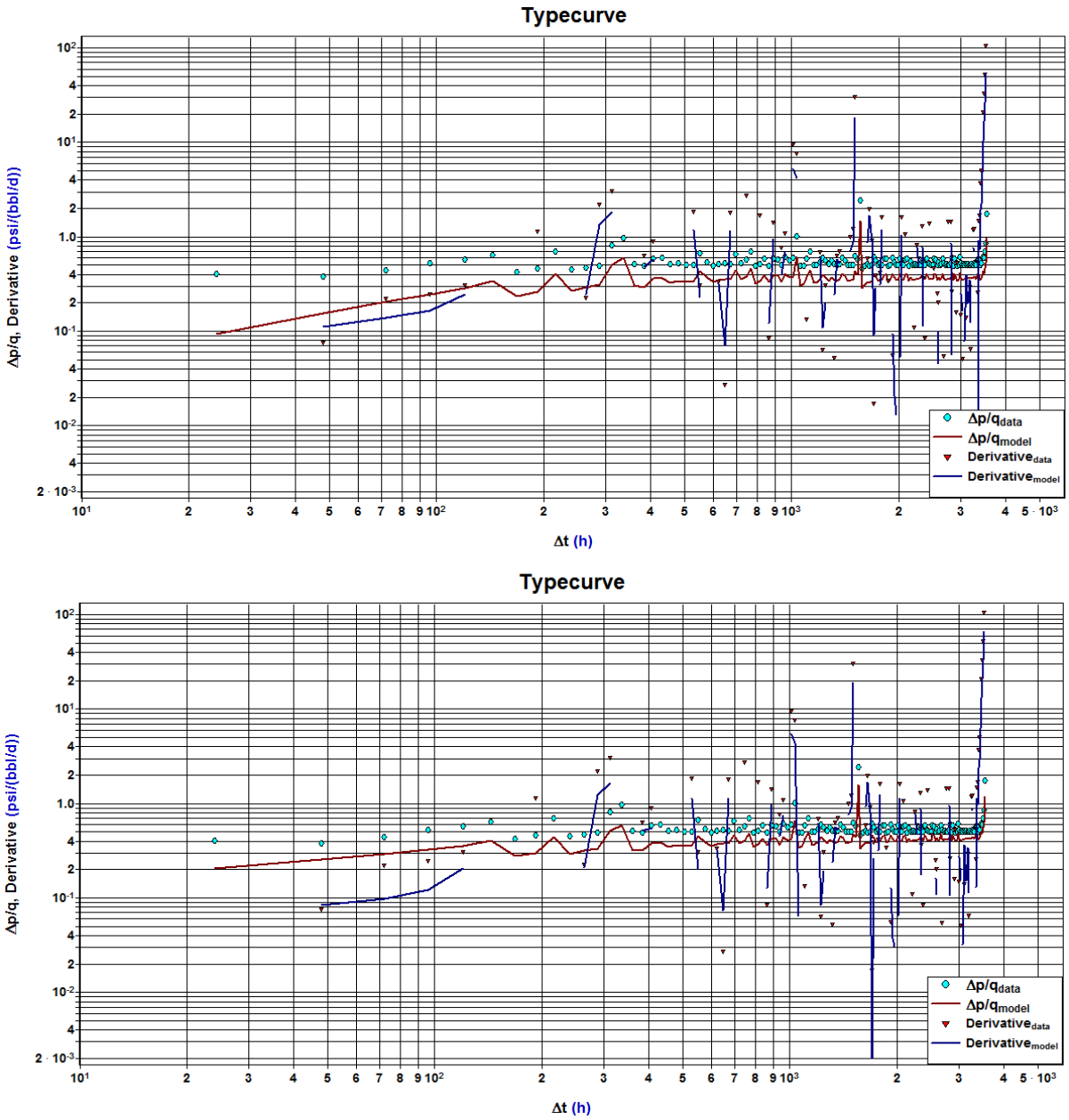

Figure 4-7. Recorded (blue dots) and modeled (red line) values for change in pressure (*Δp*) divided by flow rate (*q*), and the recorded (red triangles) and modeled (blue lines) values for the time derivative of *Δp/q* for an example Phase I cycle, beginning July 10, 1997, allowing all three parameters to vary (top) and fixing s_d at -4.35 (bottom).

Modeling results for typical injection cycles in the remaining phases are shown as follows: Phase II – pressure history (Figure 4-8) and type curve (Figure 4-9); Phase III – pressure history (Figure 4-10) and type curve (Figure 4-11); Phase IV – pressure history (Figure 4-12) and type curve (Figure 4-13). For each phase, the cycle shown is representative of cycles in that phase. Unlike the Phase I cycle, model results from the later phases do not show a significantly greater misfit when s_d is fixed rather than allowed to vary.

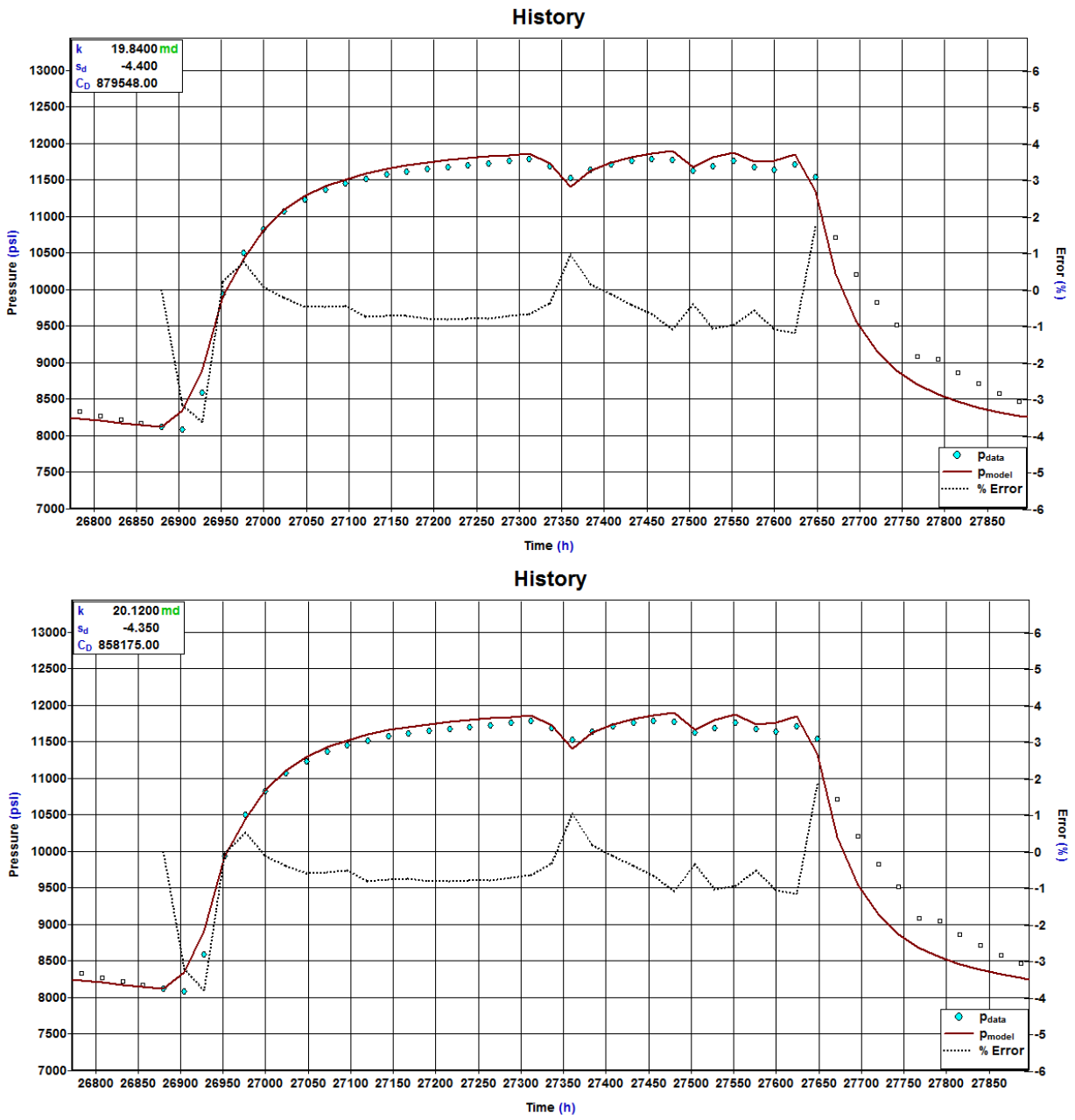

Figure 4-8. Recorded (blue dots) and modeled (red line) downhole pressures and percent error (dashed line) for an example Phase II cycle, beginning July 26, 1999, allowing all three parameters to vary (top) and fixing s_d at -4.35 (bottom). Recorded downhole pressures are calculated by adding a constant value of 6822 psi to measured surface pressures.

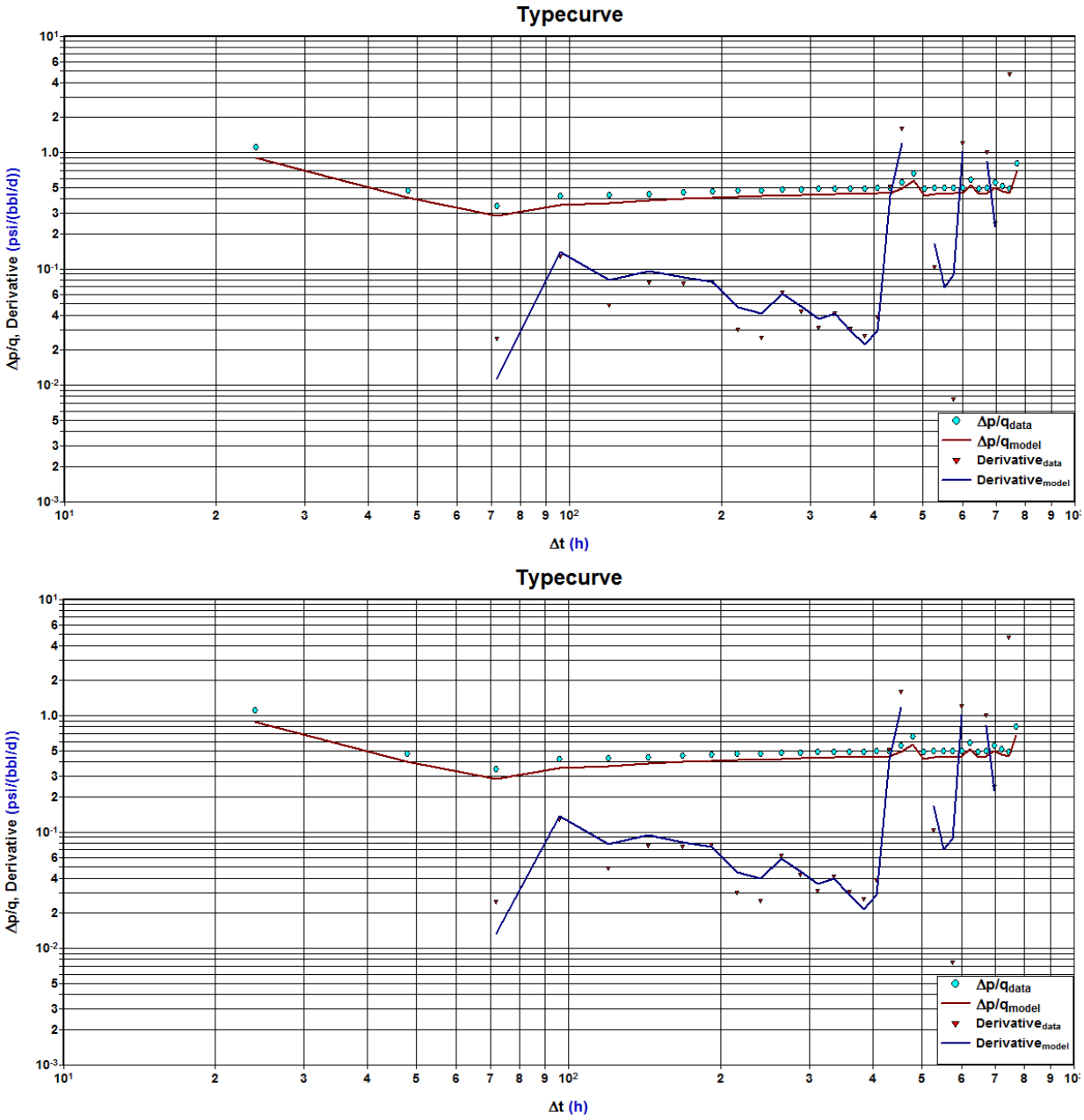

Figure 4-9. Recorded (blue dots) and modeled (red line) values for change in pressure (Δp) divided by flow rate (q), and the recorded (red triangles) and modeled (blue lines) values for the time derivative of Δp/q for an example Phase II cycle, beginning July 26, 1999, allowing all three parameters to vary (top) and fixing s_d at -4.35 (bottom).

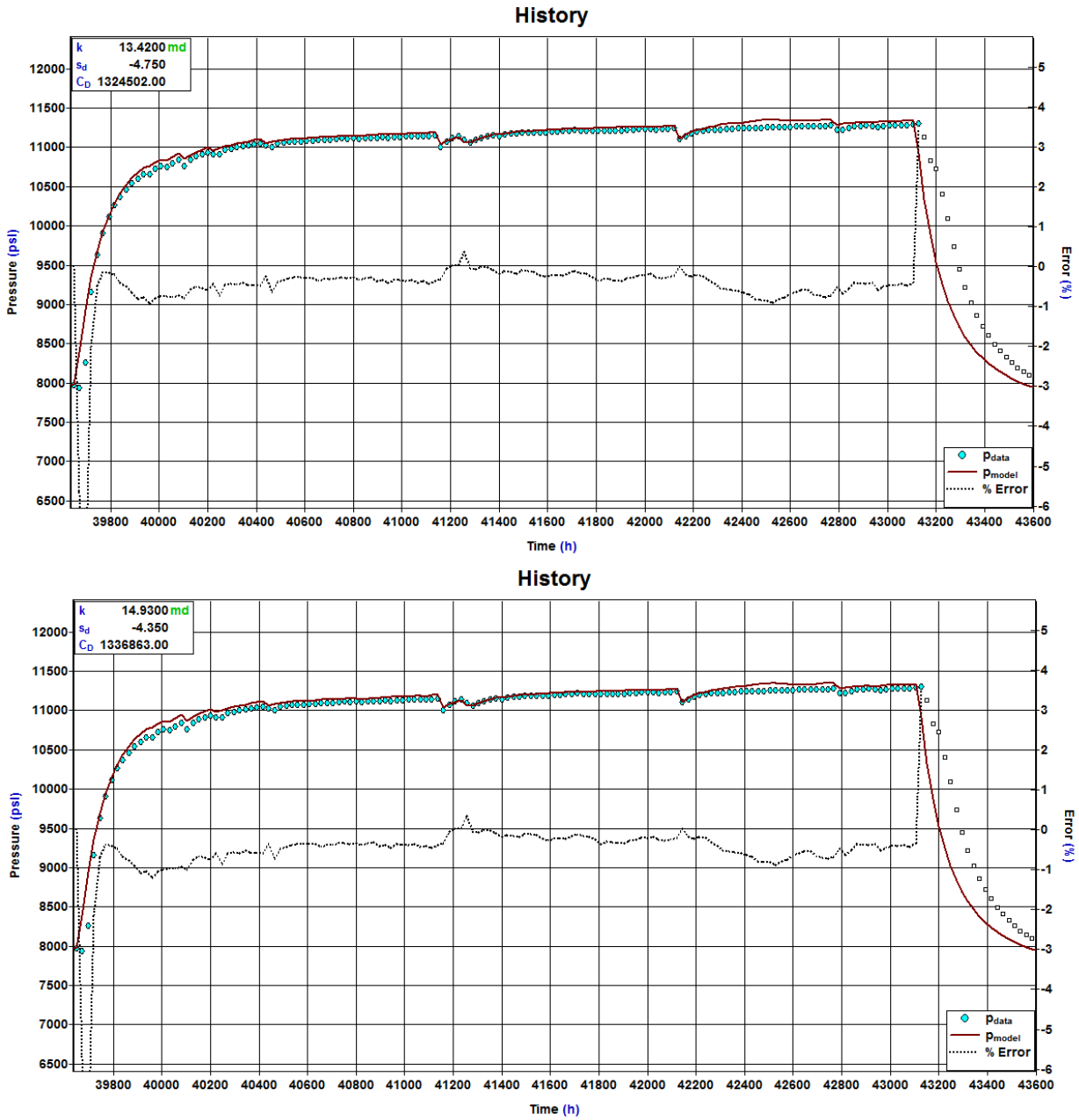

Figure 4-10. Recorded (blue dots) and modeled (red line) downhole pressures and percent error (dashed line) for an example Phase III cycle, beginning January 8, 2001, allowing all three parameters to vary (top) and fixing s_d at -4.35 (bottom). Recorded downhole pressures are calculated by adding a constant value of 6822 psi to measured surface pressures.

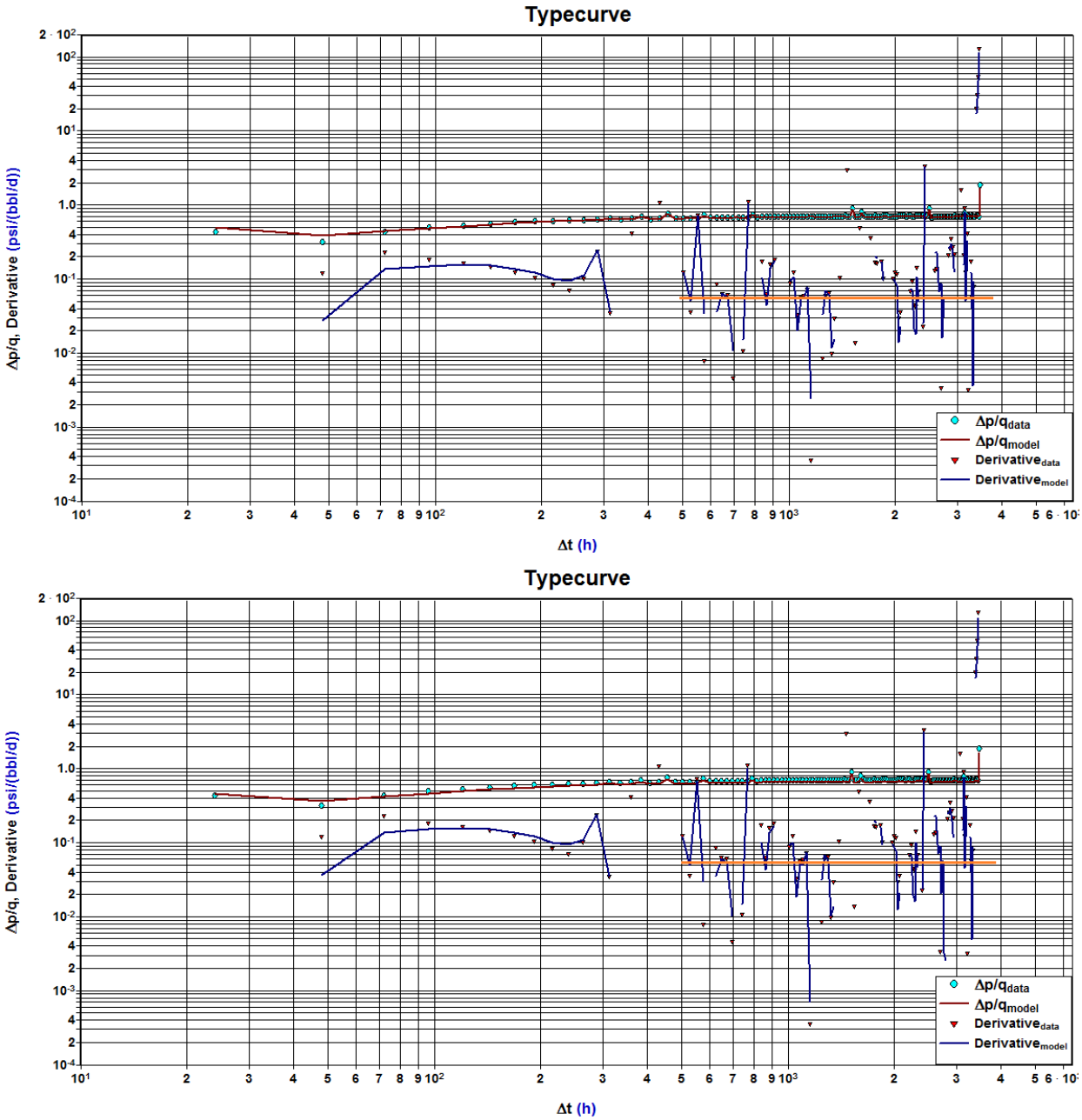

Figure 4-11. Recorded (blue dots) and modeled (red line) values for change in pressure (Δp) divided by flow rate (q), and the recorded (red triangles) and modeled (blue lines) values for the time derivative of Δp/q for an example Phase III cycle, beginning January 8, 2001, allowing all three parameters to vary (top) and fixing s_d at -4.35 (bottom). Orange lines highlight the (approximate) emergence of radial flow.

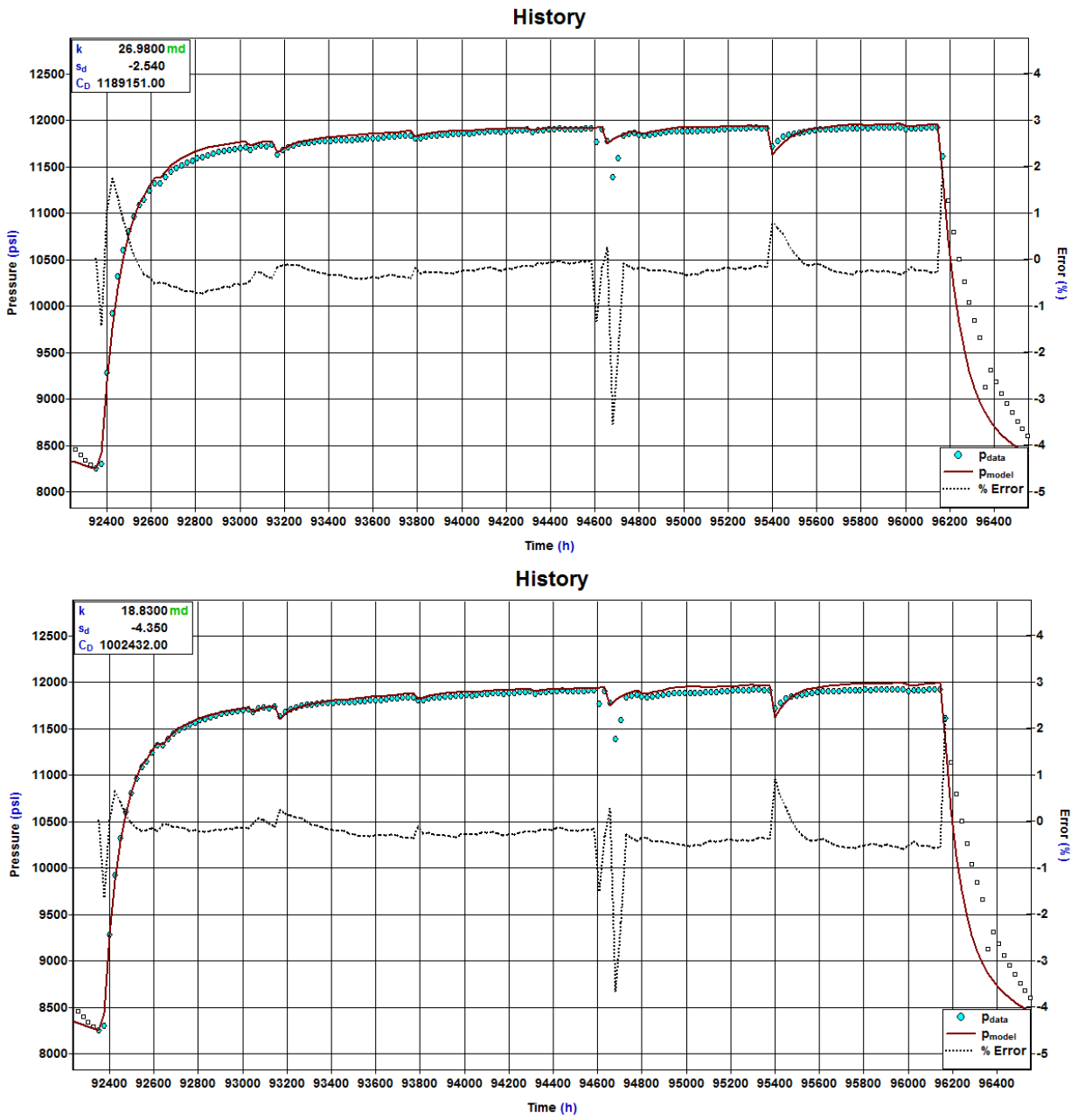

Figure 4-12. Recorded (blue dots) and modeled (red line) downhole pressures and percent error (dashed line) for an example Phase IV cycle, beginning January 14, 2007, allowing all three parameters to vary (top) and fixing s_d at -4.35 (bottom). Recorded downhole pressures are calculated by adding a constant value of 7133 psi to measured surface pressures.

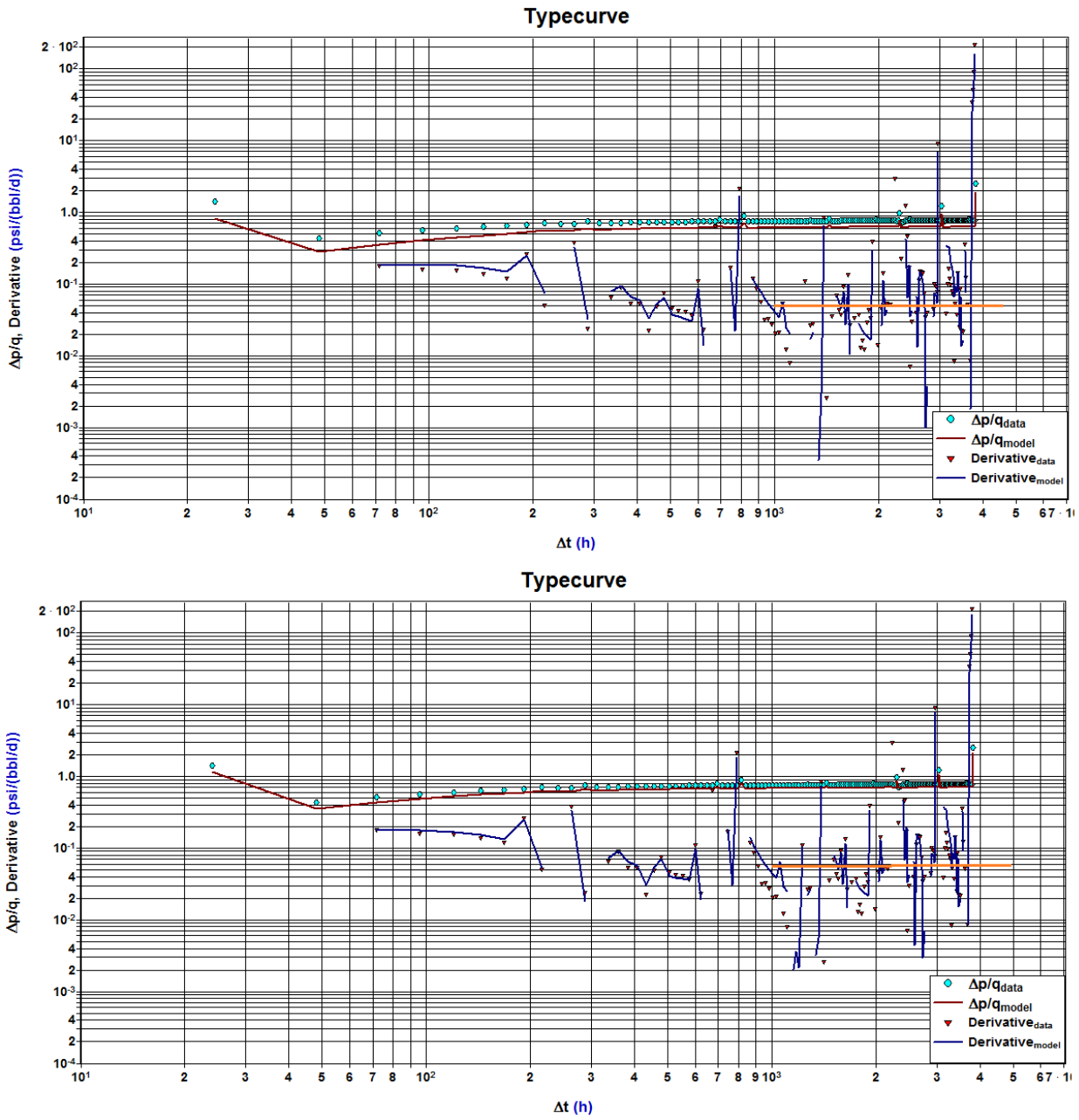

Figure 4-13. Recorded (blue dots) and modeled (red line) values for change in pressure (Δp) divided by flow rate (q), and the recorded (red triangles) and modeled (blue lines) values for the time derivative of Δp/q for an example Phase IV cycle, beginning January 14, 2007, allowing all three parameters to vary (top) and fixing s_d at -4.35 (bottom). Orange lines highlight the (approximate) emergence of radial flow.

The fits in the later phases are generally better than in Phase I, particularly compared to the time prior to 1998 when there were more variations in flow rate. Whether or not s_d is fixed, the models generally fit the data within 2% error for the buildup cycles in Phase II and within 1-2% error in Phases III and IV. Errors tend to be lowest in periods of continuous flow, and highest at the beginning of cycles and around mid-cycle shut-ins.

While the magnitude of the pressure falloff during the shut-ins is matched relatively well, the shapes of the falloff curves are not well-matched in the later phases, with the pressures falling off more slowly than predicted. It is possible to fit the falloff curves with similar values of k and s_d as were obtained from fitting the buildup curves; however, it is necessary to use significantly higher values of C_D, as demonstrated by the example falloff curves shown in Figure 4-14. While this seems counterintuitive in a porous medium model, fracture closure during falloff periods could cause more fluid to be forced into the near-wellbore area, causing pressures to falloff more slowly than modeled.

a.

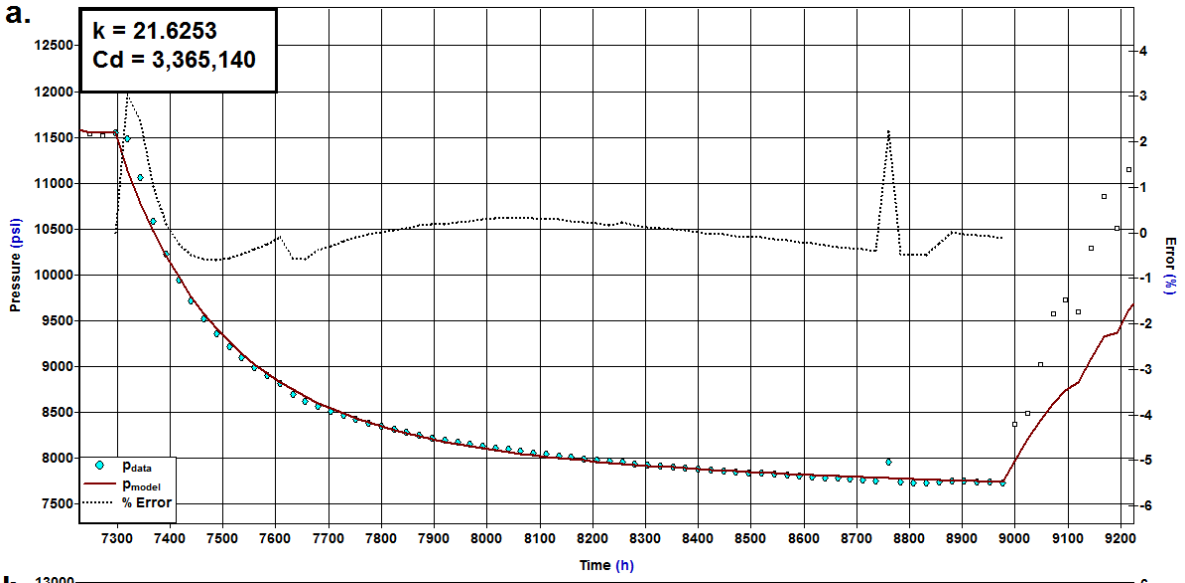
k = 21.6253
Cd = 3,365,140
Pressure (psi)
Error (%)
Time (h)
Pdata
Pmodel
% Error

b.

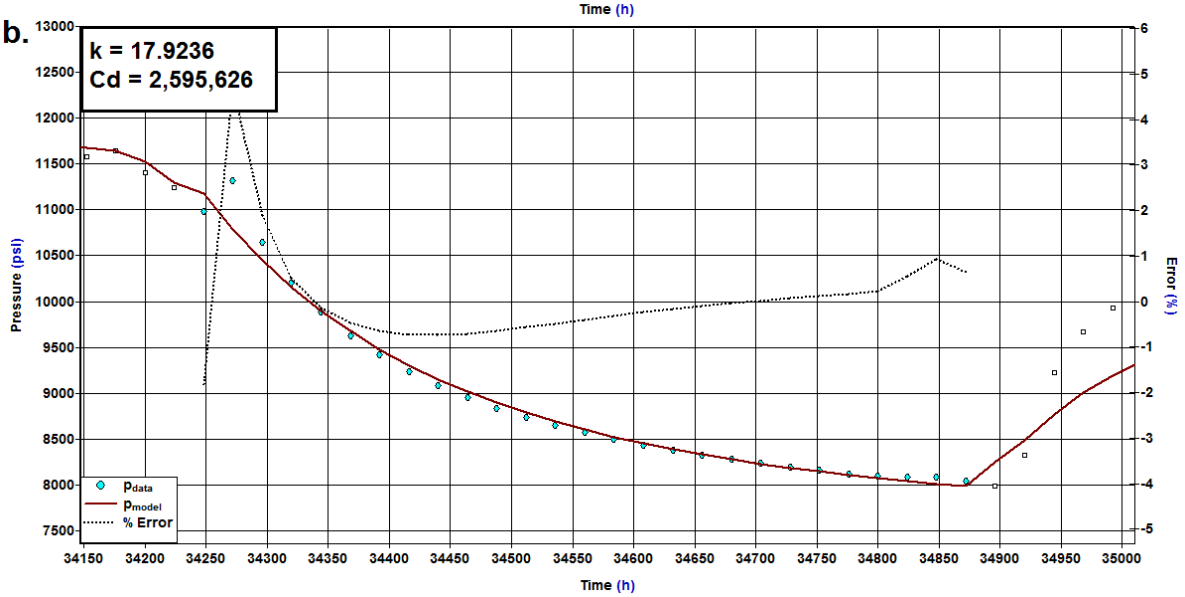
k = 17.9236
Cd = 2,595,626
Pressure (psi)
Error (%)
Time (h)
Pdata
Pmodel
% Error

c.

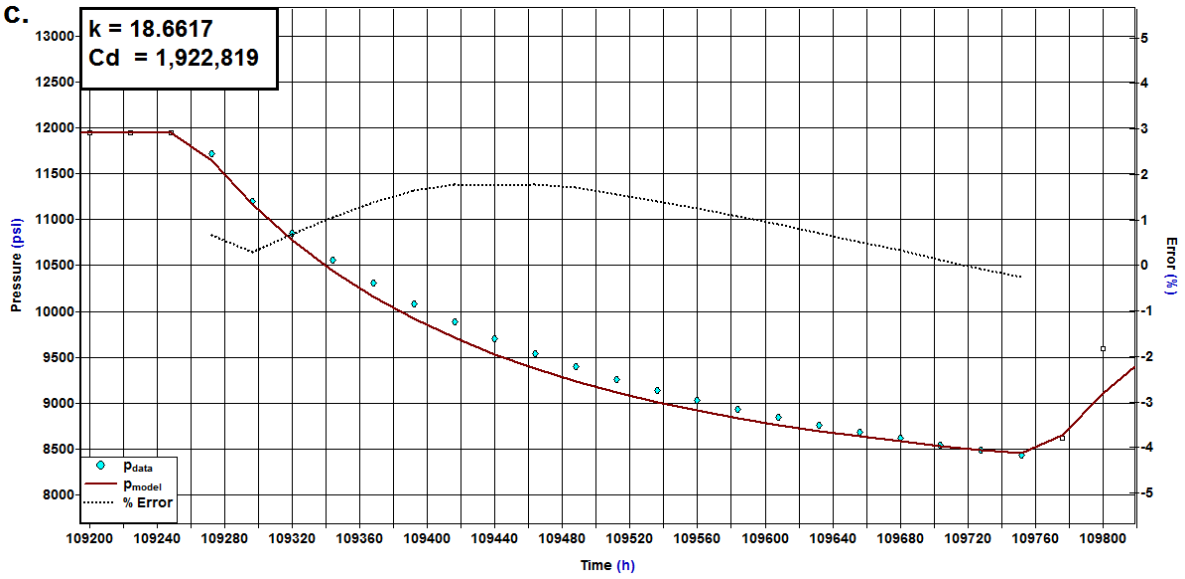
k = 18.6617
Cd = 1,922,819
Pressure (psi)
Error (%)
Time (h)
Pdata
Pmodel
% Error

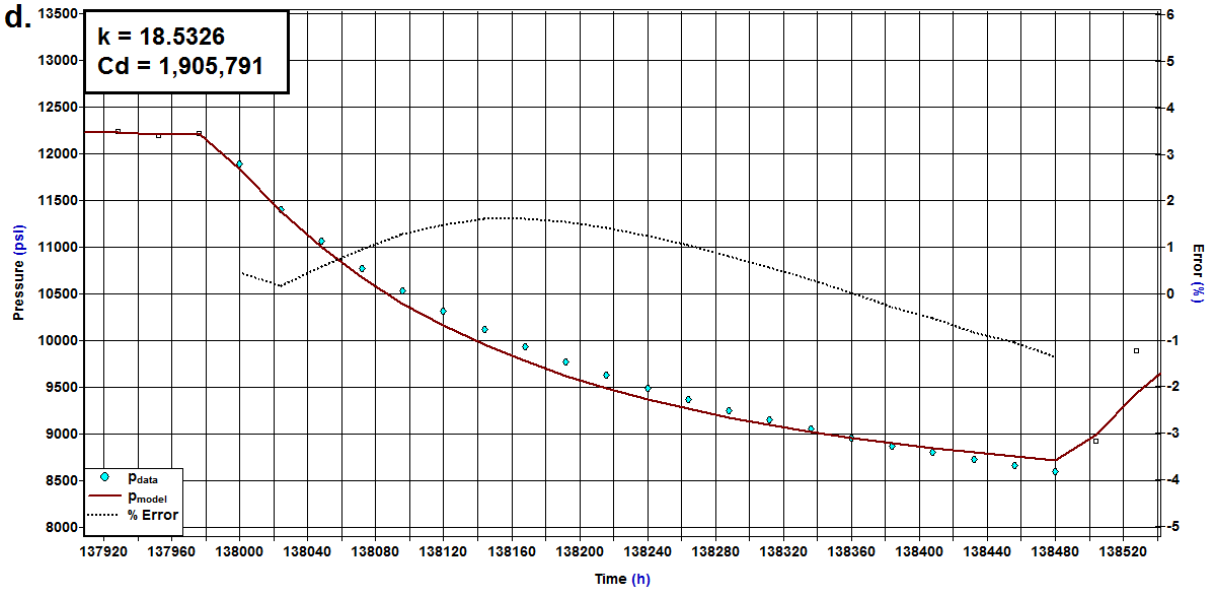

Figure 4-14. Recorded (blue dots) and modeled (red lines) downhole pressures and percent error (dashed linse) during four example falloff periods, beginning (a) May 1, 1997, (b) May 28, 2000, (c) December 18, 2008, and (d) March 29, 2012. Values for k and C_d were fit with s_d fixed at -4.35, and are shown in the top left corner of each plot.

The earlier portions of the type curves shown above appear to indicate primarily the transition from wellbore storage to radial flow, with radial flow (identifiable as a flat spot on the derivative curve) emerging around 1000 hours in Phases III and IV (Figure 4-11, Figure 4-13). The transition is more difficult to identify in Phases I and II due to the number of changes in flow rate. Even in Phases III and IV, the amount of scatter in the derivative, much of which is related to unplanned shut-ins or other changes in flow rate, makes it difficult to resolve the precise times that these transitions occur. Boundary effects, which cause an increase in the derivative following the radial flow period, are not observed. If boundary effects exist, they would be more readily observed during a long flow period having no shut-ins and minimal changes in flow rate (or alternatively, during a long shut-in period).

4.3.3 Using r_{inv} to Investigate Changes in Permeablity

An important concept in well test interpretation is the radius of investigation. The radius of investigation is not a theoretically rigorous concept, but in general has been shown to provide an adequate estimate of the distance that is "sensed" by the well (Fekete, 2012). There are several definitions of the radius of investigation, which differ only by a constant. Here we use the definition from Lee (1982), that the radius of investigation is the point where the pressure variations are fastest, which is equivalent to the location of the pressure front. Using this definition, the radius of investigation can be derived from the solution to the diffusivity equation for an instantaneous line source in an infinite medium:

$$p - p_0 = \frac{c_1}{t} e^{\frac{-r^2}{4Dt}} \qquad (4.11)$$

where p is pressure in psi, p_0 is initial pressure in psi, t is time in hours, r is radius in feet, D is hydraulic diffusivity in square feet per hour, and c_1 is a constant, related to the strength of the instantaneous source.

The hydraulic diffusivity, in arbitrary units, is defined as :

$$D = \frac{k}{\phi \mu c_t} \tag{4.12}$$

where k is permeability, ϕ is fractional porosity, μ is viscosity, and c_t is total compressibility. Converting to oilfield units, this equation becomes:

$$D = 2.64 * 10^{-4} \frac{k}{\phi \mu c_t} \tag{4.13}$$

where k is in mD, μ is in centipoises, and c_t is in psi^{-1}.

Equation (4.11) can be solved for the time, t_m , when the pressure disturbance is a maximum at r_{inv} by differentiating with respect to time and setting equal to 0, yielding:

$$\begin{aligned} \frac{\partial p}{\partial t} &= \frac{-c_1}{t^2} e^{\frac{-r^2}{4D\pi}} + \frac{c_1 r^2}{4Dt^3} e^{\frac{-r^2}{4D\pi}} = 0 \\ t_m &= \frac{r_{inv}{}^2}{4D} \end{aligned} \tag{4.14}$$

Substituting Equation (4.12) into Equation (4.14) yields, in arbitrary units:

$$t_m = \frac{\phi \mu c_t r_{inv}{}^2}{4k} \tag{4.15}$$

In oilfield units,

$$t_m = \frac{948 \phi \mu c_t r_{inv}{}^2}{k} \tag{4.16}$$

Equivalently,

$$r_{inv} = \sqrt{\frac{kt}{948 * \phi \mu c_t}} \tag{4.17}$$

The value r_{inv} is known as the radius of investigation. Note that r_{inv} is independent of flow rate.

Calculating the radius of investigation for a single cycle likely leads to an underestimation, since the pressures are still elevated at the end of a shut-in, which is not accounted for in the calculation of r_{inv} .

There is significant scatter in the recorded $\Delta p/q$ derivatives (Figure 4-7, Figure 4-9, Figure 4-11, Figure 4-13), primarily due to changes in the flow rate, making it difficult to resolve changes in the derivative later in the cycle. However, calculating the radius of investigation at a certain time and observing the derivative at that time can provide a minimum distance from the well to which there are no observable changes in the permeability.

Calculating r_{inv} using typical parameters for a Phase IV cycle results in:

$$r_{inv} = 220\sqrt{t} \qquad (4.18)$$

Using this value, after 35 days (840 hours), the radius of investigation is approximately 2 km. There are five cycles that have no shut-ins exceeding 2 hours duration within the first 35 days. The time derivatives of $\Delta p/q$ versus t for these five cycles are plotted in Figure 4-15, using high sample rate data where available to increase the resolution. While there is still some scatter in the derivatives, there are no trends indicating a change in permeability, providing evidence that the permeability does not change significantly to a distance of at least 2 km from the wellbore (and as discussed above, r_{inv} is likely underestimated).

In contrast to the flow model results, both seismic reflection data and the spatial distribution of seismicity suggest an impermeable fault located about 1.5 km to the northeast of the injection well (King et al., 2014; Block et al., 2012). If the assumption that this fault serves as an impermeable boundary is correct, the inability to resolve this fault indicates that the radial flow model is insensitive to such features in the actual geologic structure at this distance. In particular, if there are preferential flow paths due to pre-existing faults, the pressures recorded at the well may not be equally influenced by the reservoir characteristics in all directions. An alternative explanation for our inability to resolve this fault in the pressure-flow modeling is that the estimated radius of investigation given above is biased by trade-offs between reservoir thickness, permeability, and r_{inv}. For example, if the modeled reservoir thickness of 100 ft were increased by a factor of 4, k would be reduced by a factor of 4, and r_{inv} would be reduced by a factor of 2 to 1.0 km.

a.

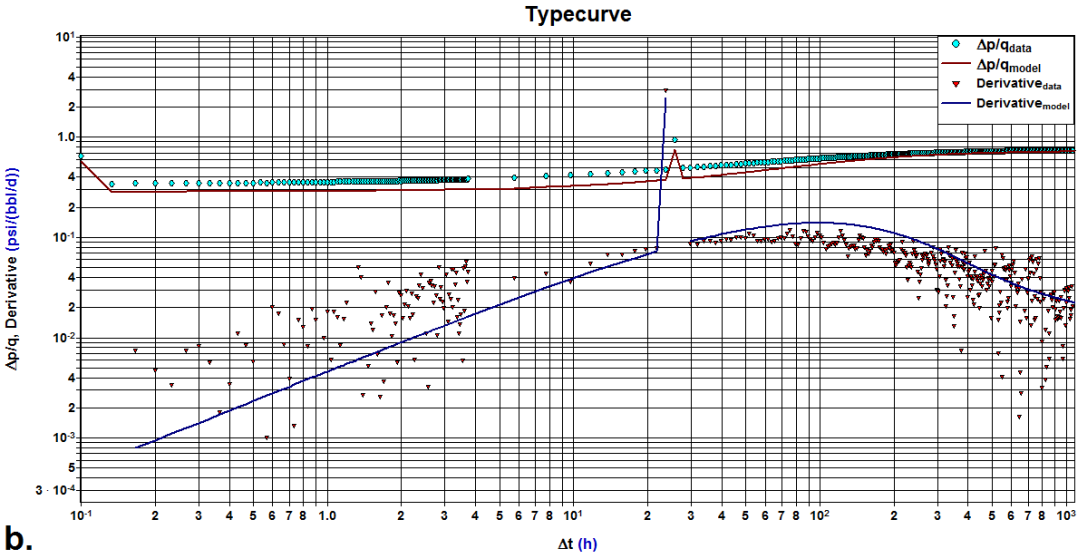
Typecurve
Δp/q, Derivative (psi/(bbl/d))
Δt (h)
Δp/q_data
Δp/q_model
Derivative_data
Derivative_model

b.

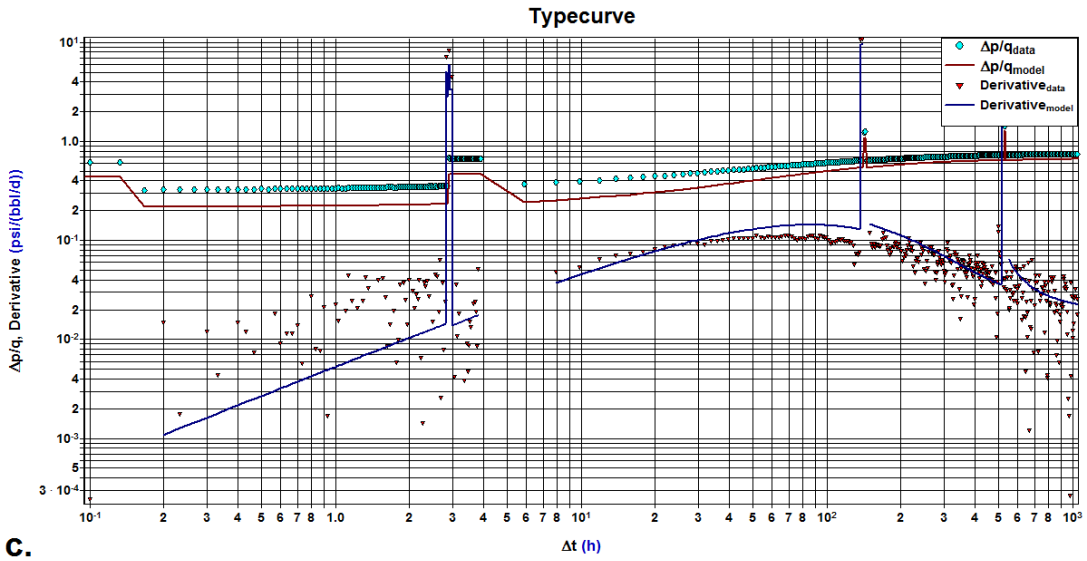
Typecurve
Δp/q, Derivative (psi/(bbl/d))
Δt (h)
Δp/q_data
Δp/q_model
Derivative_data
Derivative_model

c.

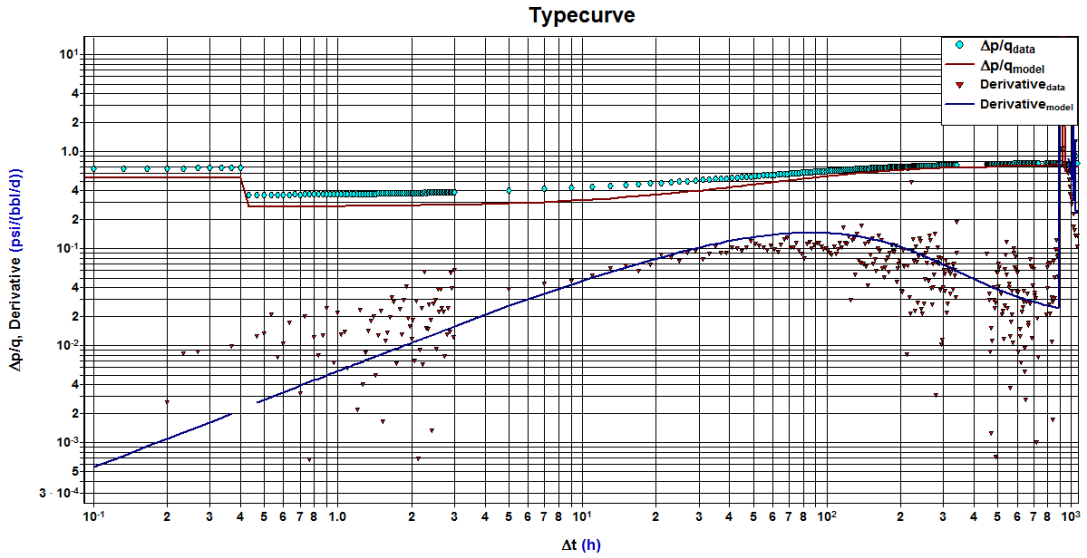
Typecurve
Δp/q, Derivative (psi/(bbl/d))
Δt (h)
Δp/q_data
Δp/q_model
Derivative_data
Derivative_model

d.

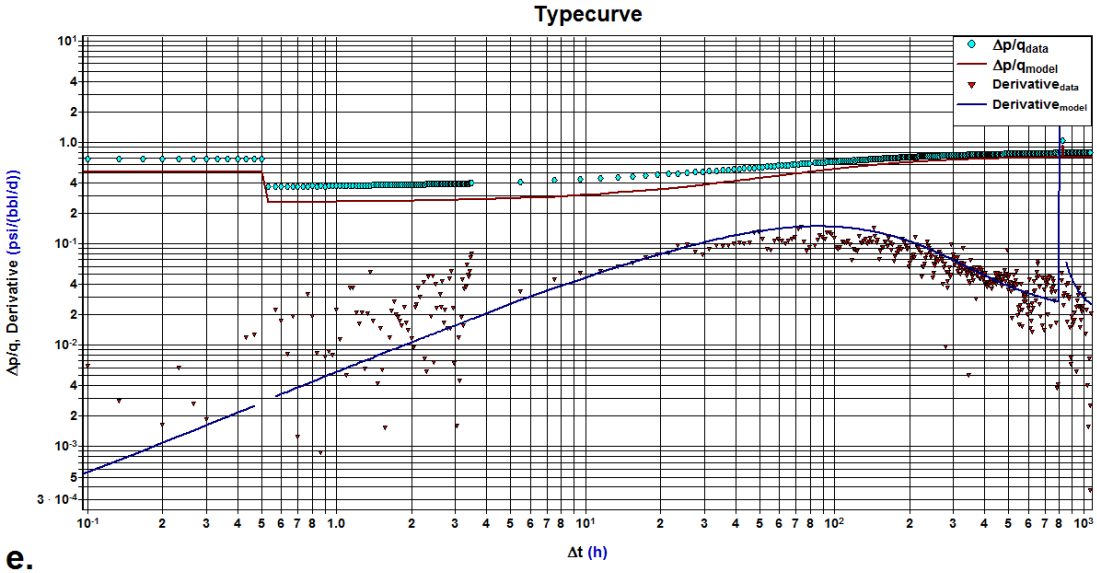

e.

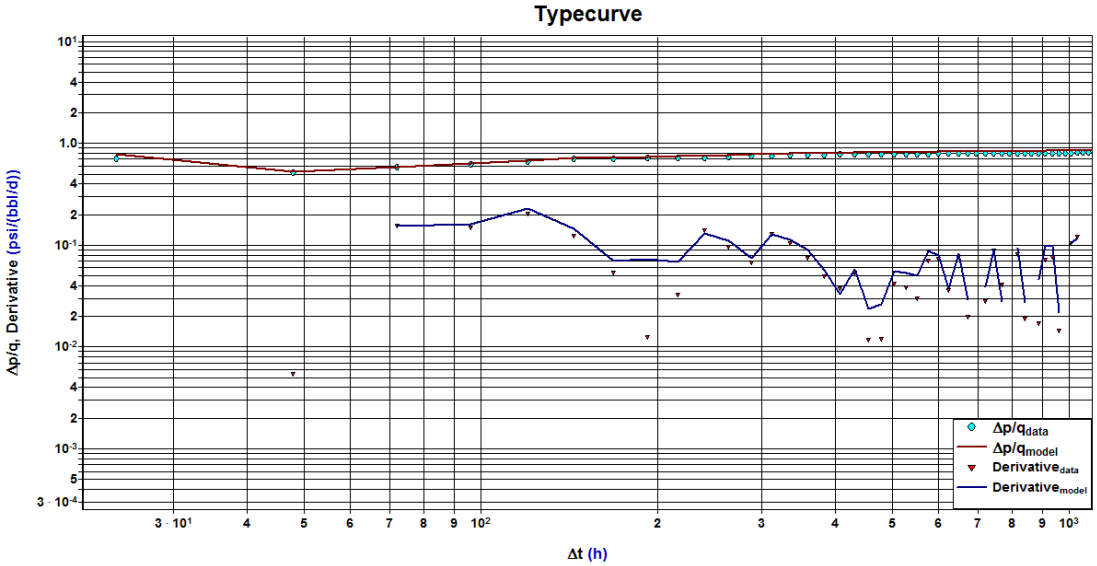

Figure 4-15. Recorded (blue dots) and modeled (red line) values for change in pressure (*Δp*) divided by flow rate (*q*), and the recorded (red triangles) and modeled (blue lines) values for the time derivative of *Δp/q* for the first 35 days (840 hours) for the cycles beginning January 8, 2004 (a), January 6, 2005 (b), January 7, 2009 (c), October 19, 2011 (d), and April 16, 2012 (e). Plots a-d use high sample rate from the SCADA system. Plot e uses daily average data, due to a period of missing data in the SCADA system during that time period.

4.3.4 Fitting Multiple Cycles Simultaneously

The rate of increase in the maximum recorded surface pressure for each cycle appears to be greater since 2010 than previously (Figure 3-1), which suggests the possibility that the pressures are being affected by a reservoir boundary or a zone of decreased permeability. To explore this possibility, a model was constructed that held all parameters fixed for multiple cycles. Figure 4-16 shows actual and modeled pressures for a single set of parameters for the cycles from March 2006 through January 2013. These parameters were derived as by fixing s_d at -4.35, the same value as used in Section 4.3.1, and determining best fit values for k and C_D, inputting small

injection rates during shut-in periods in order to treat these cycles as a single cycle. While there is a general trend of the modeled pressures being higher than the recorded pressures from 2006-2009 and lower than recorded pressures from 2010-2013, the mismatch between the recorded and modeled maximum pressures is relatively small for all cycles, suggesting that a radially symmetric model with infinite-acting boundaries is adequate to model the data during this time period. It is likely that the increase in maximum pressure in recent years is therefore related to a decrease in the number of unscheduled maintenance shut-ins, which has led to a decrease in the total shut-in time per cycle, an increase in the average injection rate, and a commensurate increase in the maximum pressure.

This pressure rise is not unexpected, as pressure-flow modeling theory holds that even in the simplest case of injecting into an infinite reservoir at a constant rate, the derivative of pressure increase will become constant, or equivalently, the pressure will increase at a constant rate. Thus, pressure rise does not by itself necessarily indicate either boundary effects or near-well effects.

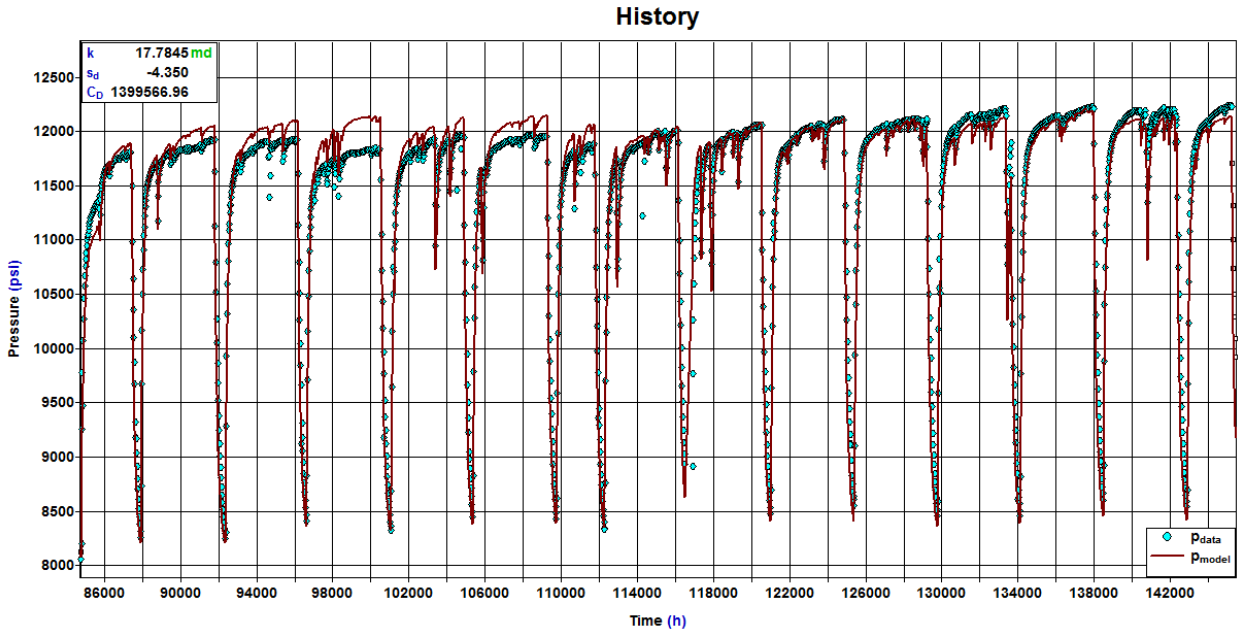

Figure 4-16. Recorded (open squares) and modeled (red lines) downhole pressures for the time period from March 2006 to January 2013. The model uses a single set of input parameters, as shown in the bottom left corner. Recorded downhole pressures are calculated by adding a constant value of 7133 psi to measured surface pressures.

4.4 Pressure-Flow Modeling Discussion

With 18 years of pressure-flow data, Paradox Valley is a unique case study. The time scale for typical well test models ranges from minutes to days, rather than the hundreds of days modeled in this study. Additionally, it is atypical of most waste disposal projects to inject above fracture propagation pressures for long periods of time. Consequently, there are no clear analogs in the published literature for the expected behavior of wellhead pressures at Paradox Valley that may result from various assumed reservoir characteristics. The theoretical behavior for our simple model should be the same over long or short time periods, but the analysis is complicated by the

frequent flow rate changes that have occurred over the long injection history, the likely changes in reservoir properties over time, and the large area experiencing pore pressure increases.

However, the ability of this simple model to fit the data reasonably well despite these complicating factors, both by fitting the cycles individually and by fitting the last several cycles with a single set of injection parameters, provides strong evidence that there have not been significant changes in the reservoir properties near the injection well over the last several years. Near-wellbore scaling should be apparent in the pressure-flow data, possibly through a decrease in the wellbore storage constant or an increase in the skin due to damage, both of which would indicate degradation of the near-wellbore conditions, or through a change in permeability. A decrease in calculated permeabilities over the last several years, which could indicate precipitation over a large area, is not observed.

A radial composite permeability, with a decreased permeability in the near-wellbore region compared to the area further from the well, should be evident as a decrease in the derivative of $\Delta p/q$ (change in pressure divided by flow rate) versus time, as illustrated in the typecurve shown in Figure 4-17.

In summary, while we recognize that a radial flow model is insufficient to fully resolve the complexities of the geologic structure, we do not see any effects in the pressure-flow modeling over the last several years that would appear to indicate near-wellbore changes, and thus conclude that the observed pressure increase is primarily due to far-field reservoir pressurization.

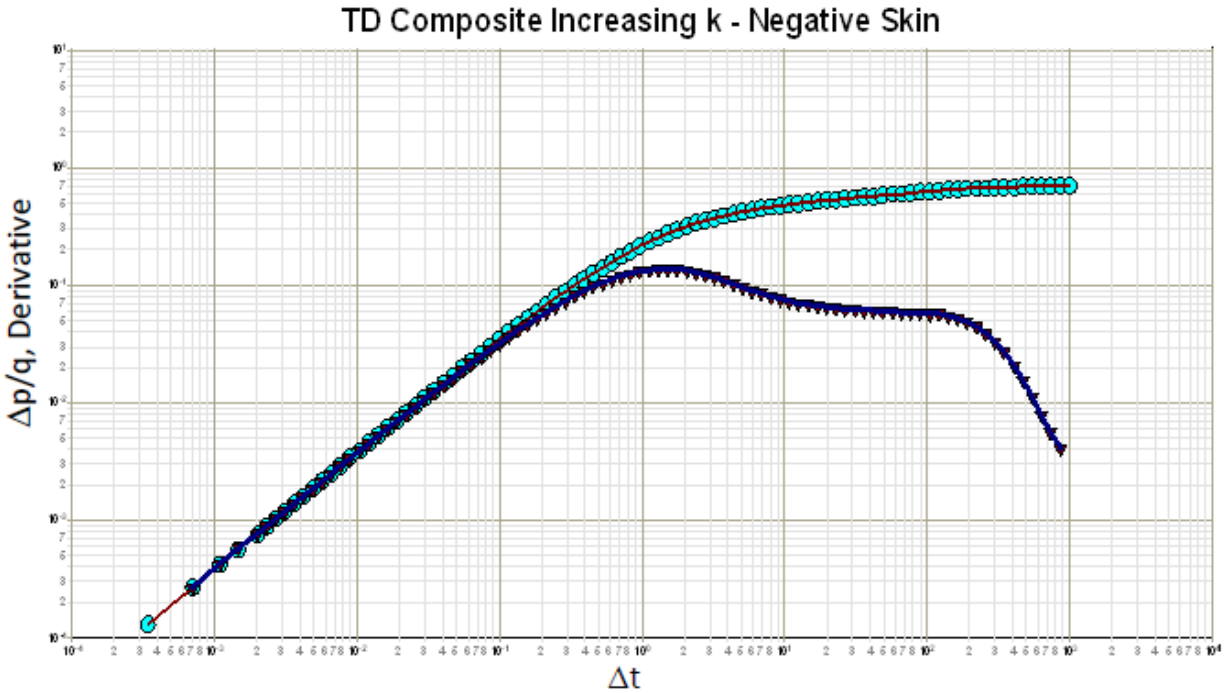

Figure 4-17. Typecurve for change in pressure (Δp) divided by flow rate (q) (circles) and the time derivative of Δp/q (triangles) versus time for a reservoir with negative skin due to damage and radial composite permeability with higher permeability further from the well. From Fekete (2012).

A Consultant Review Board (CRB) was held in January 2015 to discuss the MASIP. This CRB recommended supplementing our analysis using a set of analytical equations. In addition to allowing comparison to and verification of the results obtained using the Fekete software, this method allows for the calculation of pressures away from the well, which may then be compared to the induced seismicity data. This analysis is the subject of future work.

5 Induced Seismicity

5.1 History of Seismicity

Seismic monitoring of the Paradox Valley area began in 1983, with installation of the first stations of the Paradox Valley Seismic Network (PVSN). Network installation was timed to provide a pre-injection baseline of naturally occurring background seismicity. The network has been continuously operated since 1985, and has been expanded and updated over the years to respond to changing seismicity patterns. The current configuration consists of a surface array of 20 digitally recorded, broadband, 3-component sensors.

Six years of pre-injection monitoring recorded no earthquakes within 18 km of PVU Injection Well #1. The data recorded during this period include just one local earthquake, which occurred about 19 km from PVU Injection Well #1. Within days of the start of the initial injection test in 1991, seismic events were detected in the immediate vicinity of the injection well. During subsequent injection tests and continuous injection operations, induced earthquakes occurred at progressively increasing distances from the injection well. The close correlation between injection operations and induced seismicity at PVU has been well established (Ake et al., 2005; Block et al., 2014b).

The geographical distribution of induced seismicity over time is presented in the series of maps shown in Figure 5-1. For reference, four seismicity areas have been delineated and named: (1) Near-well - By the end of the injection tests in 1995, earthquakes were occurring 3 to 4 km from PVU Injection Well #1 (Figure 5-1a). This area of induced seismicity immediately surrounding the injection well is referred to here as the “near-well” region. (2) Northwest (NW) cluster - In mid-1997, about a year after the start of continuous injection, earthquakes began occurring 6 to 8 km northwest of the injection well (Figure 5-1b). This cluster of induced seismicity is called the “northwest (NW) cluster”. (3) Northern valley - In mid-2000, earthquakes were first detected 12 to 14 km from the injection well, along the northern edge of Paradox Valley (Figure 5-1b). Several distinct clusters of earthquakes have occurred along the northern edges of the valley since 2000 (Figure 5-1c). The earthquakes occurring in all of these clusters are referred to as “northern valley events”. (4) Southeast (SE) cluster - An earthquake was first detected about 6 km southeast of the injection well in 2004 (Figure 5-1c), but the seismicity rate in this area markedly increased beginning in 2010 (Figure 5-1d). This group of earthquakes is referred to as the “southeast (SE) cluster”. In recent years, a few isolated earthquakes have been detected in previously aseismic areas, including in the center of Paradox Valley (Figure 5-1d).

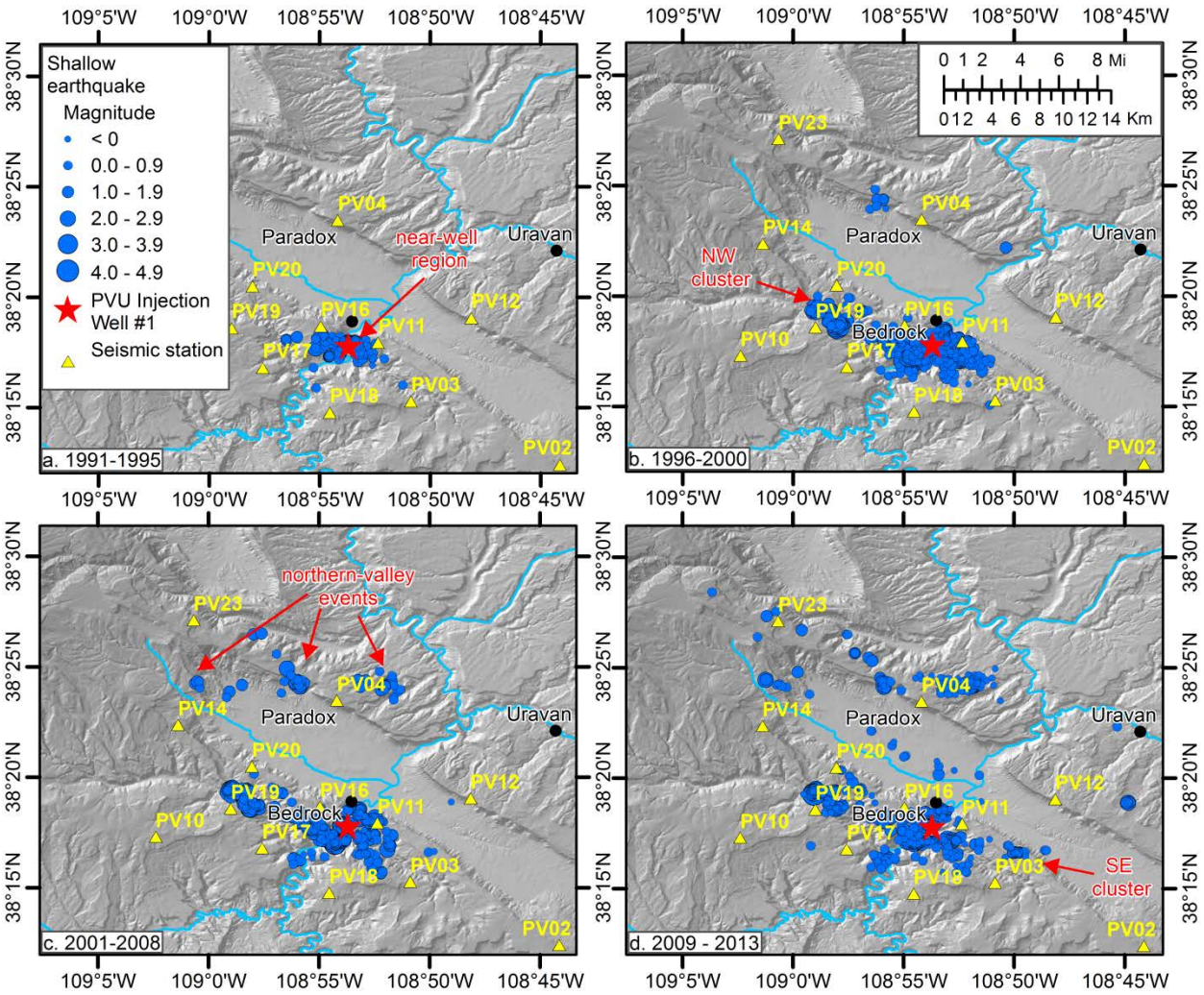

Figure 5-1. Maps showing the spatial distribution of shallow seismicity recorded in the Paradox Valley area over time: (a) injection tests, 1991-1995; (b) continuous injection, 1996-2000; (c) continuous injection, 2001-2008; (d) continuous injection, 2009-2013. All detected earthquakes locating less than 8.5 km deep (relative to the ground surface elevation at the injection wellhead) are included.

5.2 Relation to Pore Pressure Diffusion

The occurrence of seismicity is not necessarily evidence of the presence of injectate, since seismicity may be caused by pore-pressure increase in the in-situ fluid. While it is also possible that seismicity could be induced by changes in the hoop and radial stresses rather than pore pressure changes, pore pressure perturbation is the generally accepted primary mechanism for inducing seismicity from fluid injection (Healy et al., 1968; Raleigh et al., 1972; Hsieh, 1979; Talwani and Acree, 1984). The onset of seismicity triggered on preexisting, critically loaded faults by pore pressure diffusion tends to exhibit distinctive trends in space-time. To evaluate whether pore pressure diffusion appears to be a major triggering mechanism for the PVU-induced seismicity, we examine time-distance plots of the seismicity and compare them to the trends expected for seismicity triggered by pore pressure diffusion.

Linear pore pressure diffusion in a fluid-saturated poroelastic medium is described by the low-frequency limit of the second compressional wave of the Biot equations (Biot, 1962). For the simplified case of uncoupled pore pressure diffusion in an isotropic, homogeneous, poroelastic medium, the diffusion equation reduces to:

$$\frac{\partial p}{\partial t} = D\nabla^2 p \tag{5.1}$$

or, in cylindrical coordinates:

$$\frac{\partial p}{\partial t} = D\left(\frac{\partial^2 p}{\partial r^2} + \frac{1}{r}\frac{\partial p}{\partial r}\right) \tag{5.2}$$

where p is pore pressure, t is time, and D is hydraulic diffusivity. The wave satisfying this equation is dispersive, with higher frequencies traveling faster than lower frequencies (Shapiro et al., 1997). However, the higher frequencies also have significantly lower amplitudes, and these extremely small pore pressure perturbations are not likely to trigger induced seismicity (Rothert, 2004). Rather, it is usually assumed that induced seismicity is triggered when the lower-frequency, higher-amplitude components arrive.

For a point pore pressure perturbation in an infinite homogeneous medium, Shapiro et al. (1997) derived an estimate for the earliest arrival time at a distance r from the source corresponding to the higher-energy, lower-frequency components:

$$t = \frac{r^2}{4\pi D} \tag{5.3}$$

or, equivalently:

$$r = \sqrt{4\pi D t} \tag{5.4}$$

This relation was derived assuming a constant pore pressure perturbation persisting at the source location until time t or later (see Rothert, 2004, for a more detailed description). Similar considerations lead to the radius of investigation of the pressure-flow modeling, Equation (4.17). At a given time t after introduction of a significant pore pressure perturbation, induced seismic events have a greater probability of occurrence at distances < r than at distances > r. This time-distance relation is known as the triggering front of induced seismicity. It has been applied to case studies of seismicity induced by deep well injection into crystalline basement rock (Shapiro et al., 1997; Shapiro et al., 2002; Rothert, 2004; Dinske, 2010).

Other derivations of the triggering front have been developed and applied to the study of induced seismicity. A simple 1-D relation of the form $r = \sqrt{4Dt}$ has been used to analyze seismicity induced beneath reservoirs (Talwani et al., 2007; Durá-Gómez and Talwani, 2010) and within

confined aquifers (Assumpcão et al., 2010). More complex triggering front relations have been derived for anisotropic media (Shapiro et al., 1999; Dinske, 2010), but distance remains proportional to $\sqrt{t}$. For nonlinear pore pressure diffusion, where the hydraulic properties vary with pressure, Hummel and Müller (2009) derived a 1-D analytical relation with $r \propto \sqrt{t}$, while Shapiro and Dinske (2009) derived a relation for the 3-D case with $r \propto t^{1/3}$ for large nonlinearity.

We choose to fit space-time plots of the PVU-induced seismicity data using the simple 1-D triggering front relation, $r = \sqrt{4Dt}$. Based on borehole flow measurements and patterns of induced seismicity, we believe that most of the injected fluid and associated rise in pore pressure are confined primarily to the target injection formations, especially the Leadville formation. Pressure diffusion through these sub-horizontal layers is likely to conform better to a 1-D solution than to a 3-D solution for a spherical geometry. Because both the linear 1-D and 3-D relations are parabolic equations, the fit to the data is the same regardless of the relation used. However, the value of the hydraulic diffusivity derived from the fit differs depending on the relation.

We found 4 injection start times for which the seismicity time-distance plots appear to be relatively unaffected by earlier injection operations and for which there are enough seismic events over a large enough radial distance to define a move-out curve. These injection start times are: the start of injection test #6 on January 18, 1994; the start of injection test #7 on August 1, 1994; the start of long-term injection on July 22, 1996; and the resumption of long-term injection on July 10, 1997, after a 70-day injection well shut-in. For injection tests prior to test #6, there are few recorded seismic events over limited radial distances, and therefore trying to fit a curve to the seismic move-out is not robust. For injection cycles between 1997 and 2000, the injection well shut-ins were not sufficiently long for effects of earlier injection to dissipate. Since 2000, an aseismic zone has persisted around the well to a radial distance exceeding 1 km, and the seismicity beyond that range is not sensitive enough to the injection well shut-ins that have occurred to dissipate sufficiently between cycles. For each of the 4 identified time periods, we visually fit the 1-D pressure diffusion curve to the seismic data in two ways: using the start time of injection as the reference time, and using a time shortly before the onset of seismicity as the reference time. To reduce scatter due to event location uncertainty, we include events with duration magnitude 0.5 and larger, since these events tend to have better-constrained locations. The fits are shown in Figure 5-2.

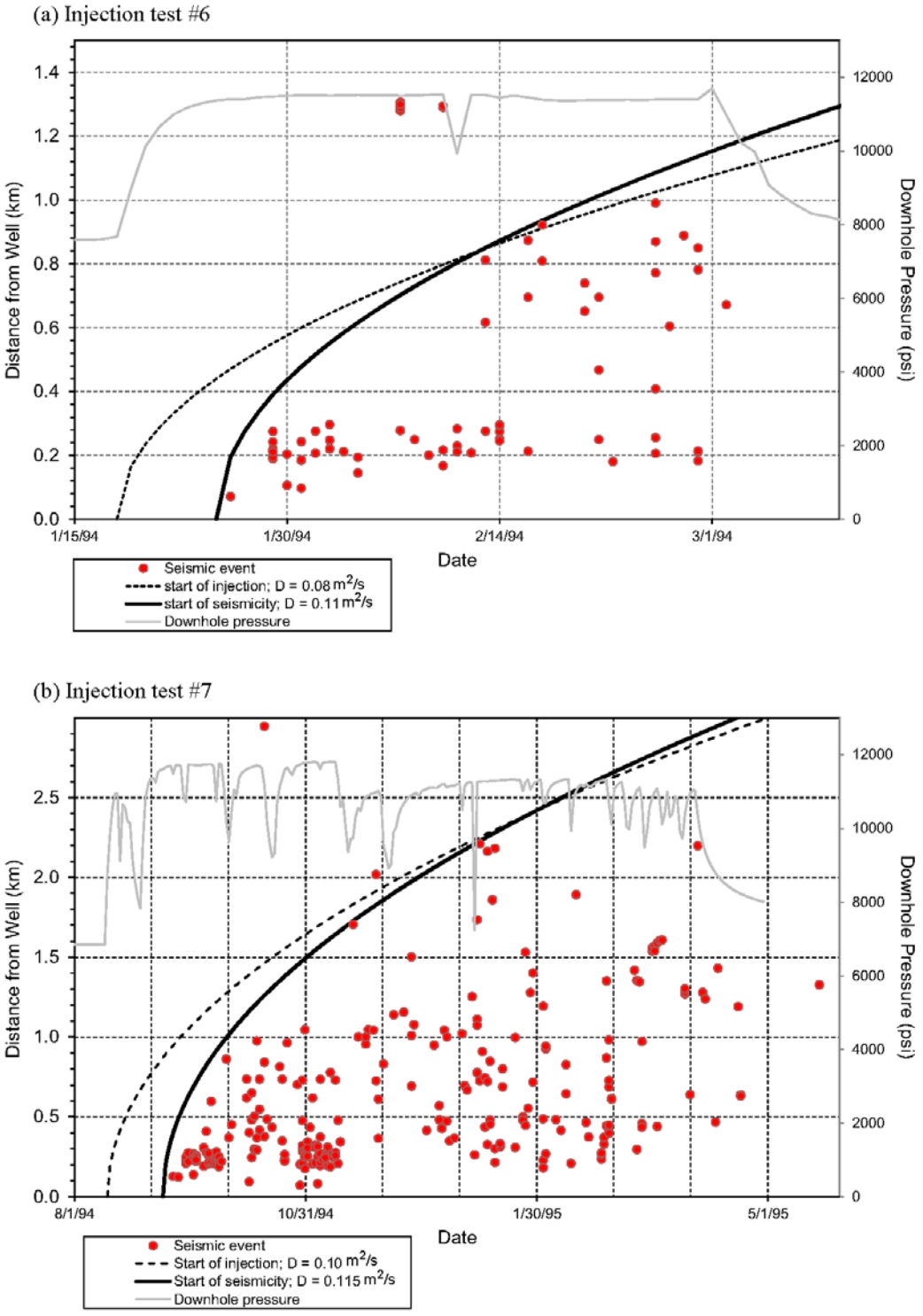

Figure 5-2. Seismicity time-distance plots for 4 injection start times: (a) start of injection test #6 (Jan. 1994), (b) start of injection test #7 (Aug. 1994), (c) start of long-term injection (Jul. 1996), and (d) resumption of long-term injection after 70-day shut-in (Jul. 1997). Two seismic triggering fronts are fit to each cycle, using a 1-D pressure diffusion relation and two different reference times. The downhole pressure is included for reference.

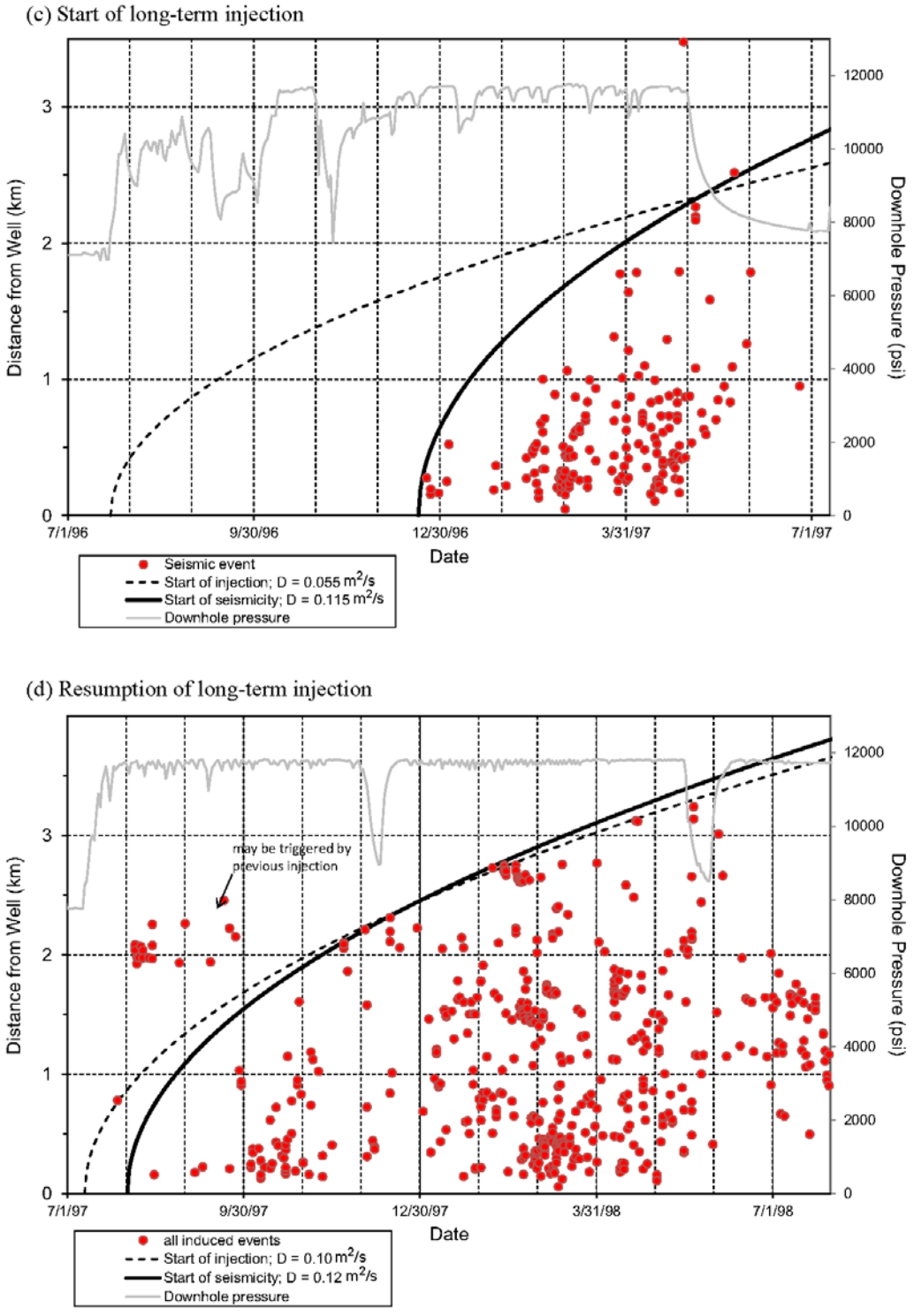

Figure 5-2, continued.

Application of seismic triggering front relations to seismic time-distance plots assumes that the time between the elevation of pore pressure at the source point and the occurrence of seismicity at a given distance from the source is due solely to the pressure diffusion time lag. These relations do not take into account any time lag that may occur between the start of injection and the increase in pore pressure to a sufficiently high level to trigger seismicity. For the 4 injection cycles shown in Figure 5-2, seismicity begins near the well shortly after the downhole pressures reach a plateau. For 3 of the 4 time periods, the difference between the start of injection and the subsequent pressure plateau and start of seismicity is small. The corresponding difference in the two pressure diffusion fits is also fairly small, although the fits using a reference time corresponding to the pressure plateau and start of seismicity generally conform better to the seismic move-outs (Figure 5-2a, b, and d). Diffusivity values obtained for these 3 cycles using the injection start time as a reference range from 0.08 to 0.10 m^2/s; values obtained using the later reference times range from 0.11 to 0.12 m^2/s. In contrast to these 3 cycles, for the start of long-term injection, there is a 5-month delay between the beginning of fluid injection and the time when pressures consistently remain high and seismicity begins (Figure 5-2c). This long delay is partially due to 2 multi-day injection well shut-ins that occurred during the intervening months; a time delay required to re-pressurize a previously-stimulated reservoir is also likely. Using the start of injection for the pressure diffusion reference time provides a poor fit to the data and an anomalously low value of diffusivity, 0.055 m^2/s (Figure 5-2c). Using a reference start time shortly before seismicity begins results in a much better fit to the seismic move-out and a diffusivity value of 0.115 m^2/s, consistent with the values obtained from the other cycles. The fact that the seismicity that began 5 months after the start of injection occurred very close to the injection well (r_{min} = ~160 m) provides further evidence that the large seismic lag time is not related to pressure diffusion, and therefore using a later reference time is reasonable.

To evaluate the radial distance to which a simple 1-D pore pressure diffusion model can explain the onset of seismicity induced by PVU injection, we overlay seismic triggering fronts on a time-distance plot showing all shallow events recorded since the start of injection. Events with depths less than 8.5 km and magnitudes ≥ duration magnitude M_D 0.5 are included. We compute the seismic triggering front for several significant start times of PVU fluid injection: the start of the first injection test (July, 1991); the start of the first injection test after acid stimulation (October, 1993), the start of the first injection test where surface injection pressures exceeded 4500 psi (January, 1994), and the start of long-term injection (July, 1996). For these calculations, we use the average diffusivity value obtained from the previous analysis for the later reference times, 0.115 m^2/s. The time-distance plot is shown with the 4 triggering front curves in Figure 5-3a.

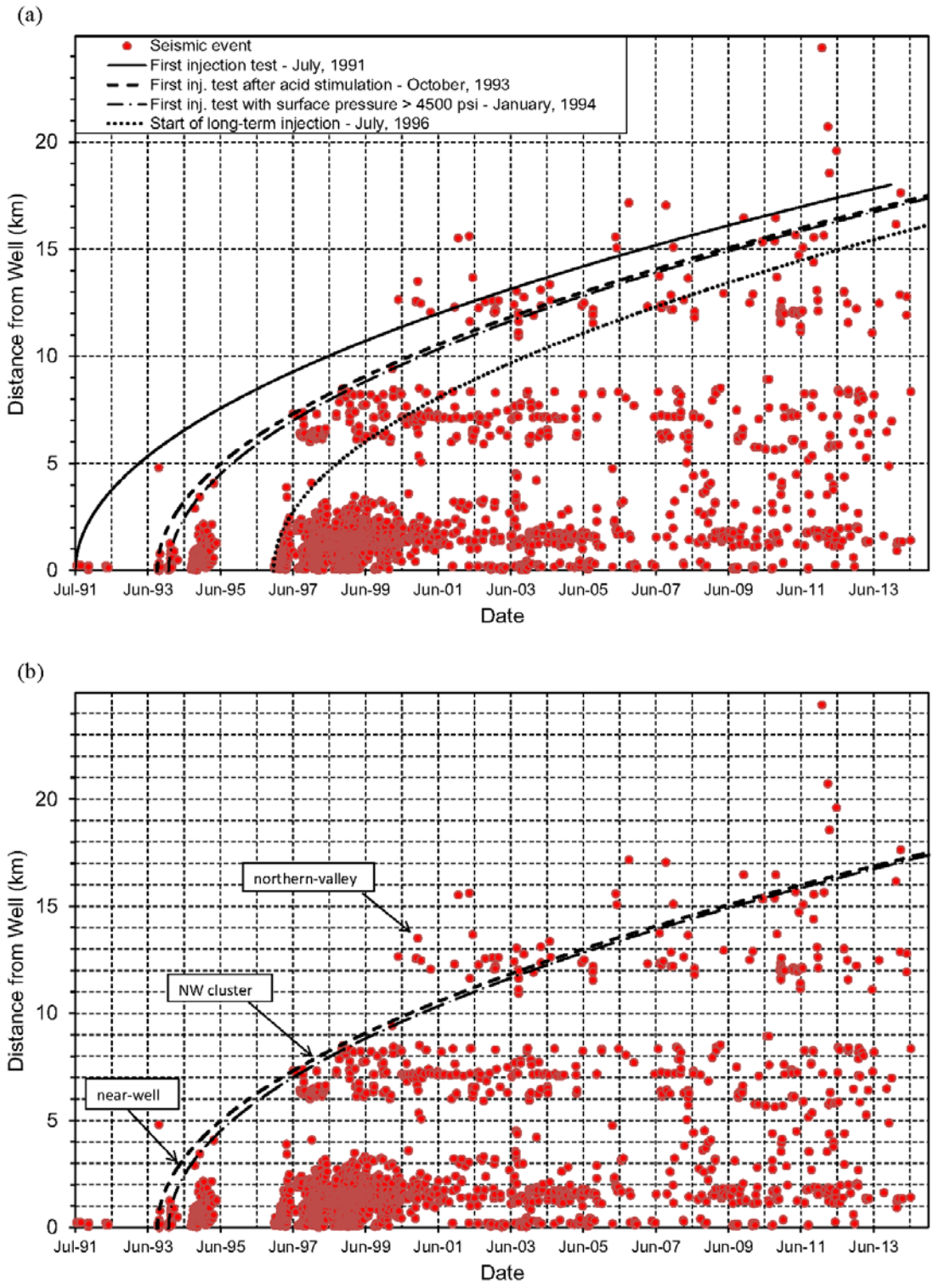

Figure 5-3. Seismicity time-distance plots of all shallow (depth < 8.5 km) events with magnitude ≥ 0.5 occurring in the vicinity of the PVU injection well. (a) Four seismic triggering fronts overlaid – see text for description of their reference times (b) Seismic triggering fronts for the first two significant injection tests overlaid. All triggering fronts were computed using a 1-D linear pressure diffusion model and a hydraulic diffusivity of 0.115 m^2/s.

While none of the triggering fronts match the onset of induced seismicity occurring at all distances, the triggering fronts for the first significant injection tests – those in late 1993 after acid stimulation and early 1994 with pressures above 4500 psi – match the onset of seismicity to radial distances of ~10 km very well. The seismic data are shown with just these two fronts overlaid in Figure 5-3b. The events at distances of 6 to 9 km are in the NW cluster. Previous investigators had suggested that the onset of seismicity in the NW cluster was either related to pressure rise along high-permeability fault zones between the well and the NW cluster (Ake et al., 2005) or stress changes related to the injected fluid (Roeloffs and Denlinger, 2009). These inferences were made based on the onset of NW-cluster induced seismicity only 1 year after the start of long-term injection; the effects of the injection tests apparently were not considered. The analysis presented here indicates that the onset of the NW-cluster seismicity in 1997 could be due to pore pressure perturbations introduced in late 1993 and early 1994 during the first significant injection tests, and that a high-permeability pathway is not needed to explain the observed seismicity patterns.

Shallow seismicity that we interpret as being induced by PVU injection operations at radial distances greater than 10 km began earlier than is predicted with the simple 1-D linear pressure diffusion model presented here. Although these events occur ahead of the computed seismic triggering front, their move-out parallels the front and therefore suggests that their triggering is related to a diffusive process (Figure 5-3b). Possible explanations for the early onset of seismicity at these distances include heterogeneity of hydraulic diffusivity, shear slip on critically-loaded faults from the higher-frequency, earlier-arriving components of pore pressure diffusion, or variations in the rate of pore-pressure diffusion due to variations in stress and strain conditions (Wang, 2000).

According to Shapiro (1999), the value of D obtained from analysis of seismic triggering fronts reflects the value for the rock prior to stimulation and potential subsequent temporal variations in its hydraulic properties. However, numerical modeling performed by Bruel (2007) demonstrates that the value of D obtained with this method may be substantially underestimated if the preexisting faults are not sufficiently close to failure. Hence, the fairly low value of hydraulic diffusivity obtained from the PVU seismic data (0.11 – 0.12 m^2/s) could indicate either that the rock permeability was low prior to stimulation or that the stress states on the faults within several km of the well were not sufficiently close to critical conditions to fail as soon as the low-frequency diffusion front arrived. If we assume that the faults within 10 km of the injection well were not sufficiently critically loaded to fail as soon as the low-frequency pore pressure diffusion front arrived, we can estimate a value of D by fitting the move-out of the distant seismicity (Figure 5-4). In this case, we obtain a value for D of 0.20 m^2/s.

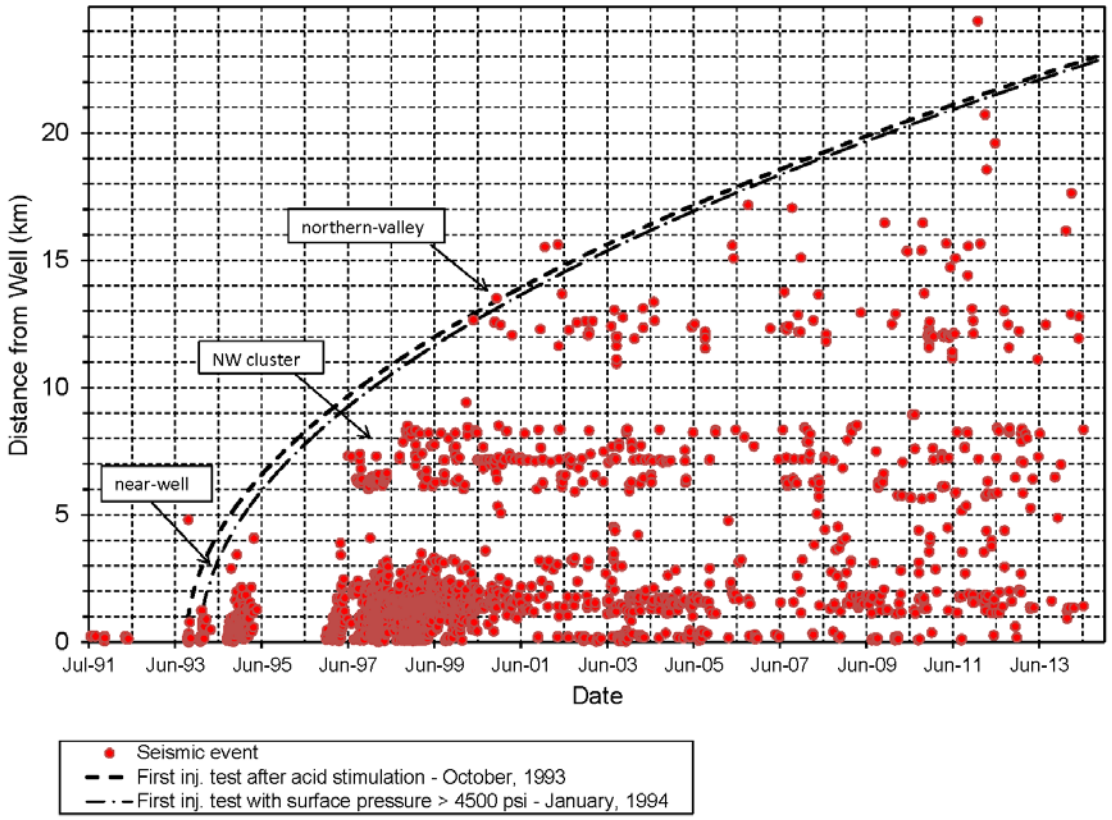

Figure 5-4. Seismicity time-distance plots of all shallow (depth < 8.5 km) events with magnitude ≥ 0.5 occurring in the vicinity of the PVU injection well. Seismic triggering fronts for the first two significant injection tests are overlaid. The triggering fronts were computed using a 1-D linear pressure diffusion model and a hydraulic diffusivity of 0.20 m^2/s.

The estimates of the hydraulic diffusivity computed from this analysis, ~ 0.1 – 0.2 m^2/s, are similar to values derived at sites where injection occurs into low-permeability crystalline basement rock. For example, a hydraulic diffusivity of 0.5 m^2/s was obtained at the Continental Deep Drilling (KTB) site in Germany (Shapiro et al., 1997), 0.17 m^2/s at the Fenton Hill Hot Dry Rock site in New Mexico (Shapiro et al., 2002), and 0.05 m^2/s at Soultz-sous-Forets in France (Shapiro et al., 2002). To evaluate whether the diffusivity values obtained from analysis of the PVU induced seismicity data are reasonable for this site, we calculate the corresponding values of permeability from the diffusivity estimates. We then compare these results with permeability values obtained independently for PVU injection formations by early flow tests in the PVU wellbore.

In hydrogeology (Freeze and Cherry, 1979), the hydraulic diffusivity D is defined as:

$$D = \frac{K}{S_S} \qquad (5.5)$$

where K is the hydraulic conductivity and S_S is the specific storage. Hydraulic conductivity K is related to the material permeability k by $K = k\rho g / \mu$, where ρ is the fluid density, μ is the fluid viscosity, and g is the gravitational constant. Specific storage S_S is given by $\rho g(c + \phi c_f)$, where ϕ is the porosity, c is the (drained) compressibility of the porous medium, and c_f is the compressibility of the pore fluid. Substituting these values into Equation (5.5) and solving for permeability gives:

$$k = D\mu\left(c + \phi c_f\right) \tag{5.6}$$

Comparison to equations for linear poroelasticity given by Wang (2000) indicates that the above equation is valid for the condition of constant stress and the assumptions of incompressible grains and pores. The more general formulas relating diffusivity and permeability for the condition of constant stress are:

$$D_\sigma = \frac{k}{\mu S_\sigma} \tag{5.7}$$

$$S_\sigma = \left(c - c_s'\right) + \phi\left(c_f - c_\phi\right) \tag{5.8}$$

where c_s' is the unjacketed material compressibility (corresponding to the solid-grain compressibility if all the grains are of the same mineral), c_ϕ is the unjacketed pore compressibility, and S_σ is the unconstrained specific storage coefficient. Setting c_s' and c_ϕ to zero, substituting the resulting expression for S_σ into Equation (5.7), and solving for k yields Equation (5.6).

Corresponding equations for the condition of constant strain are (Wang, 2000):

$$D_\in = \frac{k}{\mu S_\in} \tag{5.9}$$

$$S_\in = c_s'\left(1 - \frac{c_s'}{c}\right) + \phi\left(c_f - c_\phi\right) \tag{5.10}$$

with $S_\in$ being the constrained specific storage coefficient. Assuming incompressible grains and pores, Equation (5.10) simplifies to $S_\in = \phi c_f$ and the relation between diffusivity and permeability becomes:

$$k = D\mu\phi c_f \tag{5.11}$$

At depth, c approaches c_s', and therefore the unconstrained storage coefficient S_σ in Equation (5.8) also approaches ϕc_f (assuming incompressible pores: $c_\phi = 0$). Hence, in rigid materials at

depth, the unconstrained and constrained storage coefficients approach the same limit. This approximation and the corresponding equation relating permeability and diffusivity (Equation (5.11)) are often used in petroleum engineering (Wang, 2000) and rock mechanics (Jaeger et al, 2007).

We compute permeability values using both Equations (5.6) and (5.11). For these calculations, we use the fluid viscosity (0.00103 Pa-s) and compressibility (2.8036×10^{-10} Pa) determined previously from the temperature and salinity of the 70%:30% brine-to-fresh water mix. We perform the calculations using diffusivity values of 0.1 and 0.2 m^2/s, to span the range of values determined from the analysis of the seismic data. For porosity, we assume values ranging from 3% to 8%, based on the PVU well log data (see Table A-1, Appendix A). For the drained material compressibility in Equation (5.6), we first compute the undrained bulk modulus of the Leadville formation using a P-wave velocity of 6350 m/s, S-wave velocity of 3387 m/s, and density of 2750 kg/m^3 determined from PVU well log data. We subsequently compute the corresponding drained bulk modulus using Gassmann's equation for fluid substitution (Russell and Smith, 2007) and a limestone grain bulk modulus of $6.7x10^{10}$ Pa, and then take the inverse to get compressibility. However, for the values of porosity examined here, the difference between the drained and undrained moduli is negligible.

The permeability results are shown as a function of porosity in Figure 5-5. Results using equation (5.6) are represented by the red symbols. These permeability values range from 2.4 to 3.9 mD for a hydraulic diffusivity of 0.1 m^2/s and range from 4.8 to 7.7 mD for a diffusivity of 0.2 m^2/s. The permeabilities computed with Equation (5.11) (blue symbols) range from 0.9 to 2.3 mD for D = 0.1 m^2/s and range from 1.8 to 4.7 mD for D = 0.2 m^2/s. These permeabilities are very consistent with the values determined from early flow tests in the PVU wellbore, which vary from about 1 to 8 mD (see section 4.1). Hence, not only does the move-out of the induced seismicity match the parabolic trend predicted by pore pressure diffusion, the rate of the move-out is also consistent with reservoir properties measured independently by wellbore flow tests.

Since the occurrence of induced seismicity appears to be consistent with a simple diffusion model of pore pressure perturbations introduced at the injection well, it is reasonable to use spatiotemproal seismicity patterns to qualitatively evaluate the evolution of subsurface reservoir pressures and hydraulic connectivity. In the following sections, we examine spatiotemporal patterns of the induced seismicity to evaluate the hydraulic connectivity in the near-well area and whether it appears to have changed over time, to evaluate the region where reservoir properties have likely been altered by injection, and to determine whether the large-scale spatiotemporal seismicity patterns are consistent with increasing far-field reservoir pressurization in recent years.

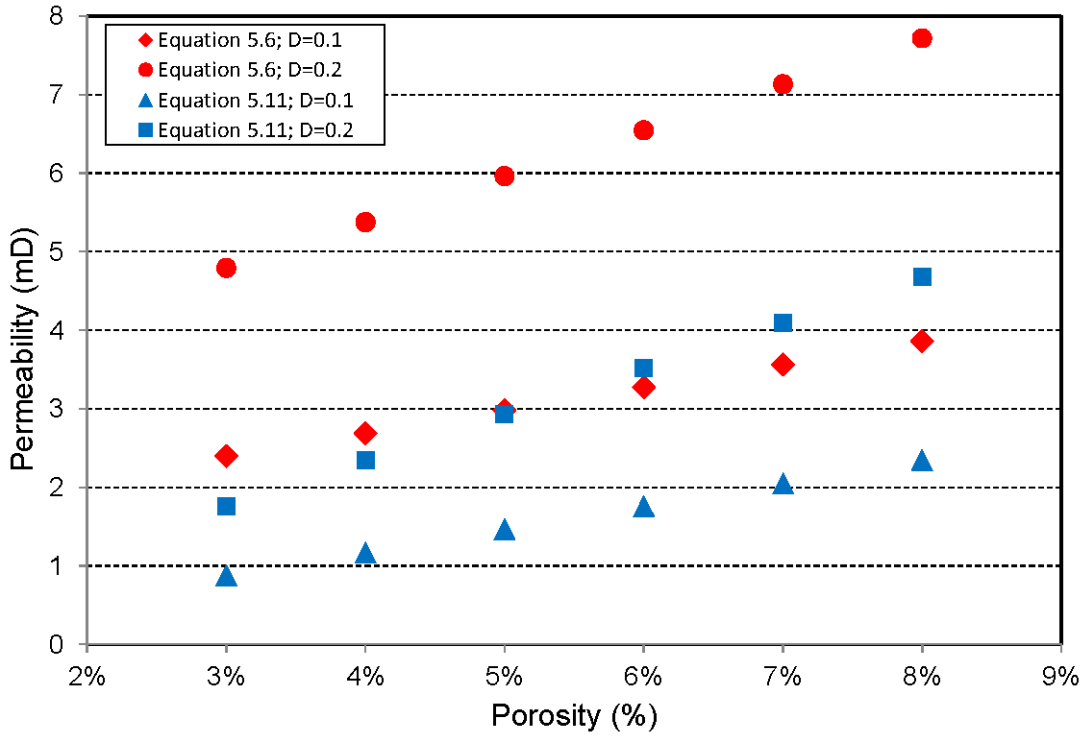

Figure 5-5. Permeabilities computed from seismic-derived values of the hydraulic diffusivity, *D*. Permeabilities were computed for a range of porosities, two values of *D*, and using two different permeability-diffusivity relations.

5.3 Near-Well Seismicity

Below we examine the 3-D spatial patterns of seismicity induced near the injection well to evaluate the hydraulic connectivity in the vicinity of the well. In addition, we look for any changes in the seismicity patterns over time that may provide evidence of temporal variations of hydraulic connectivity or permeability, such as an increase in permeability due to injection or a potential decrease in connectivity over time due to near-wellbore precipitation and clogging of fractures.

5.3.1 Vertical Seismicity Distribution and Hydraulic Connectivity

Increasing depth of fill in the bottom of the injection borehole has covered all but the uppermost perforations and may have led to decreased fluid flow into the deeper sections of the target reservoirs over time. Logging of PVU Injection Well #1 performed in 2001 indicated that the top-of-fill within the borehole was at a depth of 14,172 feet (4320 meters), at the base of the upper Leadville perforations (Subsurface Technology, 2001). In contrast, a previous survey conducted in 1994 indicated that the top-of-fill was at 14,604 feet (4451 meters), near the base of the underlying Elbert Formation. The fill has not been removed from the well, nor has the well been re-entered since 2001. The increased amount of fill within the borehole suggests that the perforations in the lower Leadville and underlying formations may have been accepting

significantly reduced amounts of fluid since at least 2001, as compared to earlier years. This has led to questions over whether injected fluid is confined to the upper Leadville Formation away from the well, or whether it is able to migrate vertically into other permeable zones. If the injection depth interval has been effectively decreased by the presence of the fill, and if there is little vertical migration of the fluid in the surrounding formations, the near-well seismicity should become progressively shallower over time as the injection interval is reduced and the fluid below the injection interval has time to disperse. Here we examine the vertical distribution of seismicity within several km of the injection well and evaluate whether this distribution has changed over time.

Induced seismicity within 3 km of PVU Injection Well #1 occurs over an elevation range of more than 2 km, as illustrated by the map and cross sections in Figure 5-6. The hypocenters shown in Figure 5-6 were computed by an event relative location method and have estimated relative horizontal errors ≤ 50 m and relative vertical errors ≤ 100 m. Most of the seismicity within a few hundred meters of the well occurs at elevations corresponding to the Leadville and other subsalt Paleozoic formations at the well (light and dark blue hypocenters, Figure 5-6). However, at distances greater than 1–1.5 km from the well, most earthquakes occur within significantly shallower (orange, red, black, and gray hypocenters) or deeper (purple hypocenters) seismicity clusters. The large vertical distribution of near-well seismicity suggests substantial vertical hydraulic connectivity in this region. We have used the spatial distribution of the induced seismicity to infer the locations and offsets of northwest trending normal faults, assuming that the seismicity is primarily occurring within or near the target injection formations (Figure 5-6). The vertical distribution of seismicity suggests that these normal faults or other high-permeability zones allow vertical fluid flow and pore pressure propagation. Because there appears to be substantial hydraulic connectivity over a vertical extent exceeding 2 km in the near-well area, the ability to access permeable zones within the target injection formations is unlikely to be substantially degraded by potential decreased fluid flow across the deep perforated zones in the injection well.

The vertical hydraulic connectivity within 3 km of the injection well does not appear to have changed over time, as interpreted from spatiotemporal patterns of induced seismicity. While the spatial occurrence of seismicity varies over time, the depth range of seismicity at any particular location remains relatively constant over time, as shown by the time sequence maps in Figure 5-7. An aseismic zone surrounding the injection well between radial distances of approximately 500 and 1100 m developed after a decrease in the injection flow rate in mid-2000. As discussed further in the next section, we interpret the scarcity of induced seismicity in this region as indicating a change in reservoir characteristics and pore pressure gradients rather than an absence of fluid flow, as suggested by the continued occurrence of seismicity at distances greater than 1100 m from the well over a large range of elevations (Figure 5-7**Error! Reference source not found.**). Additionally, a box plot of earthquakes within 500 m of the injection well shows no consistent variation with time (Figure 5-8). These observations suggest that if any precipitation and clogging of fractures is occurring near the injection well, it is not severe or widespread enough to noticeably interfere with fluid flow and pore pressure propagation.

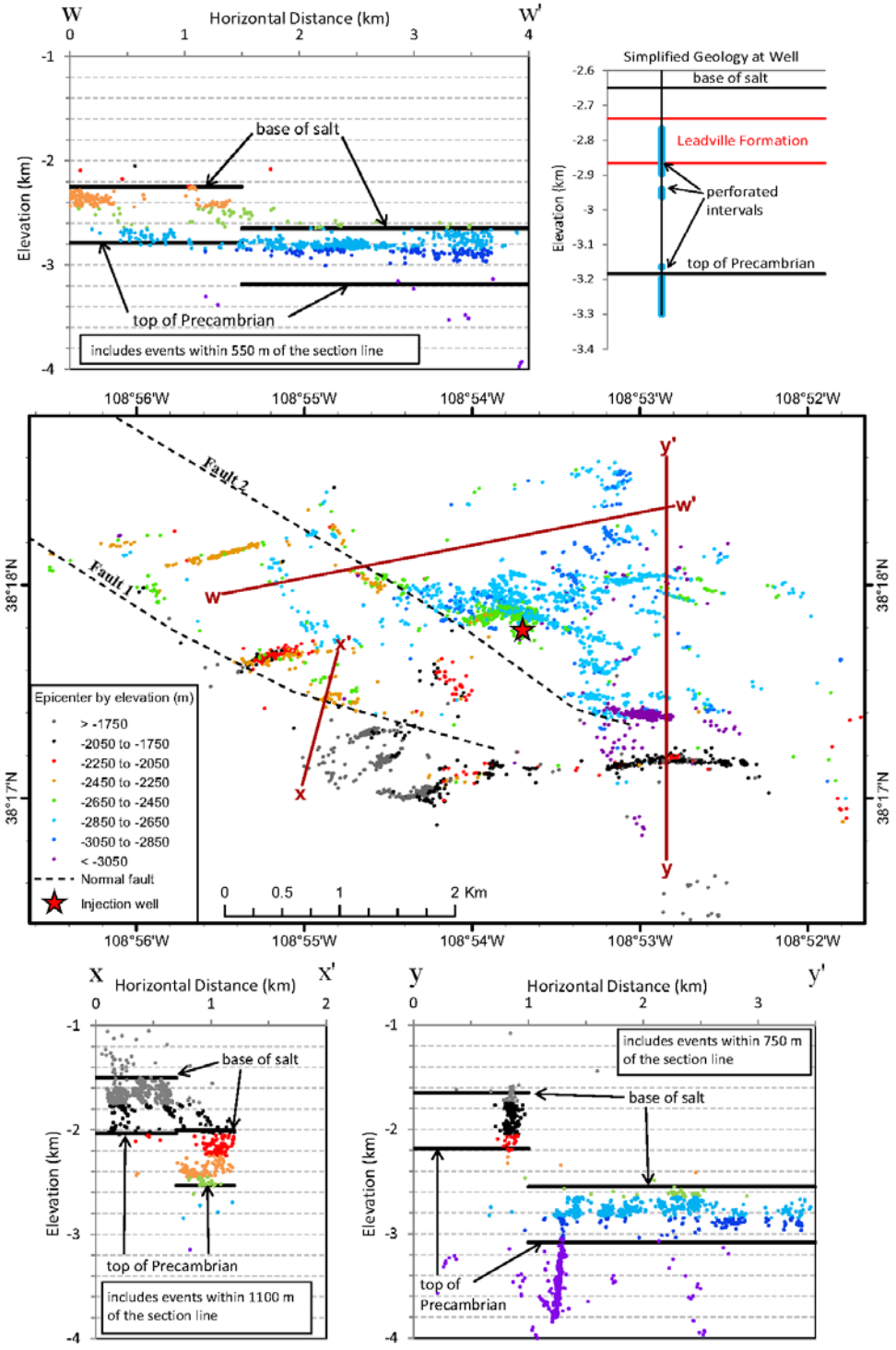

Figure 5-6. Map showing epicenters of earthquakes occurring in the near-well region of induced seismicity, color-coded by hypocenter elevation (center), and cross sections showing distinct vertical offsets of hypocenters (top and bottom). Only a-quality hypocenters from the event relative location are included. Two northwest-striking normal faults interpreted from the hypocenter elevation patterns are shown. Our interpreted base of the Paradox salt and top of the Precambrian (solid black lines) are shown in each cross section. A simplified geologic section at the PVU wellbore is included at upper right for reference.

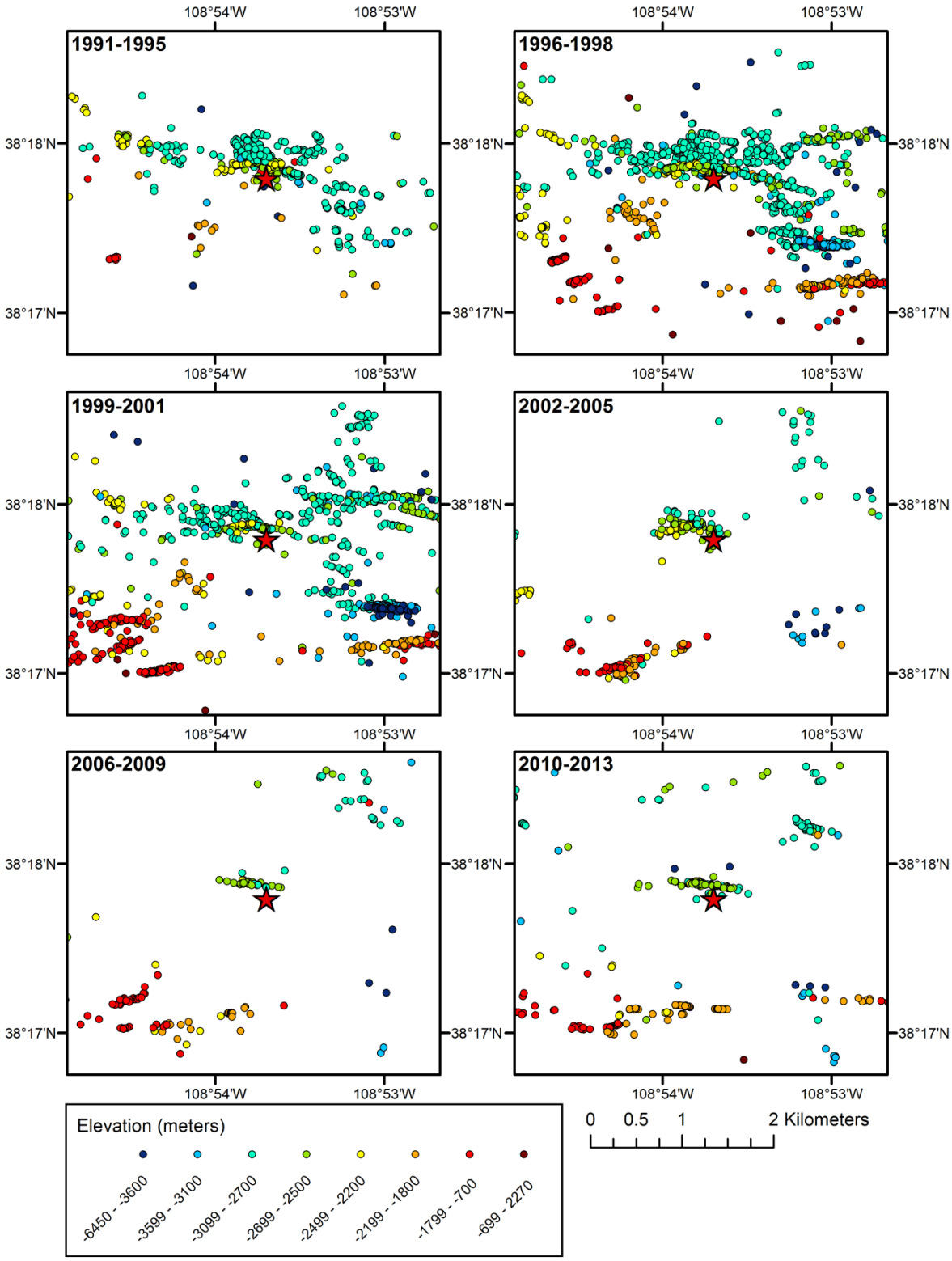

Figure 5-7. Near-well events by year, colored by elevation. Red stars designate PVU Injection Well #1.

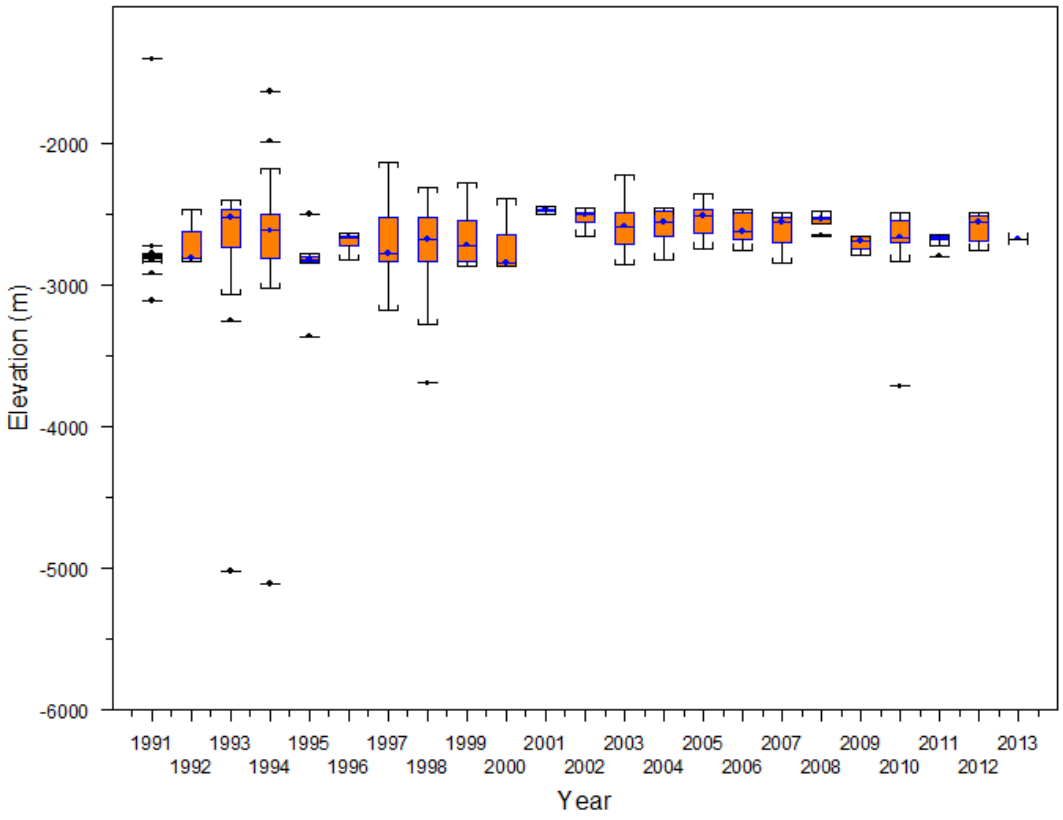

Figure 5-8. Box plot of elevations of earthquakes within 500 meters of the injection well by year, with boxes defined by hinges. Blue dots and lines show the location of the median. Whiskers are drawn to the farthest point within 1.5 times the range between the upper and lower hinges. Black dots and lines designate outliers.

5.3.2 Seismicity Patterns and Reservoir Permeability

The aseismic zone that developed around the injection well after the decrease in flow rate in mid-2000 (Figure 5-7) suggests that pore pressure gradients changed as a result of the injection tests and early years of long-term injection, to a radial distance of at least 1100 m. Temporal variations in pore pressure gradients indicate that reservoir characteristics, such as permeability, have changed. Reservoir permeability can be enhanced during injection by shear slip on pre-existing fractures, opening of new fractures, and cooling and shrinking of the rock matrix. Increased permeability leads to lower spatial gradients of pore pressure, which in turn can cause areas of previous seismic activity to become aseismic (Baisch et al., 2009). In addition, changes in the extent to which permeability is dependent on pore pressure (degree of nonlinearity) can substantially alter pore pressure gradients (Hummel and Muller, 2009). Nonlinearity may change over time; for example, if the rock matrix cools sufficiently to hold fractures open, permeability nonlinearity should decrease.

As the reservoir re-pressurized following the mid-2000 decrease in flow rate, the altered spatial pore pressure gradients within the previously stimulated region appear to have prevented the local pore pressures from increasing sufficiently to exceed values experienced prior to 2000, between distances of about 500 and 1100 m from the well. In contrast, as injection pressures increased (and exceeded pre-2000 values), the areas within 500 m of the well and farther than ~1100 m from the well appear to have experienced greater pore pressures than prior to 2000. Therefore, seismicity has continued in these regions. Without altered reservoir characteristics and corresponding changes in pore pressure gradients in the region surrounding the injection well, seismicity should have resumed in all areas, since downhole injection pressures have exceeded pre-2000 values for many years. This concept of seismic activity occurring only where previously experienced pore pressures are exceeded, known as the Kaiser effect, has been used to explain spatiotemporal induced seismic patterns, and in particular, the development of aseismic zones, at several other injection sites (Baisch et al., 2002; Baisch et al., 2009; Baisch et al., 2010).

The locations of the larger-magnitude (≥ **M** 3.0, or **M** 3.0+) induced earthquakes are consistent with a stimulated zone around the well extending to radial distances greater than ~1.5 km. In computer models of injection-induced seismicity, the larger-magnitude events occur around the edge of the previously stimulated region (Baisch et al., 2010). At PVU, the **M** 3.0+ events are mostly concentrated in a narrow band around the southern and western edges of the near-well region, at radial distances between 1.6 and 2.2 km (Figure 5-9). Of the 12 induced events in this magnitude range, only 2 occurred at distances greater than 2.5 km from the injection well. Both of these more distant *M* 3.0+ events occurred in the NW cluster; the second and largest of these occurred relatively recently, in January, 2013. Maximum earthquake magnitudes are lower in the other seismicity clusters (Figure 5-9). Hence, the patterns of the larger-magnitude PVU events are consistent with a stimulated region around the injection well (where permeabilities likely increased prior to mid-2000) to distances of roughly 1.5 to 2 km. This is approximately equal to the estimated radius of investigation of the pressure-flow modeling, and therefore the modeling should be sensitive to changes in permeability over time within this stimulated area. Permeabilities computed from the pressure-flow modeling with skin factor fixed show a modest increase in permeability between 1996 and 1999 (Table 4-1). The NW cluster may represent a second zone of reservoir stimulation; however, the pressure-flow modeling is not sensitive to reservoir characteristics at this distance from the well.

If precipitation near the injection well has been substantially decreasing reservoir permeability in recent years, we would expect pore pressures near the well to increase, which may lead to increased seismicity rates. An increase in rates of earthquakes occurring close to the well in recent years is not seen. Rather, near-well seismicity rates are low compared to historical trends (Figure 5-10a). In addition, a lower proportion of the induced seismicity has occurred close to the well in recent years than in earlier years (Figure 5-10b). Hence, there is no evidence in the seismicity recorded to date that the reservoir permeabilities near the injection well have decreased.

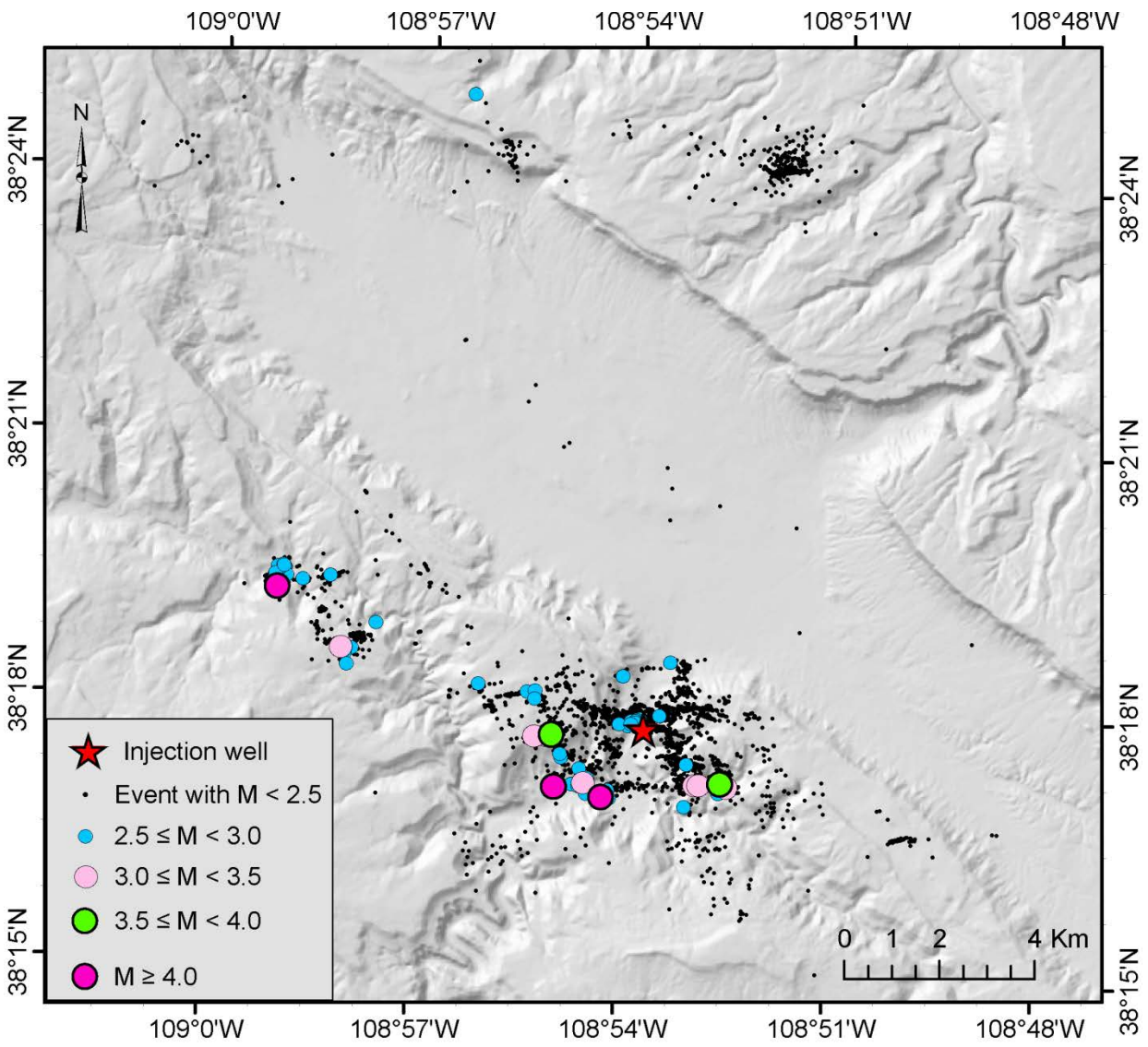

Figure 5-9. Epicenters of induced earthquakes, color-coded by magnitude.

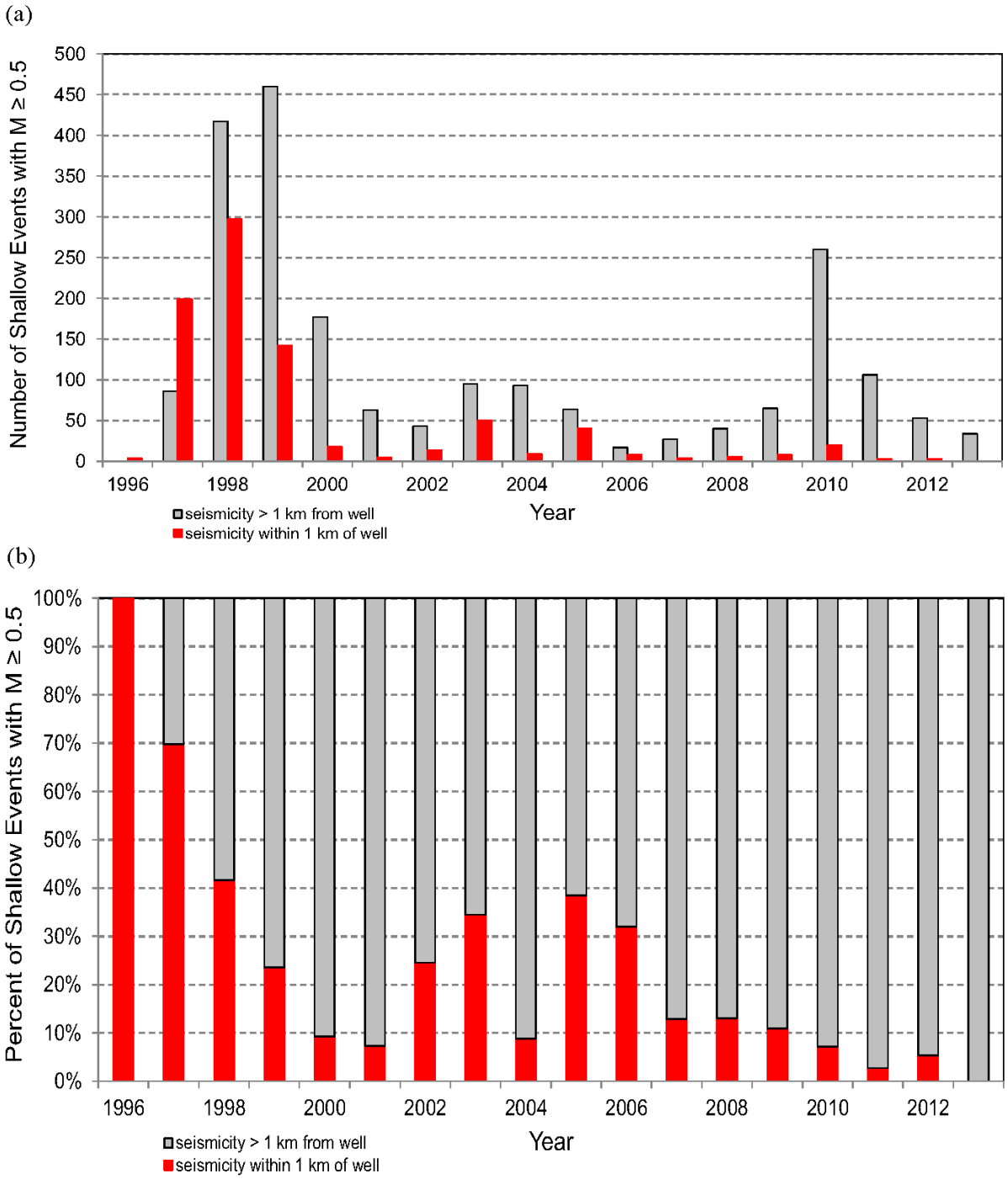

Figure 5-10. Annual rates of induced earthquakes within 1 km of PVU Injection Well #1 (red) and greater than 1 km from the well (gray): (a) number of events (b) percent of events. All shallow (depth < 8.5 km) seismic events with magnitude ≥ M_D 0.5 are included.

5.4 Geographical Expansion of Seismicity

The geographical expansion of seismicity has varied over time. The rate of expansion was highest during the later injection tests (1994-1995) and the early phase of long-term injection (1996-2000) (Figure 5-11). However, in mid-2000, when the PVU injection flow rate was decreased by about one-third in response to an M_L 4.3 induced earthquake, the geographical expansion of seismicity slowed greatly, and the spatial extent of the near-well and NW-cluster seismicity areas largely stabilized. While new clusters of seismicity appeared in the northern-valley area in the years following the reduction in flow rate, seismicity rates there were very low. There were only minor changes in the seismicity patterns between the time periods of 2000-2003 (Figure 5-12a) and 2004-2008 (Figure 5-12b). This relatively stable period lasted for about a decade.

Beginning in 2009, the spatial distribution and rates of seismicity began to change again (Figure 5-12c). A distinct group of earthquakes developed in 2010 about 6 km southeast of the injection well, the SE cluster. While the first detected SE cluster event occurred in 2004, with two additional events recorded in 2008 and 2009, beginning in 2010 the SE cluster experienced increasing rates of seismicity: 11 events in 2010, 17 events in 2011, and 25 events in 2012. Seismicity rates were also markedly elevated in some of the northern-valley clusters in 2010 and 2011: 557 northern-valley earthquakes were detected in 2010 and 113 were recorded in 2011,

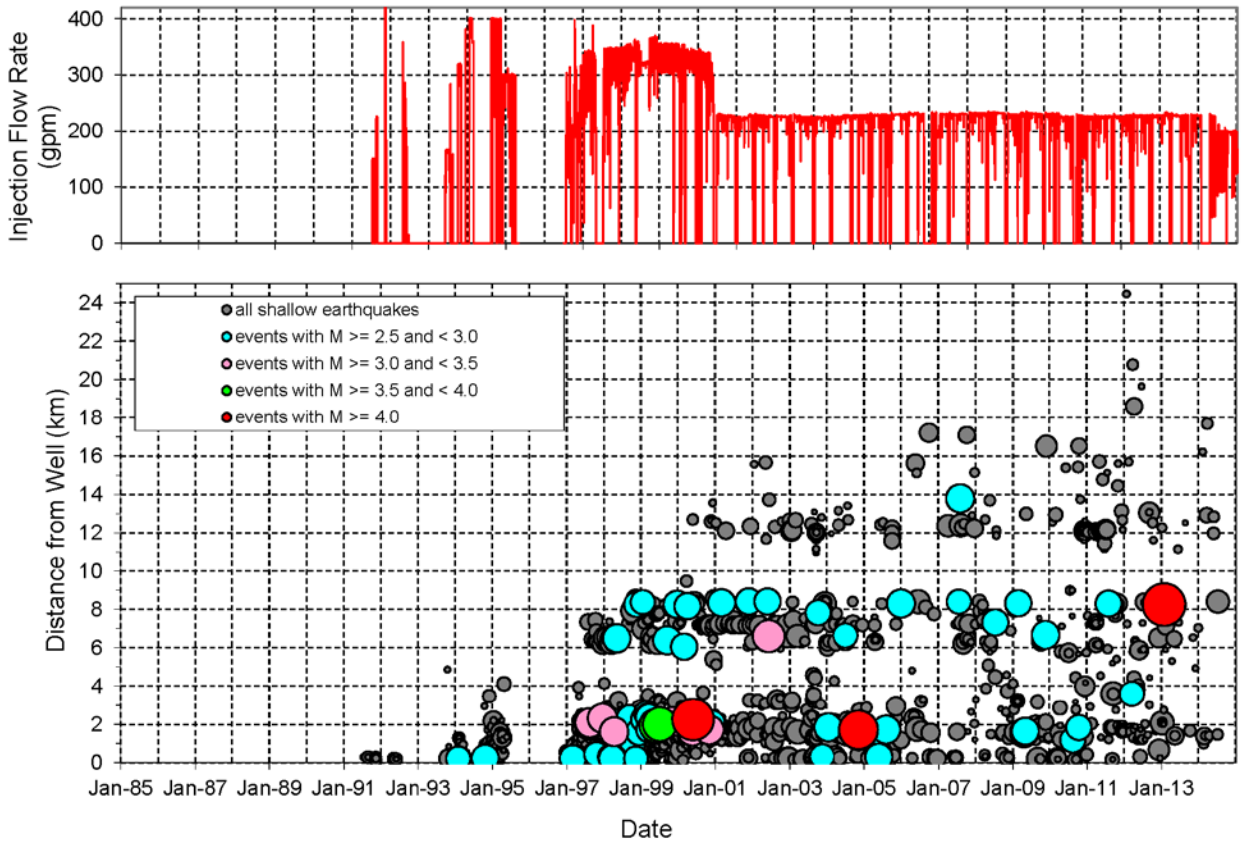

Figure 5-11. Correlation between injection flow rate (top) and shallow seismicity (< 8.5 km depth) recorded by PVSN (bottom).

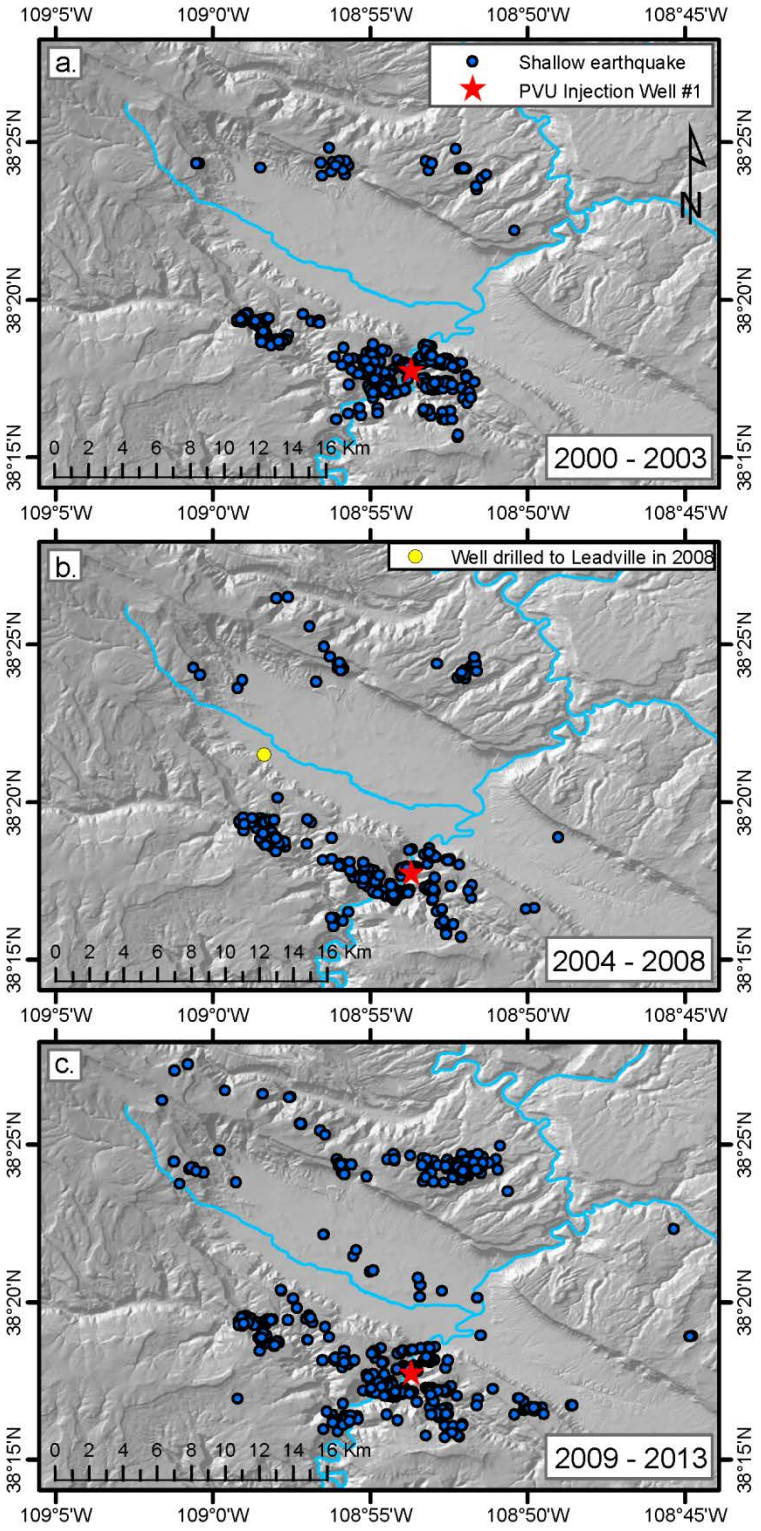

Figure 5-12. Maps showing the spatial distribution of shallow seismicity recorded in the Paradox Valley area over time: (a) 2000-2003; (b) 2004-2008; (c) 2009-2013. All detected earthquakes locating less than 8.5 km deep (relative to the ground surface elevation at the injection wellhead) are included.

greatly exceeding the previous annual rates of 2 to 33 events per year. Additionally, since 2009 seismicity has been recorded in new areas, including in the center of Paradox Valley and along the northwest edge of Paradox Valley. Furthermore, in January 2013, a local magnitude 4.4 earthquake occurred more than 8 km from the injection well, almost four times farther from the well than any previous M 3.5+ earthquake induced at PVU. The changing seismicity patterns observed in recent years suggest that pore-pressure perturbations may be reaching new areas and that pore pressures may be increasing in already stimulated regions. These observations are consistent with far-field reservoir pressurization inferred from modeling of the pressure-flow data.

Based on the spatial distribution of induced seismicity, the influence of PVU fluid injection on reservoir pore pressures does not appear to be radially symmetric. Earthquakes that we interpret as induced by PVU fluid injection occur at distances up to ~18 km north and northwest of the well (Figure 5-12c). To the southwest, south, and southeast of the well, however, induced seismicity is only observed to distances of 5-7 km. In addition, seismicity was first observed in the SE cluster, located 6 km southeast of the injection well, 7 years after seismicity had begun in the NW cluster, located 6-8 km northwest of the well. Differences in the geographical expansion of seismicity by azimuth strongly suggest that pore pressure perturbation is not radially symmetric about the well and that elevated pore pressures may extend to much greater distances in some azimuthal directions than others.

5.5 Spatial Extent of Injected Brine

Neither the pressure-flow modeling nor the induced seismicity analyses presented above yield estimates of the spatial extent of the injected brine. We have made some gross estimates of the spatial extent of the injected brine using simple volumetric analyses. Our method and results are included in Appendix A. Here we show some of the results to briefly examine the relationship between the spatial distribution of brine and the spatial distribution of seismicity and pore pressure diffusion.

The approximate relationship between the spatial extent of the injected brine, the spatial extent of the induced seismicity, and a 1-D pressure diffusion model is illustrated in Figure 5-13. This time-distance plot shows the radial distance of the observed seismicity and models of pore pressure diffusion and brine intrusion as a function time. Results from 4 simple volumetric models of brine intrusion are included. In two of these models, we assume that the injected brine is confined to the higher-porosity ($\geq$ 3%) zones in all of the sub-salt formations, as identified from well log data. The combined thickness of these zones is 90 m, and the weighted average porosity from the sonic porosity well log is 5.6% (Appendix A). In the other 2 brine intrusion models, we assume that the brine is confined to the higher-porosity zones in the Leadville formation only. The combined thickness of these zones is 50 m, and the weighted average porosity is 5.5%. We further sub-divide each of these two models into 2 scenarios. In one scenario, we assume that the injected brine displaces the in-situ fluid in only 5% of the pore space, in all time periods. The remaining 95% of porosity is assumed to be inaccessible to the injected brine, either because of restricted permeability or because the injected brine mixes with the in-situ fluid instead of displacing it. In the second scenario, we assume that the injected brine invades only 5% of the pore space during the injection tests, but that the percent of pore space

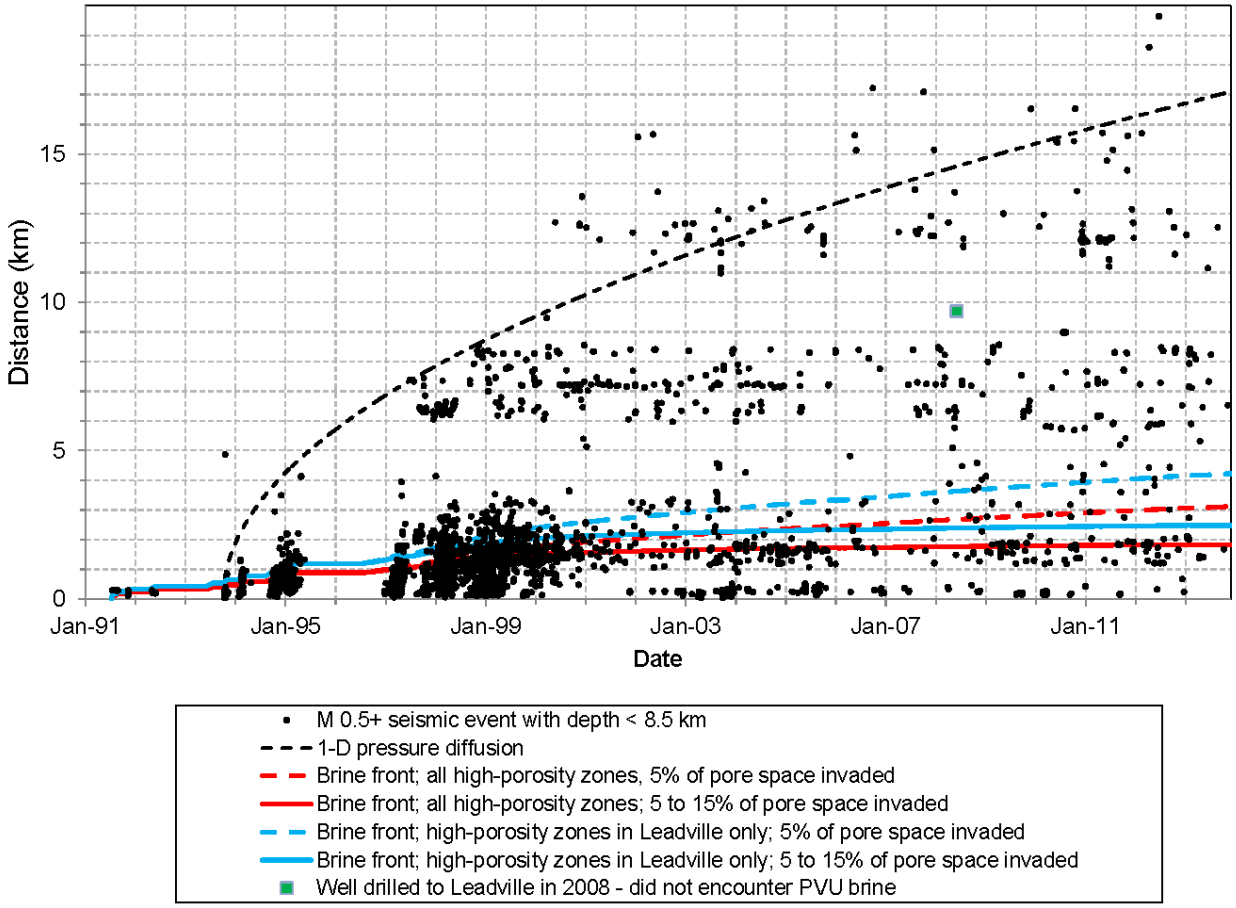

Figure 5-13. Estimated radial distance from the well of the injected brine over time, based on 4 different cylindrical models (red and blue curves). The shallow earthquakes with M ≥ 0.5 (black dots) and a 1-D pore pressure diffusion curve with diffusivity = 0.115 m^2/s (dashed black line) beginning at the time of the first significant injection test (after acid stimulation) are shown for comparison. The green square represents a well drilled into the Leadville formation in 2008, in which no PVU brine was encountered.

invaded by the brine linearly increases during long-term injection from 5% to 15%. Since PVU typically injects well above the fracture propagation pressure, fractures likely grow over time, increasing permeability and providing access to additional pore space. In addition, as the reservoir formations are intruded by the injected brine, the rock matrix will cool. This thermal effect should cause the rock matrix to shrink, further opening fractures and increasing porosity. We model potential increases in porosity and/or permeability over time by gradually increasing the percent of existing pore space that we assume the injected brine can occupy.

The brine intrusion models shown in Figure 5-13 illustrate that the spatial extents of the pore pressure front and induced seismicity grow at a substantially faster rate than the spatial extent of the injected brine. Hence, the induced seismicity occurs ahead of the brine front, with the distance gap between the two increasing over time. This is especially true for the brine intrusion models in which the fraction of porosity invaded by the injected brine increases over time. For these models, the radial expansion of the brine front greatly decreases as the brine instead diffuses into additional pore space near the well. The relationship between the spatial extent of the induced seismicity and injected brine shown in Figure 5-13 is consistent with a model of

seismicity being triggered by pore pressure perturbation, since pressure perturbation propagates through the in-situ fluids ahead of the injected brine.

The brine intrusion models presented above yield estimates for the current radial distance of brine intrusion of roughly 2 to 4 km. If some of the injected brine invades lower-porosity intervals, or the fraction of pore space occupied by the brine is greater than 0.05, then the estimated radial distance would be less. Conversely, if the fraction of pore space occupied by the brine is less than 0.05 or the porosity decreases away from the injection well, then the estimated distance would be greater. The sensitivity of the results to different assumptions is investigated further in Appendix A. The estimated distance of brine intrusion of 2-4 km shown here is consistent with observations made in an exploration well drilled in 2008 9.7 km northwest of PVU Injection Well #1, on the edge of Paradox Valley (Figure 5-12b; Figure 5-13, green square). That well penetrated the Leadville formation, and chemical analysis of the deep brine recovered from the well did not match the chemistry of the brine injected at PVU (personal communication, Cleary Petroleum Corp. to Reclamation, 2008). Hence, this single data point suggests an upper limit of ~10 km for the brine intrusion as of 2008.

5.6 Induced Seismicity Discussion

Induced seismicity patterns are consistent with the results from the pressure-flow modeling that indicate a lack of near-wellbore flow impairment. Near-well seismicity patterns indicate substantial vertical hydraulic connectivity within ~3 km of the injection well, and the hydraulic connectivity appears to have remained fairly constant since early in injection operations. The seismic data suggest that permeability may have increased in the reservoir formations to distances of ~1.5-2.0 km from the well during early injection operations (prior to mid-2000). Seismicity patterns within 2 km of the well have not changed significantly since ~2001-2002, suggesting that near-well permeabilities are stable. These observations are consistent with results of the pressure-flow modeling, which indicate fairly constant permeabilities since ~2002 within an estimated radius of investigation of 1 to 2 km.

The large-scale geographical expansion of induced seismicity is consistent with far-field reservoir pressurization. Since 2009, seismicity rates have increased in some regions, and induced seismicity has been detected in previously aseismic areas. These changes have been observed at distances up to ~18 km from the injection well. Hence, while the region immediately surrounding the injection well to a radial distance of about 2 km has been most strongly altered by injection operations, the seismicity patterns indicate that pore pressures have likely increased over much larger distances. Because of the low, fracture-dominated permeability of the Leadville formation, elevated pore pressures may be propagated over large distances through a limited network of fractures, potentially leading to a complex pore pressure field. Areas southwest, south, and southeast of the well have only experienced low rates and magnitudes of seismicity at radial distances > ~2.5 km and have not experienced any seismicity at distances > 7 km, suggesting that geologic factors may be limiting pore pressure increase in these areas.

6 Conclusions

No evidence of near-well flow impairment is observed over the last several years, either in the pressure-flow modeling or in the patterns of induced seismicity. Rather, both the pressure-flow modeling and the induced seismicity are consistent with far-field reservoir pressurization. There is some evidence for a decrease in the wellbore storage capacity of the near-well area in early years, most clearly shown by the decrease in the modeled wellbore storage constant between January 2002 and June 2002, but any degradation in the near-well reservoir properties does not appear to have progressed since that time.

These studies suggest that reservoir pressurization has occurred to at least a distance of ~2 km from the injection well, and that substantial elevations in pore pressure could be occurring at much greater distances (up to ~18 km from the well) in some azimuthal directions.
The radius of investigation of the pressure-flow modeling of individual injection cycles is estimated to be 1 to 2 km. Therefore, this modeling suggests substantial pore pressure increase in the target injection formations to a distance of at least 1-2 km from the well. Changes in the patterns of induced seismicity occurring ≥6 km from the well observed since 2009 suggest that reservoir pressures may be increasing at distances up to ~18 km from the injection well in some azimuthal directions. However, seismicity patterns are strongly asymmetric around the wellbore. Areas southwest, south and southeast of the well, at radial distances greater than about 2–2.5 km, have experienced relatively low levels of seismicity, suggesting that geologic factors may be limiting pore pressure increase in these areas.

7 References

Abramowitz, M, and I. A. Stegun, 1964, *Handbook of Mathematical Functions with Formulas, Graphs, and Mathematical Tables*, Dover Publications, New York, 1064 pp.

Agarwal, R. G., R. Al-Hussainy, and H. J. Ramey Jr., 1970, An investigation of wellbore storage constant and skin effect in unsteady liquid flow: I. Analytical treatment: Society of Petroleum Engineers Journal, v. 10, no. 3, p. 279-290.

Ake, J., K. Mahrer, D. O'Connell, and L. Block, 2005, Deep-Injection and Closely Monitored Induced Seismicity at Paradox Valley, Colorado: Bulletin of the Seismological Society of America, v. 95, no. 2, p. 664-683, doi: 10.1785/0120040072.

Assumpcão, M., Yamabe, T. H., Barbosa, J. R., Hamza, V., Lopes, A. E.V., Balancin, L., and M. B. Bianchi, 2010, Seismic activity triggered by water wells in the Paraná Basin, Brazil: Water Resources Research, v. 46, W07527, doi:10.1029/2009WR008048.

Baisch, S., M. Bohnhoff, L. Ceranna, Y. Tu, and H. Harjes, 2002, Probing the crust to 9-km depth: fluid-injection experiments and induced seismicity at the KTB superdeep drilling hole, Germany: Bulletin of the Seismological Society of America, v. 92, no. 6, p. 2369-2380.

Baisch, S., R. Vörös, R. Weidler, and D. Wyborn, 2009, Investigation of fault mechanisms during geothermal reservoir stimulation experiments in the Cooper Basin, Australia: Bulletin of the Seismological Society of America, v. 99, no. 1, p. 148-158, doi: 10.1785/0120080055.

Baisch, S., R. Vörös, E. Rothert, H. Stang, R. Jung, and R. Schellschmidt, 2010, A numerical model for fluid injection induced seismicity at Soultz-sous-Forêts: International Journal of Rock Mechanics and Mining Sciences, v. 47, no. 3, p. 405-413.

Bear, J., 1972, Dynamics of Fluids in Porous Media, Dover Publ.

Biot, M. A., 1941, General theory of three-dimensional consolidation, Journal of Applied Physics, v. 12., p. 155-164.

Biot, M. A., 1962, Mechanics of deformation and acoustic propagation in porous media, Journal of Applied Physics, v. 33, p. 1482-1498.

Block, L., 2014, Second Injection Well Site Selection CRB – Recommendations following December 2012 Meeting, Bureau of Reclamation, Denver, CO, 16 pp.

Block. L., V. King, W. Yeck, and M. Meremonte, 2014a, 2013 Annual Report, Paradox Valley Seismic Network, Paradox Valley Unit, Colorado, Technical Memorandum No. 85-833000-2014-32, Bureau of Reclamation, Denver, CO, 60 pp.

Block, L., and C. Wood, 2009, Overview of PVU-Induced Seismicity from 1996 to 2009 and Implications for Future Injection Operations, Technical Memorandum No. 86-88330-2009-22, Bureau of Reclamation, Denver, CO, 16 pp.

Block, L. V., C. K. Wood, W. L. Yeck, and V. M. King, 2014b, The 24 January 2013 M_L 4.4 Earthquake near Paradox, Colorado, and its Relation to Deep Well Injection: Seismological Research Letters, v. 85, no. 3, doi:10.1785/0220130188, 16 pp.

Block, L., W. Yeck, V. King, S. Derouin, and C. Wood, 2012, Review of Geologic

Investigations and Injection Well Site Selection, Paradox Valley Unit, Colorado, Technical Memorandum No. 86-68330-2012-27, Bureau of Reclamation, Denver, CO, 71 pp.

Bremkamp, W., and C. L. Harr, 1988, Area of Least Resistance to Fluid Movement and Pressure Rise, Paradox Valley Unit, Salt Brine Injection Project, Bedrock, Colorado, Bureau of Reclamation, Grand Junction, CO, 39 pp.

Bruel, D., 2007, Using the migration of the induced seismicity as a constraint for fractured Hot Dry Rock reservoir modelling: International Journal of Rock Mechanics and Mining Sciences, v. 44, p. 1106-1117.

Campbell, J. A., 1981, Summary of Paleozoic stratigraphy and history of western Colorado and eastern Utah, in *Western Slope Colorado*, 32nd Field Conference Guidebook, New Mexico Geological Society, Socorro, N. M., p. 81-87.

Detournay, E., and A.H.-D. Cheng, 1993, Fundamentals of poroelasticity, Chapter 5 in *Comprehensive Rock Engineering: Principles, Practice, and Projects, Vol. II, Analysis and Design Method*, ed. C. Fairhurst, Pergamon Press, p. 113-171.

Dinske, C., 2010, Interpretation of Fluid-Induced Seismicity at Geothermal and Hydrocarbon Reservoirs of Basel and Cotton Valley: Ph. D. dissertation, Freien Universität Berlin, Berlin, Germany, 151 pp.

Doelling, H. H., 1988, Geology of Salt Valley anticline and Arches National Park, Grand County, Utah, in *Salt Deformation in the Paradox Region*, Bulletin 122, Utah Geological and Mineral Survey, Salt Lake City, Utah, p. 1-58.

Durá-Gómez, I., and P. Talwani, 2010, Reservoir-induced seismicity associated with the Itoiz Reservoir, Spain: a case study: Geophysical Journal International, v. 181, p.343-356.

Dusseault, M. B., T. Davis, A. W. Eustes III, and J. Nunn, 2013, Assessment of a potential second injection well site in the Paradox Valley Unit saline water disposal project.

Envirocorp Services and Technology Inc., 1995, Report of evaluation of injection testing for Paradox Valley Injection Test No. 1, Bureau of Reclamation, Durango, CO, 68 pp.

Fekete, 2012, WellTest user manual (7.6.0 ed.): Calgary, Fekete Associates Inc.

Freeze, R. A., and J. A. Cherry, 1979, *Groundwater*, Prentice-Hall, Inc., Englewood Cliffs, New Jersey, 604 pp.

Harr, C. L., 1988, Final geological well report, Bureau of Reclamation Injection test Well No. 1, Paradox Valley, Montrose County, Colorado, U. S. Bureau of Reclamation, Grand Junction, CO.

Healy, J. H., W. W. Rubey, D. T. Griggs, and C. B. Raleigh, 1968, The Denver Earthquakes: Science, v. 161, no. 3848, p. 1301-1310.

Horner, D. R., 1951, Pressure build-up in wells: Leiden, Netherlands, E. J. Brill.

Hsieh, P. A., 1979, A Reservoir Analysis of the Denver Earthquakes: A Case of Induced Seismicity, Master's thesis, Department of Hydrology and Water Resources, University of Arizona, Tuscon, AZ.

Hummel, N., and T. M. Muller, 2009, Microseismic signatures of non-linear pore-fluid pressure diffusion, Geophysical Journal International, v. 179, p. 1558-1565.

King, V. M., L. V. Block, W. L. Yeck, C. K. Wood, and S. A. Derouin, 2014, Geologic structure of the Paradox Valley Region, Colorado, and relationship to seismicity induced by deep well injection: Journal of Geophysical Research, doi:10.1002/2013JB010651.

Kharaka, Y. K., G. Ambats, J. J. Thordsen, and R. A. Davis, 1997, Deep well injection of brine from Paradox Valley, Colorado; potential major precipitation problems remediated by nanofiltration: Water Resources Research, v. 33, no. 5, p. 1013-1020.

Lee, W. J., 1982, *Well Testing*, Society of Petroleum Engineers Textbook Series, Dallas, TX, 159 pp.

Mahrer, K., J. Ake, and L. Block, 2002, 2001 Status Report—Paradox Valley Seismic Network, Paradox Valley Project, Southwestern Colorado, Technical Memorandum No. D8330-2001-007, Bureau of Reclamation, Denver, CO, 37 pp.

Mahrer, K., J. Ake, D. O'Connell, and L. Block, 2003, 2002 Status Report—Paradox Valley Seismic Network, Paradox Valley Project, Southwestern Colorado, Technical Memorandum No. D8330-2003-009, Bureau of Reclamation, Denver, CO, 75 pp.

Mahrer, K., J. Ake, D. O'Connell, and L. Block, 2004, 2003 Status Report—Paradox Valley Seismic Network, Paradox Valley Unit, Southwestern Colorado, Technical Memorandum No. D8330-2004-04, Bureau of Reclamation, Denver, CO, 126 pp.

Mahrer, K., L. Block, and J. Ake, 2001, 2000 Status Report—Paradox Valley Seismic Network, Paradox Valley Project, Southwestern Colorado, Technical Memorandum No. D8330-2001-007, Bureau of Reclamation, Denver, CO, 34 pp.

Nuccio, V. F., and S. M. Condon, 1996, Burial and thermal history of the Paradox Basin, Utah and Colorado, and petroleum potential of the middle Pennsylvanian Paradox formation, in Geology and Resources of the Paradox Basin, UGA 25, edited by A. C. Huffman et al., Utah Geological Association, Salt Lake City, Utah, p. 57-76.

Raleigh, C. B., J. H. Healy, and J. D. Bredehoeft, 1972, Faulting and crustal stress at Rangely, Colorado, in *Flow and Fracture of Rocks*, American Geophysical Union Geophysical Monograph 16, Washington D. C., p. 275-284.

Roeloffs, E., and R. Denlinger, 2009, An Axisymmetric Coupled Flow and Deformation Model for Pore Pressure Caused by Brine Injection in Paradox Valley, Colorado: Implications for the Mechanisms of Induced Seismicity: Preliminary Report to the Bureau of Reclamation, U. S. Geological Survey, 31 pp.

Rothert, E., 2004, Fluid Induced Microseismicity: Data Modeling and Inversion for Hydraulic Properties of Rocks: Ph. D. dissertation, Freien Universität Berlin,Berlin, Germany, 127 pp.

Russell, B. H., and T. Smith, 2007, The relationship between dry rock bulk modulus and porosity – an empirical study, University of Calgary Consortium for Research in Elastic Wave Exploration Seismology Research Report, v. 19, 14 pp.

Shapiro, S. A., E. Huenges, and G. Borm, 1997, Estimating the crust permeability from fluid-injection-induced seismic emission at the KTB site: Geophysical Journal International, v. 131, p. F15-F18.

Shapiro, S. A., Audigane, P., and J. Royer, 1999, Large-scale *in situ* permeability tensor of rocks from induced microseismicity, Geophysical Journal International, v. 137, p. 207-213.

Shapiro, S. A., Rothert, E., Rath, V., and J. Rindschwentner, 2002, Characterization of fluid transport properties of reservoirs using induced microseismicity: Geophysics, v. 67, no. 1, p. 212-220.

Shapiro, S. A., and C. Dinske, 2009, Fluid-induced seismicity: Pressure diffusion and hydraulic fracturing: Geophysical Prospecting, v. 57, p. 301-310.

Suburface Technology, 2001, Report of operations: Houston, no. 60D5207, 24 p.

Talwani, P., and S. Acree, 1984, Pore Pressure Diffusion and the Mechanism of Reservoir-Induced Seismicity: Pure and Applied Geophysics, v. 122, no. 6, p. 947-965.

Talwani, P., Chen, L., and K. Gahalaut, 2007, Seismogenic permeability, K_s: Journal of Geophysical Research, v. 112, B07309, doi:10.1029/2006JB004665.

Walker, J. D., and J. G. Geissman, (Compilers), 2009, Geologic Time Scale, Geological Society of America, Boulder, CO, doi:10.1130/2009.CTS004R2C.

Wang, H. F., 2000, *Theory of Linear Poroelasticity with Applications to Geomechanics and Hydrogeology*, Princeton University Press, Princeton, New Jersey, 287 pp.

1) Wang, H., E. Detournay, M. Dusseault, M. Fehler, and C. Frohlich, 2015, Report from the Consultant Review Board on Paradox Valley Unit – MASIP/Induced Seismicity Meeting No. 1., Grand Junction, CO.

Williams, P. L., 1964, Geology, structure, and uranium deposits of the Moab Quadrangle, Colorado and Utah, Miscellaneous Investigations Series Map I 360, U. S. Geological Survey, Denver, CO.

Wood, C., V. King, L. Block, and W. Yeck, 2016, The M_L 4.4 Earthquake of January 24, 2013, Near Paradox, Colorado, and Implications for Near-term Injection Operations, Draft Technical Memorandum No. 86-68330-2013-12, Bureau of Reclamation, Denver, Colorado, 166 p.

Appendix A Models for the Spatial Extent of Injected Brine

We use simple volumetric analyses to estimate the spatial extent of the brine injected at the PVU Injection well #1. For these simple calculations, we assume that the volume of rock containing the injected brine can be represented by one or more cylinders centered at the injection well and that the brine is uniformly distributed within each cylinder. The relation between injected volume V, cylinder height h, cylinder radius r, and effective porosity ϕ is then:

$$\frac{V}{\phi} = \pi r^2 h$$

Estimates of the porosity of target injection formations are provided in Bremkamp and Harr (1988). From the sonic porosity well log, 164 ft (50 m) of the Leadville formation were determined to have 3% or greater porosity (Table A-1). Using the reported porosities and thicknesses, we calculate a weighted average porosity of 5.5% for this 164-ft (50-m) interval. These higher-porosity zones are reported by Bremkamp and Harr to be scattered through 18 different depth intervals within the 416 feet of Leadville formation encountered in the well. Bremkamp and Harr (1988) do not report porosity values for the remaining 252 ft (77 m) of the Leadville, but the sonic-porosity log indicates much lower porosities for the remaining intervals. Assuming a porosity of 0.5% for the remaining intervals yields a weighted average porosity of 2.5% for the entire 416-ft (127-m) Leadville formation. Assuming a porosity of 1% yields a weighted average (2.8%) that differs only slightly, and hence the average porosity of the entire Leadville formation is not very sensitive to the value assumed for the low-porosity zones.

Table A-1. Higher-porosity zones within the Leadville formation reported in Bremkamp and Harr (1988). Values were derived from the sonic-porosity well log for PVU Injection Well #1.

Thickness (ft)	Thickness (m)	Porosity Range (%)	Median Porosity (%)
48	14.6	3 – 4	3.5
30	9.1	4 – 5	4.5
74	22.6	5 – 8	6.5
10	3.0	8 – 10	9
2	0.6	>10	14*

*An upper porosity limit of 18% was used for this interval, based on core-derived porosities reported in Bremkamp and Harr (1988).

Table A-2. Higher-porosity zones within non-Leadville sub-salt formations reported in Bremkamp and Harr (1988). Values were derived from the sonic-porosity well log for PVU Injection Well #1.

Lithology	Thickness (ft)	Thickness (m)	Weighted Average Porosity (%)
dolomites & limestones	28	8.5	4
sandstones	48	14.6	5.5
Precambrian schist	54	16.5	7
Total	130	39.6	5.8

Bremkamp and Harr (1988) report an additional 130 ft (39.6 m) of higher-porosity zones in the Devonian to Precambrian units. They report weighted average sonic-derived porosities for the total dolomite/limestone, sandstone, and Precambrian schist lithologies, as listed in Table A-2. The weighted average porosity for all these zones is 5.8%.

Considering the range of possible zones that could accommodate the injected brine, we construct simple cylindrical models for five scenarios: (1) injected brine is confined to the higher-porosity zones within the Leadville formation; (2) brine is confined to the high-porosity zones within all formations; (3) brine is confined to the entire Leadville formation; (4) brine is confined to the entire Leadville formation plus the higher-porosity zones in the other formations; and (5) brine is accommodated by all sub-salt Paleozoic formations and into the upper 160 ft of the Precambrian basement. Possible brine intrusion to a depth of 160 ft into the Precambrian basement is used because Bremkamp and Harr (1988) report that the Precambrian has adequate reservoir characteristics to that depth. Weighted average porosities for these scenarios were computed using the porosity values listed in Tables A-1 and A-2 and assuming a porosity of 0.5% for the remaining intervals. Because of the uncertainties in the porosity measurements and because porosity may vary with distance from the well, we consider a range of possible porosity values for each scenario. The range extends from one-half to twice the computed weighted averaged porosity. The interval thickness (corresponding to the cylinder height used in the calculations), weighted average porosity, and porosity range for each scenario are listed in Table A-3.

Table A-3. Scenarios used for cylindrical brine intrusion models.

Scenario	Thickness (ft)	Thickness (m)	Weighted Average Porosity (%)	Porosity Range (%)
Higher-porosity zones in Leadville only	164	50	5.5	2.8 – 11.0
Entire Leadville	416	127	2.5	1.2 – 4.9
Higher-porosity zones in all formations only	294	90	5.6	2.8 – 11.3
Entire Leadville plus higher-porosity zones in other formations	546	167	3.3	1.6 – 6.5
All sub-salt formations	1913	583	1.3	0.6 – 2.6

Using the thicknesses (cylinder heights) and porosity ranges listed in Table A-3, we compute corresponding radii of cylinders containing the cumulative volume of brine injected through October, 2014 (2.12×10^9 gal, or 8.02×10^6 m^3). The results for the 5 scenarios are shown in Figure A-1. The estimated extent of brine intrusion ranges from about 0.4 to 1.3 km from the injection well.

1) The results shown in Figure A-1 were computed using several simple assumptions, including the assumptions that all the formation porosity is accessible to the injected brine (effective porosity = total porosity) and that the injected brine completely displaces the in-situ fluid. If some of the pore space is inaccessible due to limited permeability or the injected brine mixes with the in-situ fluid, then the porosity available to the injected brine could be considerably lower than the formation porosities used in the above calculations. To evaluate how this could affect the results, we re-compute radii assuming that 50% of the formation pore space is available to the injected brine (Figure A-2). In this case, radii range from 0.6 to 1.9 km. If only 10% of the pore space is accessible, then the radii range from ~1.3 to 4.3 km (Figure A-3).

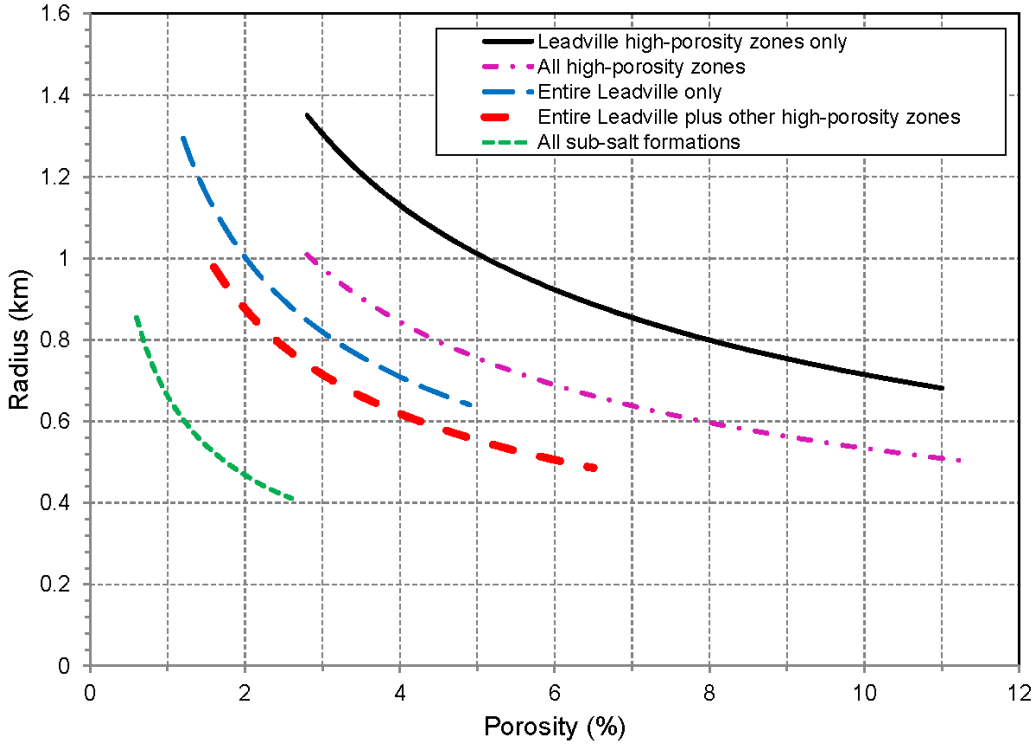

Figure A-1. Computed radii for five cylindrical models of the injected brine, assuming 100% of the formation pore space is accessible.

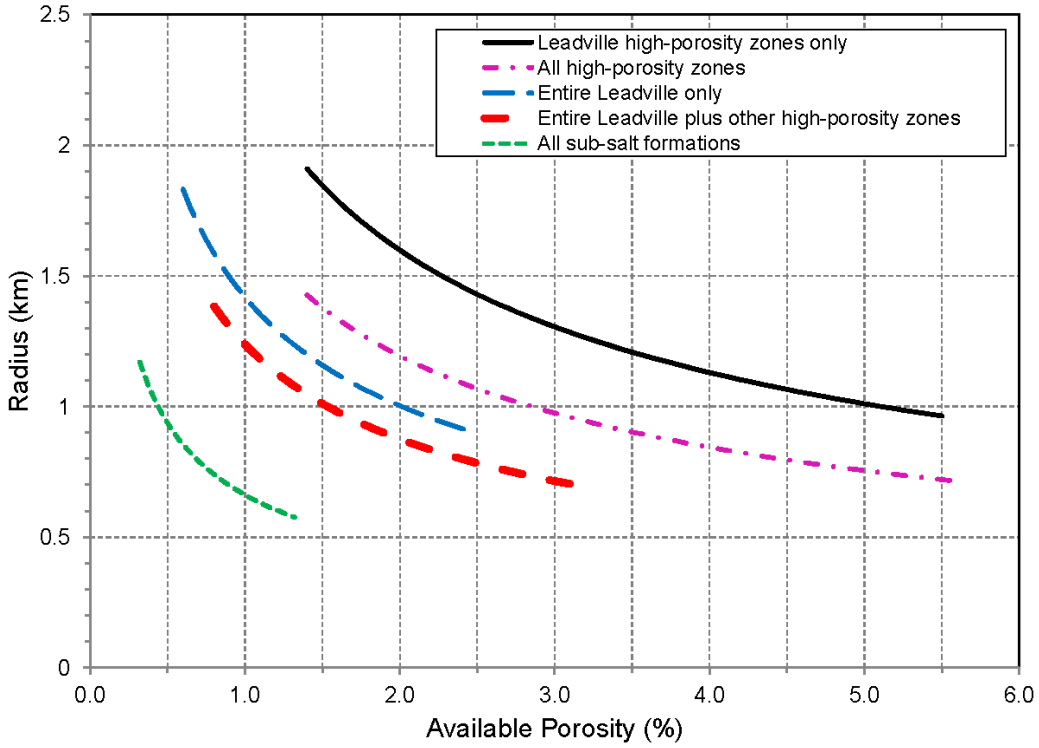

Figure A-2. Computed radii for five cylindrical models of the injected brine, assuming 50% of the formation pore space is accessible.

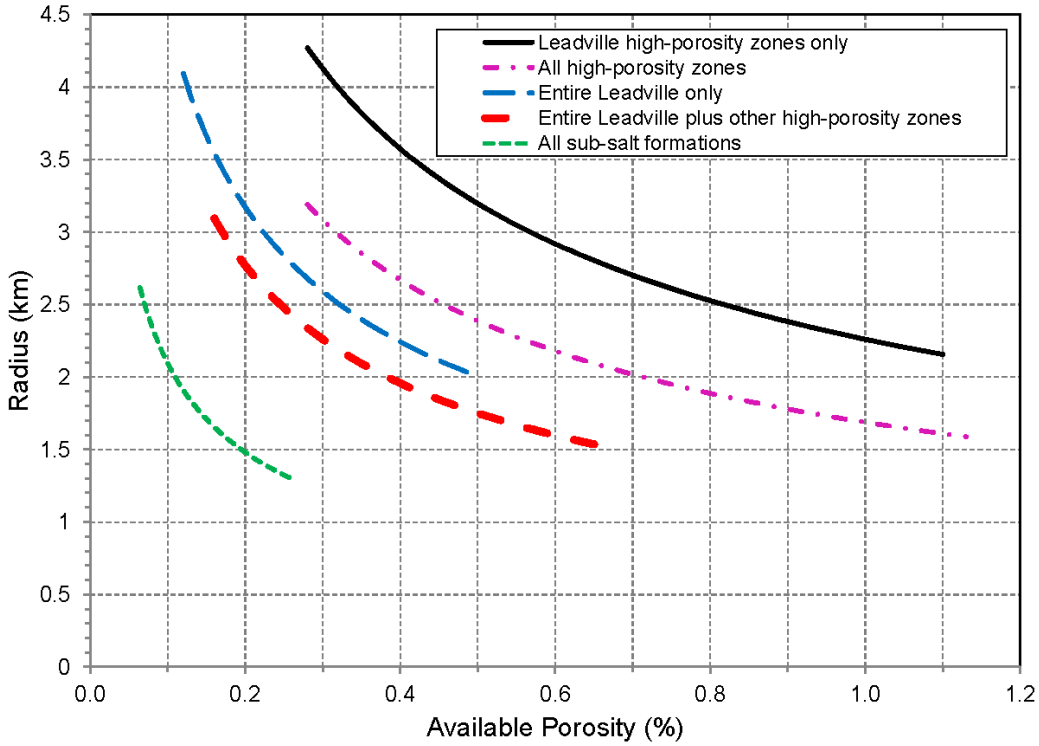

Figure A-3. Computed radii for five cylindrical models of the injected brine, assuming 10% of the formation pore space is accessible.

We further evaluate the dependence of the computed radii on the fraction of pore space accessible to the injected brine in Figure A-4. In this plot, we show computed radii as a function of the fraction of pore space occupied by the brine. For these calculations, the weighted average porosities of the corresponding lithologies are used for each scenario (from Table A-3). The results indicate that, if at least 25% of the formation pore space is accessible to the injected brine, then the computed extent of brine intrusion is ≤ 2 km. If 10% of the pore space is accessible, then the computed radii range from roughly 2 to 3 km. If only 5% of the pore space is accessible, then the radii range from approximately 2.5 to 4.5 km. As the fraction of available pore space decreases below 0.05, the computed radii greatly increase as the curves become asymptotic.

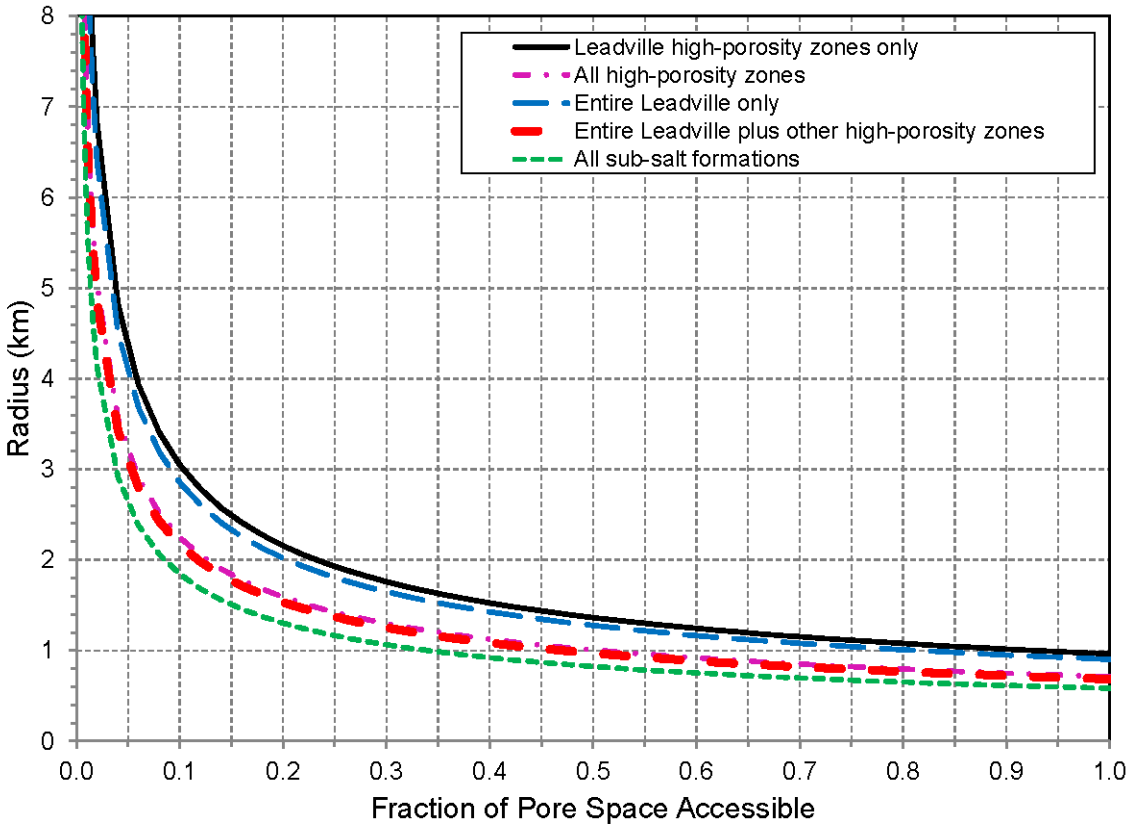

Figure A-4. Computed radii for five cylindrical models of the injected brine as a function of the fraction of pore space that is occupied by the brine. The weighted average formation porosities shown in Table A-3 are used for these calculations.

The rate at which the radius of injected brine grows over time is investigated in the plot presented in Figure A-5. This example shows the scenario in which the injected brine is confined to the higher-porosity zones in all formations. This corresponds to a cylinder with a height of 90 m and porosity of 5.6%. In Figure A-5, the radius of the cylinder containing the brine is shown as a function of time, assuming four values for the percent of the porosity that is occupied by the injected brine: 100%, 30%, 10%, and 5%. As can be seen, the rate of brine intrusion predicted by these simple models is inversely proportional to the percent of pore space occupied by the brine. For the lowest assumed pore space fraction occupied by the brine (5%), the highest rate of growth occurs. In addition, all models show that the rate of brine intrusion has been lower since 2000 than before; this is due to the lower flow rates that have been used since 2000.

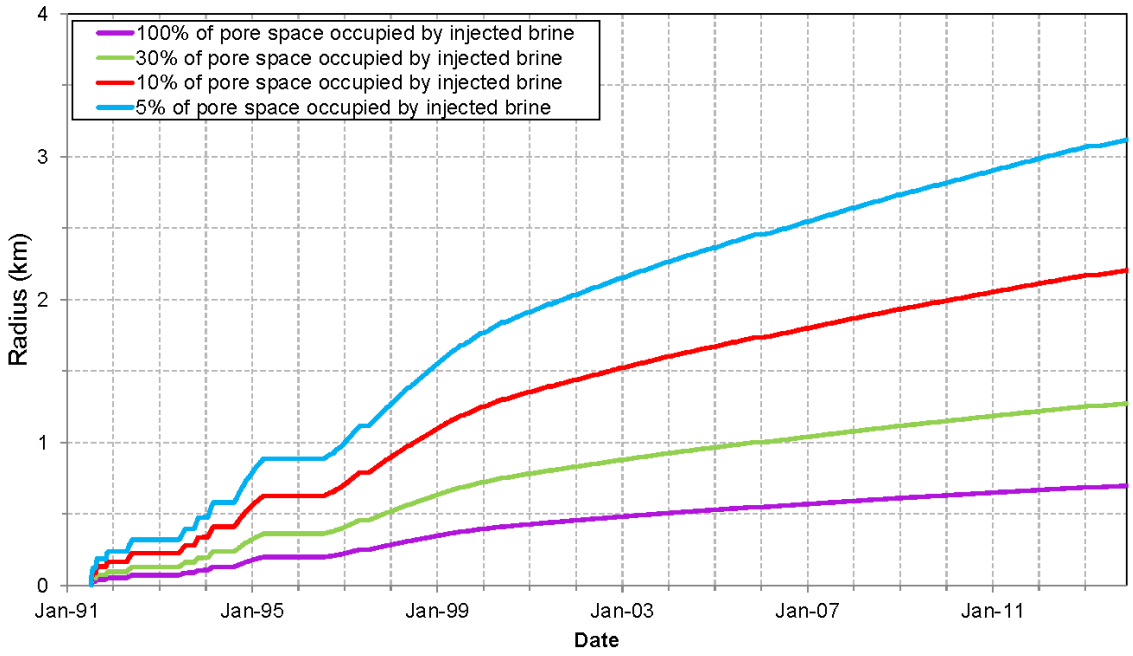

Figure A-5. Computed radii over time for the scenario in which the injected brine is confined to the higher-porosity zones in all formations (cylinder height = 90 m; formation porosity = 5.6%). Curves are shown for four assumed values of the percent of pore space occupied by the injected brine.

The assumption used in the above analysis that the fraction of pore space occupied by the injected brine is constant over time is likely not correct. Since PVU typically injects well above the fracture propagation pressure, fractures likely grow over time, increasing permeability and providing access to additional pore space. In addition, as the reservoir formations are intruded by the injected brine, the rock matrix will cool. This thermal effect should cause the rock matrix to shrink, further opening fractures and increasing porosity. We can model potential effects of increasing porosity and/or permeability over time by increasing the fraction of pore space occupied by the injected brine over time. For example, in Figure A-6 we show the computed radius as a function of time for the same model as in Figure A-5, except that the percent of pore space occupied by the injected brine is 5% during the injection tests and then linearly increases

during long-term injection from 5% (in July,1996) to 15% (in October, 2014). As can be seen, increasing the amount of pore space occupied by the injected brine over time by a modest amount can greatly slow the geographical expansion of the brine.

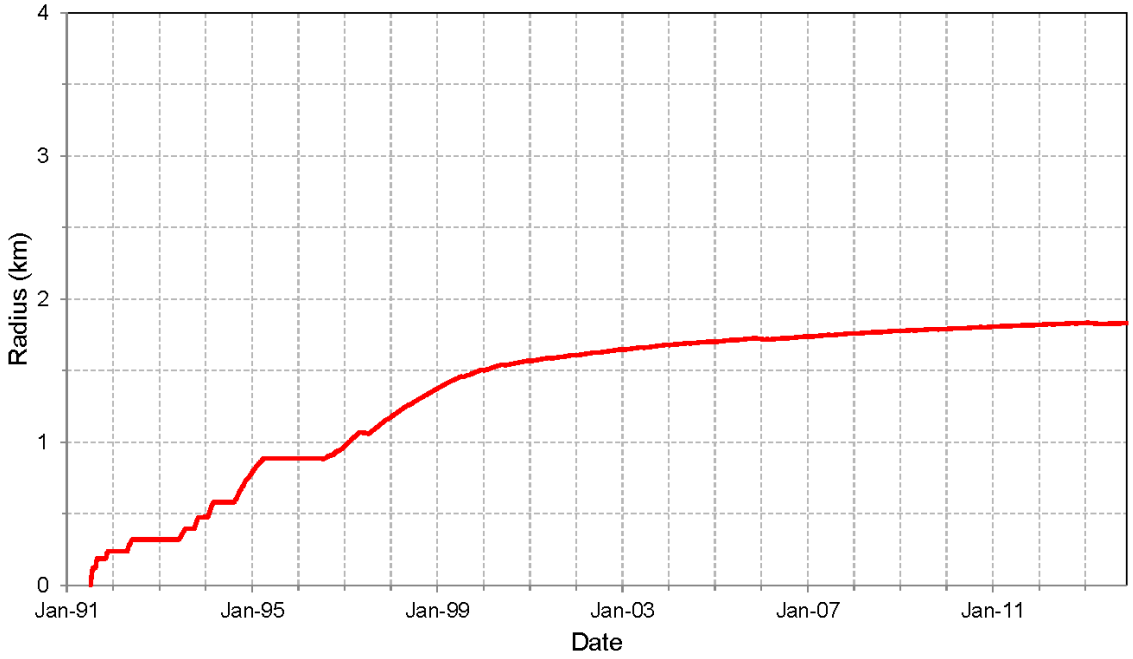

Figure A-6. Computed radius over time for the scenario in which the injected brine is confined to the higher-porosity zones in all formations (cylinder height = 90 m; formation porosity = 5.6%). The percent of pore space occupied by the injected brine is 5% during the injection tests and then linearly increases during long-term injection from 5% (in July, 1996) to 15% (in October, 2014).

Appendix B Electronic Supplement of Pressure and Flow Rate Data

Daily average pressure and flow rate data are included in an electronic attachment to this Technical Memorandum. The data encompass the injection test period and continuous injection Phases I-IV, from July 10, 1991, to April 16, 2013. While the injection test data are not analyzed, their inclusion is necessary to replicate the results of the analyses, as the pressure response of the reservoir is dependent on the complete flow rate history.

The injection test data have several gaps, extending up to several months. There are periods where the injection rates and pressures appear to be inconsistent with one another, for example increasing pressures during periods of 0 flow rate. These discrepancies appear to indicate poor data quality. We have not attempted to correct these errors; they are presented "as-is."

The data completeness is significantly better during the period of continuous injection, which began in 1996. However, there was a gap in the pressure data from June 6, 2001 to June 18, 2001, which was filled in using interpolation. Additionally, the pressures on the following four days, from June 19 to June 22, 2001, were inconsistent with the shape of the fall-off curves from other cycles. Thus, it seems likely that these values are in error, and they were filled in using interpolation as well.

The pressures in the attachment are surface pressures. Downhole pressures can be calculated using the fluid density, which varies over time, as shown in Table B-1.

Table B-1. Fluid density.

Start Date	End Date	Density (g/cm^3)
07/11/1991	8/14/1991	1.000
08/15/1991	11/04/1991	1.058
11/05/1991	06/05/1993	1.115
06/06/1993	10/2/1993	1.000
10/3/1993	1/7/2002	1.122
1/8/2002	4/16/13	1.173

The earthquake catalog data used in this analysis have not been attached to this Technical Memorandum but are available as an electronic attachment to Wood et al. (2016).